Università degli Studi di Napoli Federico II

Scuola Politecnica e delle Scienze di Base

Dipartimento di Ingegneria Industriale

TESI DI LAUREA IN INGEGNERIA AEROSPAZIALE
CLASSE DELLE LAUREE MAGISTRALI IN INGEGNERIA
AEROSPAZIALE E ASTRONAUTICA
(LM-20)

Analysis of In-Orbit Break-Up Models, Debris Cloud Evolution, and Short-term Collision Risk Assessment

Relatore
Prof. Ing. Giancarmine Fasano

Correlatori
Prof. Ing. Roberto Opromolla
Ing. Giorgio Isoletta

Tutor aziendale
Ing. Andrea Zollo

Candidata
Annarita Trombetta
M53/1621

Anno Accademico 2023–2024

Università degli Studi di Napoli Federico II

Scuola Politecnica e delle Scienze di Base

Dipartimento di Ingegneria Industriale

TESI DI LAUREA IN INGEGNERIA AEROSPAZIALE
CLASSE DELLE LAUREE MAGISTRALI IN INGEGNERIA
AEROSPAZIALE E ASTRONAUTICA
(LM-20)

Analysis of In-Orbit Break-Up Models, Debris Cloud Evolution, and Short-term Collision Risk Assessment

Relatore
Prof. Ing. Giancarmine Fasano

Correlatori
Prof. Ing. Roberto Opromolla
Ing. Giorgio Isoletta

Tutor aziendale
Ing. Andrea Zollo

Candidata
Annarita Trombetta
M53/1621

Anno Accademico 2023–2024

Abstract

The primary objective of this thesis is to assess the short-term collision risk between a debris cloud and operational spacecraft, with the aim of developing a prototype tool to enhance the operational safety of resident space objects. As space technology has advanced, the rate of spacecraft launches has steadily increased, leading to congestion in Earth's orbital environment. This overpopulation increases the likelihood of in-orbit break-ups, which generate significant amounts of space debris and pose substantial risks to operational spacecraft. While active debris-removal techniques continue to evolve, studying debris dynamics is essential for evaluating collision risks. The increasing accumulation of space debris presents a particularly acute hazard in the immediate aftermath of a break-up event, where traditional risk assessment methods are inadequate due to the lack of comprehensive tracking data. Key break-up models, such as NASA's Standard Break-up Model (SBM), are analysed in terms of their ability to describe fragments distributions by size, velocity, and area-to-mass ratio. The research also investigates debris cloud evolution, particularly in the initial phase post-break-up, where the dynamics of fragments is significantly affected by ejection velocities. Understanding the short-term dynamics of debris clouds is crucial for establishing the assumptions on which the collision risk assessment tool is based. The study confirms that Keplerian motion assumptions hold in the short-term phase. The tool, developed in Python, calculates collision probability using the multi-revolution Lambert's problem and a mapping technique from position space at a given time into spread velocity space at the time of break-up, as each debris acquires an additional velocity from the break-up. A novel approach to handling uncertainty in the break-up epoch is also introduced. The findings demonstrate the effectiveness of this approach in providing timely assessments of collision risks, which is crucial for the safe operation of spacecraft. A novel approach to consider uncertainties on the break-up epoch is also presented. The results underscore the need for improved risk models to ensure space safety in the increasingly congested low-Earth orbit environment.

Contents

Acknowledgements

I would first like to express my heartfelt gratitude to my academic tutor for the unwavering support provided not only during these six months, but throughout my entire university journey. Your guidance has been instrumental in my development. I would also like to sincerely thank my co-tutors for their valuable support and insights during this project.

I would like to extend my gratitude to all the members of the Flight Dynamics group, with whom I had the privilege of embarking on this extraordinary journey. Working alongside your expertise has been incredibly valuable for my technical and professional growth, but what I appreciated most was the friendly and welcoming atmosphere that made every day enjoyable.

Last but by no means least, I would like to express my deepest thanks to my technical supervisor, Andrea. This thesis would not have been possible without you, your profound expertise, and, above all, your patience (and the countless coding days). In you, I found not only unwavering technical support, but a true friend I can always count on.

At this point, I would like to switch to Italian to thank the people who are dearest to me.

Il ringraziamento più grande lo voglio dedicare alla persona che è sempre in prima fila per me. Mamma, grazie per essere sempre stata al mio fianco. La tua determinazione e la tua bontà d'animo, qualità che in te raggiungono un livello raro e straordinario, sono state una fonte di ispirazione per il mio impegno e lo saranno per ogni nuova avventura che affronterò nella mia vita.

Un ringraziamento altrettanto grande va al mio papà, il mio compagno di risate. Il mio cuore si scioglie ogni volta che mi chiami "Ingegnere", perché con la tua voce lasci trapelare quanto tu sia fiero di me. Grazie per essere sempre al mio fianco, per non aver mai avuto un dubbio nelle mie capacità. Sei l'esempio costante da cui ho imparato tanto e la spalla silenziosa su cui sempre mi poggerò.

Grazie Mamma e Papà per aver reso possibile e sostenuto, attraverso i vostri sacrifici, questo mio traguardo. Ricordate che, ovunque io sia, ci sarò sempre per voi.

Adesso tocca alla persona che in cinque anni è stata la mia constante, Nonna Luisa. La tua forza d'animo è ciò che ha guidato il mio percorso, e ha lasciato un segno indelebile nella persona che sono. Grazie per essere la mia seconda mamma . Sappi che tu, in me, sei eterna.

Un ringraziamento speciale va anche al mio secondo papà, zio Giggi. Ti ringrazio per essere stato sempre dalla mia parte e per essere parte di ogni mia avventura.

Non posso non dedicare un grazie speciale alla persona che ha reso questo percorso ancora più straodinario, Luca. Grazie per sostenermi in ogni mio obiettivo come se fosse il tuo. Sono grata a questo percorso per averci fatto incontrare, per aver permesso di crescere insieme e di diventare la squadra fortissima che siamo.

Voglio ringraziare tutti i miei amici, che mi hanno accompagnato lungo questo percorso con il loro affetto e supporto costante. Anche quando sono lontana, so che ci sono delle persone su cui posso sempre contare, pronte a farmi ridere e consolarmi, con cui sentirmi di nuovo una ragazzina. La vostra amicizia è stata fondamentale per arrivare fino a qui, e sono immensamente grata di avervi nella mia vita.

Infine, ma non per importanza, un immenso grazie va anche a tutte le persone che, con la loro vicinanza e affetto, mi hanno sostenuto in questi anni. La vostra presenza, anche nei piccoli gesti, è stata preziosa per ciò che ho realizzato.

Dedico questo traguardo ai miei nonni, che oggi non sono qui, ma che sarebbero stati fieri di me. Grazie, nonna Candida e nonno Vincenzo, per tutto ciò che mi avete donato e che custodisco con amore dentro di me. Ma il mio grazie più immenso va alla persona che più di tutti avrebbe desiderato di essere qui con me oggi. Grazie nonno Michele per aver sempre fatto il tifo per me. Vorrei tanto averti qui oggi, per vedere ancora una volta la gioia e l'orgoglio nei tuoi occhi luccicanti. Oggi, come due anni fa, questo traguardo non è mio, ma è nostro, per continuare a costruire insieme sulla Luna.

Abbreviations

AEDC Arnold Engineering Development Complex

ASAT Anti-Satellite

BVP Boundary Value Problem

CAM Collision Avoidance Maneuver

CAS Collision Avoidance System

CDM Conjunction Data Message

CM Center of Mass

CSpOC Combined Space Operations Center

DCS DebriSat Categorization System

DEM Digital Elevation Model

DLR Deutsches Zentrum für Luft- und Raumfahrt (German Aerospace Center)

DOD Department of Defense

ECI Earth-Centered Inertial

ESA European Space Agency

FD Flight Dynamics

FEM Finite Element Method

GEO Geostationary Earth Orbit

GNSS Global Navigation Satellite System

GSOC German Space Operations Center

HAX Haystack Auxiliary Radar

HBR Hard Body Radius

HVI Hyper-Velocity Impact

IMPACT Integrated Multiple Platform Analysis and Collision Tool

ISS International Space Station

LEO Low Earth Orbit

LEOP Launch and Early Orbit Phase

LP Long-Period

LRIR Long-Range Imaging Radar

MASTER Meteoroid and Space Debris Terrestrial Environment Reference

NASA National Aeronautics and Space Administration

NORAD North American Aerospace Defense Command

ODPO Orbital Debris Program Office

ORDEM Orbital Debris Engineering Model

PDF Probability Density Function

PoC Probability of Collision

R/B Rocket Body

RSO Resident Space Object

RTN Radial Tangential Normal

S/C Spacecraft

SBM Standard Break-up Model

SDPA-E Space Debris Prediction and Analysis Environment

SMC Space and Missile Systems Center

SOCIT Satellite Orbital Debris Characterization Impact Test

SP Short-Period

SPH Smoothed Particle Hydrodynamics

SSN Space Surveillance Network

TCA	Time of Closest Approach
TIRA	Tracking and Imaging Radar
TLE	Two Line Elements
TOD	True of Date
TOF	Time Of Flight
UF	University of Florida

List of Symbols

Symbol	**Definition**
A	Cross-section
A/m	Area-to-mass ratio
A_x	Fragment cross-section
$\mathbf{\Phi}$	State transition matrix
HBR	Primary sphere radius
d	Particle's diameter
Δt	Time of flight
ΔV	Additional/Ejection velocity
E	Orbit energy
e	Eccentricity
f	PDF function
g	Propagator function
h	Mapping function
i	Inclination
$J2$	Second zonal harmonic coefficient
L_c	Characteristic length
M	Mean anomaly
m	Mass
μ	Mean value
μ_E	Earth's gravitational constant
n	Mean motion
N	Number of fragments
ν	True anomaly
Ω	Right ascension of the ascending node
P_C	Probability of collision
P_i	Probability of collision of a single fragment
p	Semi-latus rectum
R	Number of revolution
R_E	Earth's radius
r	Position
r_1	Parent Position
r_2	Primary Position

ρ	Density
S	Scaling factor
SV	State vector
σ	Standard deviation
T	Simulation time
T_t	Transfer orbit period
T_T	Time to torus
t	Time
t_0	Time at break-up
V	Velocity
V_1	Parent Velocity
V_2	Primary Velocity
$\mathcal{V}$	Volume

List of Figures

List of Tables

List of Algorithms

General context

German Space Operation Center (GSOC)

This Master's thesis has been developed in collaboration with the German Space Operations Center (GSOC) at Oberpfaffenhofen near Munich. The center employs over 300 people, whose tasks involve preparing and implementing both crewed and uncrewed international space missions. The institute is primarily responsible for operating and controlling spacecraft, their subsystems and payloads. The main task is to plan and execute all essential sequences of activities to operate spacecraft, such as corrections to flight and orbital paths. GSOC has played a pivotal role in space operations since 1969 and continues to be a key player, offering expertise in various fields. To mention only a few, the institute is currently monitoring and operating a series of Earth Observation satellites, such as BIROS, Eu:CROPIS, EnMAP, GRACE-1 and GRACE-2 as part of an efficient multi-mission operation. Furthermore, it has been controlling the TerraSAR-X mission since 2007, when the German high-resolution radar satellite TerraSAR-X was launched. In 2010, the TanDEM-X radar satellite was added, which is operated in formation flight with its twin satellite. Additionally, GSOC is responsible for conducting the flight dynamics operations for the entire Galileo constellation, the Global Navigation Satellite System (GNSS) developed by the European Union through the European Space Agency (ESA). In the field of GEO missions it is responsible for the operations of EDRS-A and EDRS-C of the European Data Relay System (EDRS) constellation, and it operates the two satellites of SatcomBW, which is the German Armed Forces' (Bundeswehr) satellite communication system. Lastly, GSOC is in charge of the operations of two payloads: ColKa on the International Space Station (ISS) and the Technical Demonstrator Payload TDP-1 on AlphaSat. Regarding interplanetary flight, it supported the HELIOS A and B missions to the Sun, ESA's GIOTTO mission and NASA's Jupiter mission GALILEO, having the task of monitoring the Retro Propulsion Module (RPM). GSOC already has 31 years of expertise in manned spaceflight. In 1985, with control of the mission Spacelab D1, it became the first European Control center to be directly involved in manned missions. Then, the center followed the operations for Spacelab D2, EUROMIR and the Space Shuttle mission SRTM. Because of its unique track record in crewed spaceflight, ESA selected GSOC to operate the Columbus research module, Europe's most important contribution to the ISS.

Flight Dynamics group

This work has been supported by the Flight Dynamics group of GSOC. Its role is to assist the satellites operated by the facility. It provides the necessary flight dynamics services and researches and develops pioneering technologies for the operations of space missions. FD group handles a diverse range of tasks, including feasibility studies for orbit or formation control concepts, flight dynamics requirements assessment. It also has a role within mission analysis, including addressing first contact influences, optimizing launch windows and reference orbits, and acquiring and positioning target orbits. They also focus on orbit maneuver planning and optimisation, evaluating attitude, life expectancy, re-entry, and orbital events. Furthermore, it executes attitude operations. In the realm of software and systems engineering, they apply flight-proven tools and enhance or develop new systems and interfaces to meet specific requirements. They also offer training and simulation services, providing lectures and training on FDS software, and supporting offline and real-time simulations. Additionally, the group supports pre-launch activities, including training and simulation campaigns, interface tests, and launch and LEOP planning activities. They handle orbit determination using tracking data or GNSS navigation data, achieving cm-precise orbit determination and mm-precise relative navigation based on GNSS raw observations. The FD Group provides products for science and customers, such as precise orbit and attitude ephemeris data. Moreover, they perform collision avoidance analysis and plan and assess Collision Avoidance Maneuvers (CAM). Last but not least, research and development are fundamental for the FD group, which carries out an extensive research endeavor program. Within this framework, thesis and PhD projects are conducted, including this Master's thesis.

Framework

As previously mentioned, the FD group is responsible for carrying out special operations related to conjunction risk assessment and collision avoidance maneuvers (CAMs) execution. The Collision Avoidance System (CAS) relies on Conjunction Data Messages (CDMs) provided by the Combined Space Operations Center (CSpOC) in the United States. The CDM contains information about a single conjunction between two objects, such as the Time of Closest Approach (TCA), position, velocity, and covariance of both objects at TCA. Once received, the CAS develops products such as the probability of collision and the miss distance at TCA, which are then analyzed by FD engineers to achieve a GO/NO GO decision. In scenarios where the colliding objects are already present in the Space Track Catalog, CDMs are sent to the operations center well in advance, providing sufficient time for operators to assess the situation. However, just after the occurrence of an in-orbit breakup event, no CDM is immediately available. Debris detection and tracking is a long and complex operation with many intrinsic challenges, as will be explored later in this thesis. Hence, there is a blackout period from the time the fragmentation event happens until the moment all possible debris are tracked and catalogued. Nevertheless, these blackout windows may still represent a significant threat to operational spacecraft. Currently, the FD group does not have any tools to address the collision risk assessment in the early time just after a break-up. This gap in the current capabilities of the FD group is the primary motivation for this thesis. The goal is to explore and develop methodologies and tools that can enhance the early assessment of collision risks immediately following a fragmentation event. By addressing this critical need, the aim is to improve the overall safety and reliability of space operations, ensuring that spacecraft can effectively avoid potential collisions with newly generated debris.

Goal of the Thesis

Given the general context illustrated above, this thesis work aims at analysing the problem of short-term collision risk assessment of a debris-cloud and gaining strong knowledge in astrodynamics and experience on the topic. The purpose is to provide a prototype tool to contribute to the research advancement and to future and more complex usage within the FD group. To achieve this goal, it was essential to build a solid background on the problem. This is why the thesis is structured with two preceding sections, one focused on conducting an analysis of break-up models and the other on investigating the debris cloud evolution. Finally, the work is structured as follows:

- Chapter 1 provides a detailed analysis of the space debris environment, highlighting its criticality. Then, the definition of a break-up event follows, focusing on its characteristics and potential causes. Finally, an investigation on debris cloud collision probability challenges is provided;

- Chapter 2 provides an overview of existing break-up models, detailing their classification and derivation. It explains the inputs and outputs of each model, while highlighting their advantages and disadvantages;

- Chapter 3 supplies a theoretical description of phases of debris cloud evolution, focusing on the relative importance of different orbital perturbations and providing an overview of possible ejection velocity models. A clear distinction between short, medium and long-term evolution is delivered, which is of fundamental importance for the collision risk assessment. Then, the propagation of a test case in short and medium-terms is presented with the purpose of demonstrating the cloud's dynamics, in terms of its shape and Keplerian elements statistical distributions. Finally, a procedure to compute the duration of the short-term is outlined;

- Chapter 4 is the core element of the thesis, since it delivers challenges and a theoretical analysis of methodologies used for the collision probability computation in a debris cloud scenario, deeply exploring the physics of the problem and the assumptions. A detailed analysis of the implemented methodology is provided, which is based on multi-revolution Lambert's problem and mapping technique from position space at a given time into spread velocity space at time of break-up;

- Chapter 5 aims at testing and validating the tool. A test case is presented and used to demonstrate the applicability of the developed tool, whose results are compared to the reference. Then, a procedure to account for break-up epoch uncertainty is provided. The chapter is concluded presenting possible future advancements, that may be able to manage more complex and realistic scenarios and remove some limiting assumptions;
- Chapter 6 concludes this work, wrapping up all obtained results.

–1–
Introduction

1.1 Space environment around the Earth

The launch of Sputnik I in 1957 marked the start of the space access era. Since then, the rate of spacecraft launches has been steadily increasing. Future projections indicate an even greater surge, driven by humanity's insatiable quest for knowledge, the desire to surpass its limitations, and the influx of new private companies entering the space industry. Unfortunately, early space missions did not consider the potential risks posed by inactive satellites and space platforms. Hence, the space surrounding the Earth is congested, and this overpopulation can potentially lead to several in orbit break-up events, generating a conspicuous amount of space debris. Figure 1.1, provided by the Space Environment Statistics of ESA's Space Debris User Portal, shows the object count per year since 1960 up to 2024 divided by object category.

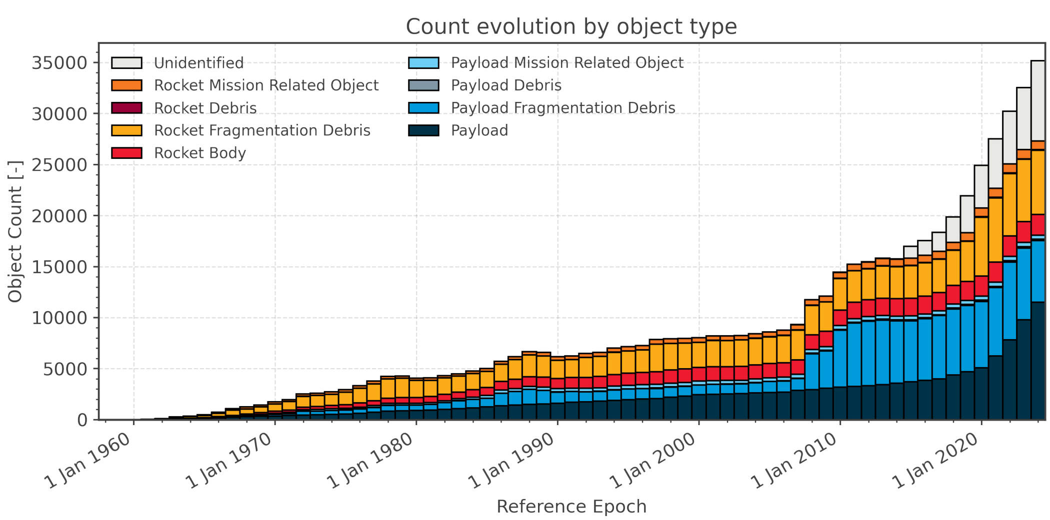

Figure 1.1: Number of space objects in orbit over time [1]

As it can be seen from the last figure, the majority of in orbit objects are space debris. The US Space Surveillance Network (SSN) reported 25,857 artificial objects in orbit above the Earth in 2021, of which only 5,465 are operational satellites [2]. While collision avoidance procedures can be performed if at least one of the colliding objects is cooperative, the concern lies in collisions between non-cooperative objects, such as space debris. Uncontrolled events of this kind have the potential to cause a cascade of collisions, exacerbating the overpopulated situation and increasing the risk for manned and unmanned spacecraft. This phenomenon is known as the Kessler's Syndrome [3]. The new space strategy is aware of this critical situation and is acting to control it. Meanwhile progress in active debris-removal techniques advances, studying their dynamics is absolutely necessary to evaluate the collision risk for operational spacecraft.

Today the analysis of the debris environment has become of fundamental importance even in the early phases of a space mission design. The analysis of the debris environment encountered by the spacecraft is performed as a mission analysis task, in order to estimate the expected number of CAMs to be executed during its lifetime. According to this study, the satellite's life-expectancy may change. Several space debris environment models do exist and can be used when a new platform is planned to be launched: the ORDEM 3.2 model of NASA, the MASTER-2001 model of ESA and the Russian SDPA-E model [4]. This series of models computes debris flux on an operational spacecraft given the known environment population at a certain epoch. The ORDEM software currently serves as the primary tool to provide a timely, validated model of orbital debris environment [5]. Being more specific, it computes the debris flux as the annual rate at which debris from a specified population, of a given size (or larger) and from a given direction would impact an equivalent spherical spacecraft with a unit cross-sectional area [6]. Orbit elements of the primary object, epoch of observation and minimum particle size are required as input.

To have a tangible proof of the situation criticality, a simulation with the ORDEM 3.2 software for a DLR mission controlled by GSOC has been performed. The mission is TerraSAR-X, a close formation mission of two twin imaging radar Earth observation satellites, TerraSAR-X and TanDEM-X. It provides a detailed and consistent Digital Elevation Model (DEM) of the Earth's entire land surface. Since their orbit parameters are very similar, only the TerraSAR-X satellite, whose orbit elements are shown in Table 1.1, has been considered for the simulation. Given its almost circular and sun-synchronous LEO orbit, this analysis is highly effective to acquire an idea of what a typical DLR's LEO mission might encounter.

a [km]	e	i [°]	Ω [°]	ω [°]
6880	0.0011	97.44	275.38	143.36

Table 1.1: TerraSAR-X orbit parameters

The simulation ends in the year 2030, and among the various products generated by the software, the most relevant one has been selected for demonstration. Figure 1.2 displays the debris particle flux at specific sizes and larger (i.e., cumulative flux) on the satellite over an orbit. The minimum and maximum margin of error (i.e., lower and upper one sigma uncertainties) are also represented. As it can be seen, the flux corresponding to the minimum and maximum particle size exhibits almost 11 order of magnitude of difference. The maximum flux reaches the order of 10^4 debris per square meters and year, which is a quite large value.

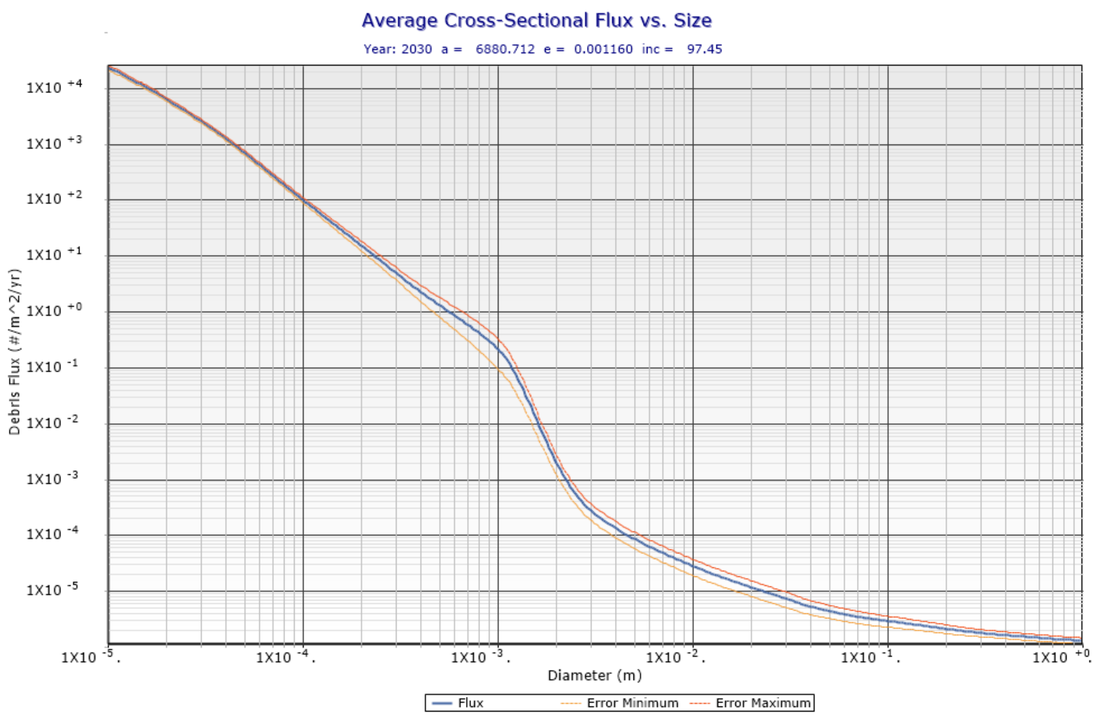

Figure 1.2: Average Flux vs size

A densely populated environment, such as that of LEO, increases the likelihood of collisions occurring. Indeed, there have been numerous recorded collision events in orbit in recent years. Among them, the collision of the Iridium 33 and Cosmos 2251 satellites is likely the most well-known. It was the first in-orbit accidental collision between satellites and produced the second largest debris cloud in the history of break-ups [7]. Cosmos-2251 was an inactive Russian platform for military communications of 900 kg, while Iridium-33 was a U.S. operational communications satellite of 560 kg and their orbits were almost circular. The collision occurred in February 2009 over northern Siberia, at an altitude of 789 km with an estimated impact velocity of 11.57 km/s. The first indication of the impact was the sudden loss of signals from the active satellite [8]. As of 1 December 2009, the U.S. space tracking system catalogued 1,632 fragments from the collision, many of which will remain in orbit for decades [7].

1.2 Break-up event definition

In the previous section, it has been clarified the overcrowded nature of the LEO debris environment and what the potential consequences are, such as collisions. Now, a more general definition and analysis of a break-up is delivered. An in-orbit break-up event is a fragmentation involving one or more space objects, called *Parents*. Such events can occur due to catastrophic or non-catastrophic collisions, but also to explosions. An explosion results in the full fragmentation of one space object. In a catastrophic collisions two objects (or more) are involved and they are both completely fragmented. Instead, in a non-catastrophic collision, the fragmentation is not entire. In a collision scenario, the larger object is referred to as the *Primary* or *Target*, while the smaller one as the *Secondary* or *Projectile* [9]. A concrete idea of each type of break-up is provided by computer illustrations shown in Figure 1.3.

(a) Explosion (b) Catastrophic Collision (c) Non-Cat. Collision

Figure 1.3: Break-up events categories: a) Columbia Space Shuttle explosion in 2003, b) Iridium33-Cosmos 2251 collision in 2009, c) Cerise collision in 1996

As stated in [9], reasons of these incidents might be various :

- Propulsion malfunctions;
- Residual propellants (typical for upper-stage);
- Electrical overcharging (explosion of batteries);
- Over-pressure due to the aerodynamic drag;
- Accidental collisions;
- Deliberate collisions (intentional break-up events for experimental or military purposes) and Anti-satellite tests (ASAT);
- Anomalous (unplanned separation of one ore more detectable objects from a platform).

Although determining the cause is difficult and sometimes impossible, the result is always the generation of a debris cloud, i.e., an ensemble of many fragments, whose dynamics evolves in time. The number of produced pieces depends on the initial conditions, such as the explosion energy or the collision impact velocity, but, in some cases, it can reach up to millions. Dealing with this huge number of fragments makes the collision risk assessment a complex and demanding operation, as will be discussed in the following sections.

To deeply delve into the physics behind a break-up, it can be assumed that each fragment receives an impulsive burn when fragmentation occurs, leading to a change in their orbital velocity by a quantity $\Delta\vec{V}_i$. This situation is intuitively visualised in Figure 1.4.

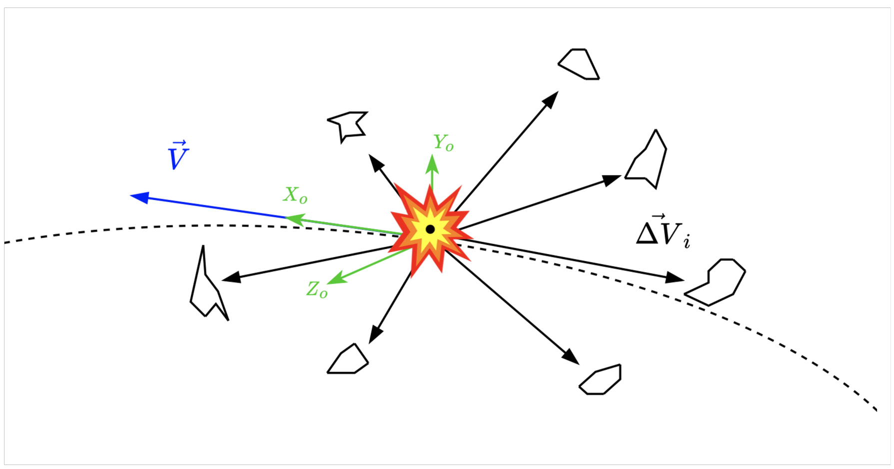

Figure 1.4: Break-up visualisation in terms of impulsive burns

Consequently, fragments will have slightly different orbits. Within this optic, the effect on the nominal orbit of a given $\Delta\vec{V}_i$ can be addressed following simple orbital mechanics equations. Each ejection velocity vector has an along-track, a radial and an out-of-plane components in the orbiting reference frame, determining the change of one or more orbital parameters.

When an along-track impulse is given at any point on a circular orbit or at the perigee (apogee) on an elliptic orbit, only a change in the orbital velocity magnitude is performed. This leads to a mechanical energy variation, hence of semi-major axis, as indicated by the following equation.

$$E = -\frac{\mu_E}{a} \tag{1.1}$$

In the latter, the Earth's gravitational constant is $398600.4418\,\mathrm{km^3/s^2}$. Depending if the $\vec{\Delta V}$ is aligned or not with the direction of motion, an increase or a decrease of the semi-major axis can be registered, respectively. This means that fragment orbits may differ from the parent orbit in terms of orbit period.

Instead, if a tangential impulse is given at a different point than the perigee (apogee) of an elliptic orbit, a semi-major axis variation is combined with a rotation of the line of periapsis and a change of eccentricity. A radial impulse shows the same effect.
When the imparted velocity has a non-zero out-of-planes component, a change of inclination and/or right ascension of the ascending node is applied. However, the $\vec{\Delta V}$ norm required for a given Δi variation is directly proportional to the orbital velocity, according to the equation 1.2.

$$\Delta V = 2V \sin\left(\frac{\Delta i}{2}\right) \tag{1.2}$$

For the same Δi, a change of inclination of a LEO orbit will take a larger value of imparted velocity than on a higher orbit, since the orbital velocity decreases with the altitude. Changing the orbit inclination is an extremely expensive action in terms of required imparted velocity, which becomes greater as the Δi increases. For these reasons, it is unlikely that a fragment may receive a consistent inclination variation. Nevertheless, it may be still possible, since ejection velocity magnitudes due to fragmentation event might reach very large values, but this is denied by historical break-up events, registering a maximum plane variation of 3° with respect to the parent orbit [10]. In any case, fragments of a given break-up still pose a significant threat to satellites with different inclination, because a collision may occur at the orbits intersections.

This discussion has been effective to address the characterisation of the initial orbits of fragments resulting from imparted velocities of the break-up. Actually, fragment orbits are also affected by perturbation, but their magnitude depends on the characteristics of each individual fragment. In a LEO scenario, an estimation of each ballistic coefficient is required for evaluating the effect of the atmospheric drag.

Additionally, effects of the Earth non-sphericity, such the J2 term due to its oblateness, should be taken in account. As results, the orbits of fragments will differ from the parent one because of the initial ejection velocities, but they will evolve and keep changing in time because of orbit perturbation. The debris cloud evolution is deeply explored in Chapter 3. This discussion has effectively demonstrated that the $\vec{\Delta V}$ is crucial to determine initial conditions of fragments just after the break-up and their dynamical evolution of these fragments over time. But how is it possible to determine these initial conditions? The answer lies in the break-up model, which provides the necessary parameters for initial conditions determination. Therefore, an overview of break-up models is thoroughly examined in Chapter 2.

1.3 Challenges of debris cloud collision probability

The immediate concern after a break-up is that one or more fragments of the cloud might collide with an operational space platform. The main parameter used to evaluate the criticality of a possible collision between two space objects is the Probability of Collision (PoC). The derivation of this metrics is well consolidated in the literature for a classical scenario where only two objects are colliding and a priori knowledge of their state and covariance at a given time before TCA is available. For such a scenario, there are different methodologies that are categorised according to the relative velocity of the encounter.

When computing the probability of collision between an object and a cloud of fragments, the classical approach does not hold for the following reasons:

- The encounter between the debris cloud and the target object cannot be treated as a series of individual encounters with each fragment because debris cloud characterisation may take a lot of time. Consequently, the state and positional uncertainties of each fragment may not be accurately known at the time of computation;

- Very small fragments are not routinely tracked and not considering them would lead to a risky under-estimation of the PoC;

The consequences of the first two points are the lack of information in the catalog about the state and covariance of fragments, which are the input for the classical collision risk assessment, and that the debris cloud characterization cannot be deterministic, meaning that it is not possible to rely solely on catalog inputs, as this would result in missing the smaller fragments.

1.3.1 Role of the Space Surveillance Network in debris cataloguing

After a break-up event, the cataloguing process of all fragments begins as soon as an evidence of the occurrence is retrieved. For example, for an in-orbit collision, where at least one of the two spacecraft is operational, the proof of the fragmentation might be the lack of signals from the active objects. The process is carried out through observations from the sensor network on ground, and it might take up to several months. Waiting until this procedure is concluded pones a threat to active satellite. Existing tools and ground procedures cannot be used before all possible fragments have been catalogued. The global Space Surveillance Network (SSN), operated by the U.S.-Canadian North American Aerospace Defense Command (NORAD), is the main source of data on the quantity, sizes, and orbits of space debris. Actually, this network was not designed for debris tracking, but for early-warning defence purposes. Accurately tracking all debris would not only be unfeasible due to sensor limitations, but it might compromise the actual network's aim [11]. The SSN consists of optical and radar sensors, mostly located on the north-western hemisphere [12]. The contributing sensors in Lexington (Massachusetts), which are controlled by MIT, are very important for debris surveillance. The Lexington site includes the Haystack Long-Range Imaging Radar (LRIR, or simply "Haystack"), the Haystack Auxiliary Radar (HAX), and the Millstone Hill radar. This site is able to detect LEO debris down to 2 cm in length. Instead, the Goldstone site (California) can detect LEO objects down to 2 mm [4].

From the Europe side, a high-performance radar facility is available. The FGAN Tracking and Imaging Radar (TIRA) system, located in Wachtberg near Bonn (Germany), is sensitive enough to detect 2 cm-sized objects at a distance of 1000 km. When combined with the Effelsberg radio telescope as a secondary receiver, the detection threshold reach the value of 0.9 cm at the same distance [13]. Depending on the energy release during the break-up, generated fragments are assumed to cover a size regime mainly within diameters of $0.1mm \leq d \leq 1m$ [4]. Because of coverage constraints and detection capability limitations, objects smaller than 10 cm in LEO and 1 m in GEO are not routinely tracked. The problem is that even fragments smaller than 1 mm can be lethal for an active satellite, and since they cannot be reliably tracked, they represent the most hazardous objects [4]. The key point of this discussion is that, due to the lack of early information about fragments and the complete absence of very small fragments in the Sat Catalog, the classical approach for collision risk assessment cannot be applied to debris cloud scenarios. This limitation is particularly critical in the immediate aftermath of a break-up (i.e the short-term), as the classical method relies on input states, position uncertainties, and physical characteristics of the objects, which are not available in this context. To solve this issue, break-up models are involved to radically remove the need of inputs from the catalog. They represent a statistical approach to immediately characterise a cloud in order to not neglect smaller particles, taking into account the uncertain and unpredictable nature of fragmentation phenomenon.

Due to these reasons, it is necessary to adopt an alternative methodology for the debris cloud short-term collision risk assessment that does not take inputs from the catalog, considers the lethality of untrackable fragments, and limits its computational expense. Consequently, this thesis aims at addressing these issues. Existing algorithms that tackle these issues are presented in Chapter 4.

–2–
Break-up models

In this chapter, existing categories of break-up models are presented and discussed, highlighting their advantages and disadvantages. An overview of the most commonly used models in debris environment tools is also provided. It is worth mentioning that existing models are numerous, and those referenced herein constitute only a small fraction, representing the most employed by space agencies and interested parties.

2.1 Break-up models categories

After an in-orbit break-up, the first step is to characterise every generated fragment in terms of size, mass, area and imparted velocity. Without any input from the catalog, this process can be carried out relying on break-up models, involving a statistical approach. Hence, a break-up model is a statistical model that is able to describe the outcome of a fragmentation event in terms of statistical distributions. An alternative strategy is to follow the physical mechanisms governing the break-up in order to understand the characteristics and behaviour of fragments. However, determining the physical causes of the fragmentation can be challenging, especially due to the limited information available about the event's early stages.

A break-up model can be based on physical mechanisms exploitation, data from historical in-orbit break-up events, ground experiments, or a combination of them. According to these last, it is possible to identify three different categories of break-up models:

- Empirical models;
- Semi-analytical or semi-empirical models;
- Complex models.

Existing empirical debris models are basically curve-fits of limited data and are tenuously based on fundamental physics [14]. No physical conservation law is intrinsically ensured, but a proper implementation may consider it. They completely rely on in-orbit break-up and ground tests data. Their advantages are various since they are the simplest of models. Their computational time is very short and almost negligible. A full understanding of the fragmentation event is not required, instead, only a few inputs are necessary. On the other hand, the main disadvantage is that these models are only as efficient and robust as the accuracy of the data they rely on. This means that if the initial conditions of the event of interest diverge from the ones of the database on which the model is based, then the accuracy of the results will be questionable. However, the model's robustness can always be improved by expanding the collection of real events and experimental data on which it relies.

Semi-analytical models are a combination of empiricism and physics, representing an attempt to develop relatively fast-running and accurate debris cloud generation models [14]. They are based on theoretical expressions but are normally calibrated through the use of historical and/or experimental data. Hence, models in this category are applicable to a wider range of break-up scenarios, and since a more physically rigorous approach is implemented, their accuracy is better than the previous category [11]. The main disadvantage is the necessity of more input data, which is often not available, such as the energy of explosion or the collision geometry. Risky assumptions may degrade the accuracy of the results.

Complex models are based on fundamental physical principles and include hydrodynamic (hydro) codes and structural response programs [11]. They are the most accurate models and have the ability to represent any complex scenario. Unlike the two previous categories, which tend to generalise events that cannot be generalised because of their unpredictable nature and probabilistic driver, complex models provide a more precise and detailed representation of break-ups. They detail the break-up mechanism by employing continuum mechanics, impact physics and computer aided engineering. Moreover, full scale ground tests are an enormous effort to obtain a poor general dataset. With a complex model, it is possible to perform Hyper-Velocity Impact tests (HVI) through numerical simulations, like virtual experiment execution. They are able to generate "data sets" of break-up debris for the simpler empirical and semi-analytic models, improving their accuracy and expanding their applicability to a wider range of fragmentation scenarios [14]. Despite this, complex models require a significant amount of input data to accurately represent the physics of the event. These inputs are often not available or difficult to determine, which is a notable disadvantage. Using incorrect inputs may significantly reduce the accuracy of these models. Additionally, complex models have the disadvantage of requiring long computational times. Indeed, while empirical and semi-analytical models provide fast running times on small computers, complex models may take many hours to simulate a few seconds of a physical event on a high-performance computer [14]. Consequently, these complex models are often deemed unsuitable for operational scenarios.

Performing a trade-off between advantages and disadvantages of each category, empirical models are the most appropriate category to be used in an operational application because of their simplicity and low computational expense. Indeed, they are the most commonly used for both debris cloud and environment modelling [11].

The following paragraphs will provide an overview of the most well-known models for each category (see Table 2.1), discussing the main features.

NASA's Standard Break-up Model	**Empirical**
Aerospace Corporation's IMPACT model	**Semi-empirical**
ESA's PHILOS-SOPHIA model	**Complex**

Table 2.1: Break-up model overview

The main focus will be on the Standard Break-up Model (SBM) developed by NASA. It is a very simple empirical model and is absolutely the most used one. Debris Environment tools, like MASTER (ESA), EVOLVE 4.0 (NASA) and ORDEM (NASA), indeed rely on it. Then, IMPACT model developed by the Aerospace Corporation and PHILOS-SOPHIA by ESA model are discussed for completeness, even though they are not often used and not as fully documented in the literature as the SBM.

2.2 NASA's Standard Break-up Model

Since the 1970's, the NASA Orbital Debris Program Office has modeled the debris clouds generated by in-orbit explosions and collisions in terms of fragment size and velocity statistical distributions [15]. At the beginning, the treatable fragmentation scenarios were very limited and the initial conditions were highly constrained due to the presence of few and highly weak data sets. For this reasons, in 1997 NASA's standard break-up model revision began. This effort was part of the larger task to update the EVOLVE model itself, the long-term debris environment tool, and it was carried out by a team at the NASA Johnson Space Center [15].

The output of the current SBM describes the outcome of an explosion or a collision (catastrophic or non-catastrophic), providing statistical distributions of fragments in terms of characteristic length, area-to-mass ratio and imparted velocity. Since multiple break-up events of the same type of object will not produce exactly the same debris cloud each time, the break-up model should also account for variances about the derived distributions [15]. The input, instead, is event-dependent, as represented in the block diagram of Figure 2.1. In case of a collision, both primary and secondary mass and the resulting impact velocity are required. The latter is the relative velocity magnitude between the two colliding objects. In fact, this model does not provide any indication about the imparted velocity direction, because it provides only the $\Delta\vec{V}$ magnitude distribution. In the paragraph 1.2, it has already been stated that the speed direction is of not negligible importance for both the debris cloud evolution and collision probability estimation, since the along-track, radial and out-of-plane components affect different orbital parameters. However, to solve this issue, ejection velocity direction models must be involved. Instead, the explosion case requires a scaling factor, which is a parameter containing not only information about the parent size, but also about the type of explosion.

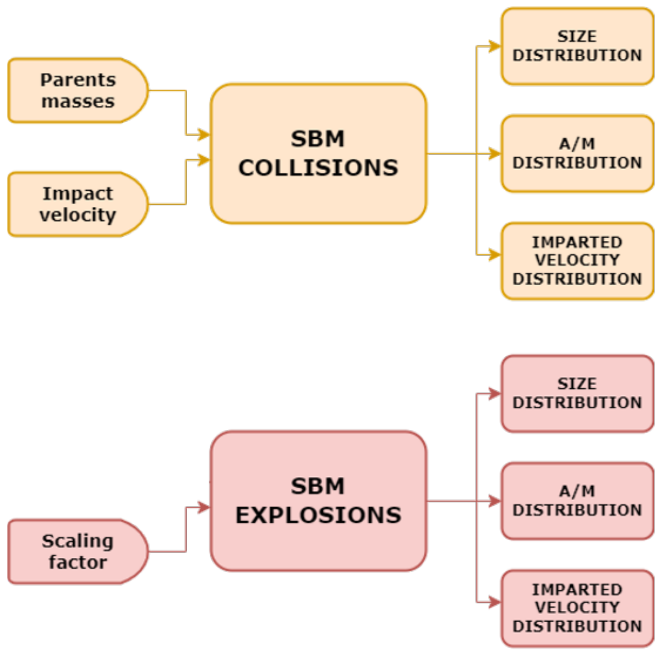

Figure 2.1: SBM's event-dependent input

The SBM depends on both historical in-orbit break-ups and ground experiments data since the early 1980's, including:

- The Solwind, and the USA 19 deliberative hyper-velocity collisions in LEO in 1985 and 1986, respectively;
- Orbital Debris Characterization Impact Test (SOCIT) series in 1991 and 1992 for fragments smaller of 8 cm of length;
- The Ariane upper stage sub-scale explosion tests by ESA;
- A series of historical orbital data (i.e., two-line element sets) for explosion and collision debris.

It is crucial to stress that the SBM is a purely energy-based model and does not consider the relative attitude between the two colliding objects nor the point of collision [9]. The collision is always assumed to involve the entire bodies of both parents. A spacecraft typically consists of multiple connected structures, like solar panels or gravity gradient booms. The result of a collision is clearly worse if the projectile hits the main platform than if it hits only a part of it. As a conclusion, the break-up model is characterised by an overestimate of the number of generated fragments.

The model supports both collision scenarios. In order to distinguish between catastrophic and non-catastrophic collisions, a kinetic-energy criterion is involved [4]. Equation 2.1 represents the kinetic energy normalised by the mass of the primary, expressed in [kg]. The impact velocity is the difference in magnitude between the primary and secondary orbit speeds and must be expressed in [km/s]. If this ratio is above the threshold of 40 J/g, then the event will be catastrophic. In the opposite case, the fragmented mass should be estimated. This step is fundamental to determine the fragmented mass, which strongly affects the distributions, as it will be clear soon.

$$\frac{\frac{1}{2} m_{Secondary} V_{Impact}^2}{m_{Primary}} > 40J/g \tag{2.1}$$

In the next paragraphs, a detailed discussion about the statistical distributions is provided. The working flow is also analysed, and a section is focused on ground experiments. The last subparagraph, instead, provides an overview of implementations and improvements of the model.

2.2.1 Size distribution

The size statistical distribution of the SBM allows to determine characteristic lengths and the total number of generated fragments. The characteristic length is a parameter that expresses the size of a debris and it is defined as the average of the three principal geometric axes of a fragment $L_c = (Lx + Ly + Lz)/3$ [4]. Previous NASA's break-up models involved mass as the independent variable in developing functions for the number of fragments generated [15]. The size or characteristic length of each fragment was then derived assuming particles of spherical shape. For objects smaller than 1 cm, the aluminum density was assumed, while, larger objects had a varying density according to Equation 2.2.

$$\rho(d) = 92.937(d)^{-0.74} \tag{2.2}$$

Where d is the fragment diameter, corresponding to the characteristic length. However, the spherical shape assumption is not very realistic, according to the unpredictable nature of a break-up event. The new version of the SBM involves the characteristic length L_c as the independent variable, since it allows to remove the sphericity assumption and can be more directly linked to both in-orbit and ground observations. Within the model application, L_c must be considered as a parameter to set. It is intended as the lower bound of the fragment size range, and it directly impacts the total number of generated debris.

The SBM models the cumulative number of fragments, i.e., the number of debris of size L_c or larger [15]. Since collisions and explosions occur by different mechanisms, two distinct distributions must be considered.

Based on numerous laboratory hyper-velocity impact tests, as the SOCIT series, and the in-orbit collision of the Solwind spacecraft, a power law distribution for the number of fragments generated by a collision of a given size and larger has been derived and described in Equation 2.3.

$$N(L_c) = 0.1m^{0.75}(L_c)^{-1.71} \tag{2.3}$$

In the above equation, L_c is in meters and m is defined as the total fragmented mass [kg], whose value depends on the type of collision, as shown by Equation 2.4. In case of a catastrophic collision, it would be the sum of the primary and secondary masses. While for non-catastrophic collisions, the fragmented mass is computed as the secondary mass scaled by the impact velocity [km/s] [15].

$$\begin{cases} m = m_{Primary} + m_{Secondary} & \text{if catastrophic} \\ m = m_{Secondary} V_{Impact} & \text{if non-catastrophic} \end{cases} \tag{2.4}$$

The cumulative number of fragments due to explosions is modeled through a power law distribution as well, expressed by Equation 2.5. In this expression, S is the scaling factor, which depends on the kind of explosion and the parent mass and it is a unit-less number. For upper-stages of 600-1000 kg, the scaling factor is fixed to 1 [15].

For both cases, the total number of generated fragments larger than a given L_c is obtained setting the desired minimum characteristic length. Obviously, the lower the set L_c, the higher the number of fragments generated.

$$N(L_c) = 6S(L_c)^{-1.6} \tag{2.5}$$

Figure 2.2 displays, in logarithmic scale, the size distribution for explosions proposed by the SBM compared to data from actual in-orbit explosions of upper-stages. All datasets exhibit quite strong conformity to the power law.

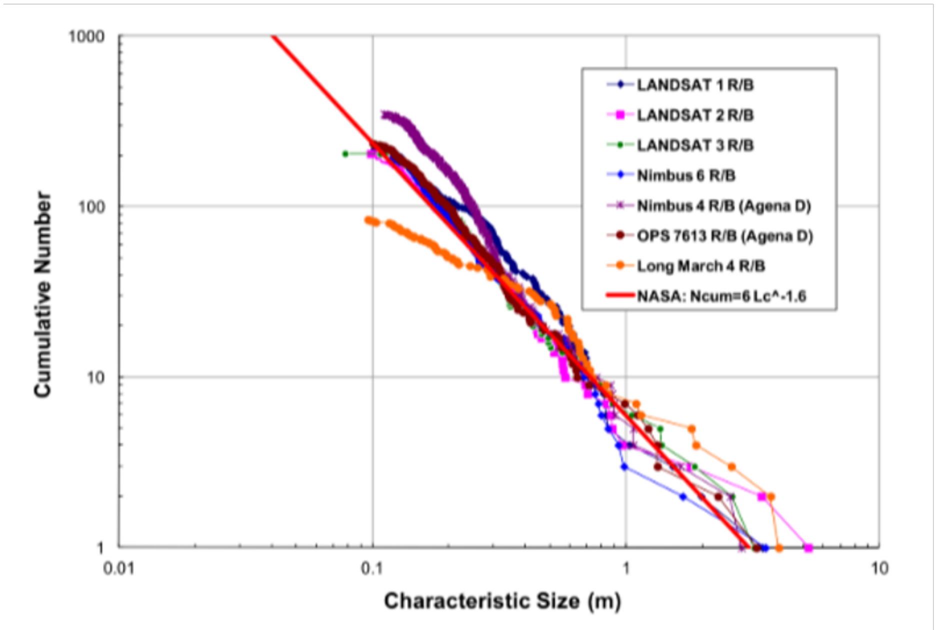

Figure 2.2: SBM's explosion size distribution compared to in-orbit data [16]

As it was stated earlier, explosions and collisions are two different mechanisms of break-up, and modeling both with a power law seems overly simplistic. In fact, a distinction between high and low intensity explosions may be considered [17]. High intensity explosions, and collisions also, tend to generate many smaller fragments, hence, a power law is coherent to this behaviour. Instead, the effect of low intensity explosions is the generation of a higher number of bigger fragments, hence, a power law is not consistent anymore. In this case, an exponential law is more suitable. However, an examination of in-orbit fragments generated by an explosion and of data collected in the well-known Atlas tank explosion, led to doubt upon the validity of this distinction [15]. This is the reason why the SBM is still relying on power law distribution of the cumulative number for both collisions and explosions scenarios.

2.2.2 Area-to-mass ratio distribution

The area-to-mass ratio A/m distribution is the most significant upgrade provided by the SBM's revision [15]. In the previous model, used by EVOLVE 3.0, a single value of A/m was involved. The A/m distributions have been developed for both spacecraft and upper-stages, and it has been possible thanks to an in-depth analysis of thousands of debris cataloged by the SSN and recorded from ground experiments.

Also in this case, the independent variable is the characteristic length L_c, but unlike the size distribution, a distinction between fragments generated by collisions and explosions is currently not supported.

Different A/m distributions are considered for distinct values of L_c. For fragments with characteristic length greater than 11 cm, the A/m distribution has been derived by analysing the decay rates of cataloged debris through a χ^2 fit [15]. The distribution is modeled as the sum of two log-normal distributions, where means and standard deviations are functions of $\lambda_c = log_{10}(L_c)$. Equation 2.6 and Equation 2.7 report the expressions and the coefficients of the distribution, respectively, for debris with L_c greater than 11 cm generated by rocket body fragmentation events.

$$D_{A/m}^{R/B} = \alpha^{R/B}(\lambda_c)N(\mu_1^{R/B}(\lambda_c), \sigma_1^{R/B}(\lambda_c), \chi) + (1 - \alpha^{R/B}(\lambda_c))N(\mu_2^{R/B}(\lambda_c), \sigma_2^{R/B}(\lambda_c), \chi) \quad (2.6)$$

$$\begin{aligned}
\alpha^{\mathrm{R/B}} &= \begin{cases} 1.0 & \lambda_c \leq -1.4 \\ 1.0 - 0.3571\,(\lambda_c + 1.4) & 1.4 < \lambda_c < 0 \\ 0.5 & \lambda_c \geq 0 \end{cases} \\
\mu_1^{\mathrm{R/B}} &= \begin{cases} -0.45 & \lambda_c \leq -0.5 \\ -0.45 - 0.9\,(\lambda_c + 0.5) & -0.5 < \lambda_c < 0 \\ -0.9 & \lambda_c \geq 0 \end{cases} \\
\sigma_1^{\mathrm{R/B}} &= 0.55 \\
\mu_2^{\mathrm{R/B}} &= -0.9 \\
\sigma_2^{\mathrm{R/B}} &= \begin{cases} 0.28 & \lambda_c \leq -1.0 \\ 0.28 - 0.1636\,(\lambda_c + 1) & -1.0 < \lambda_c < 0.1 \\ 0.1 & \lambda_c \geq 0.1 \end{cases}
\end{aligned} \quad (2.7)$$

Equation 2.8 and Equation 2.9 report the expressions and the coefficients of the distribution, respectively, for debris of the same characteristic length bin, but instead, generated by spacecraft fragmentation events.

$$D_{A/m}^{S/C} = \alpha^{S/C}(\lambda_c)N(\mu_1^{S/C}(\lambda_c), \sigma_1^{S/C}(\lambda_c), \chi) + (1 - \alpha^{S/C}(\lambda_c))N(\mu_2^{S/C}(\lambda_c), \sigma_2^{S/C}(\lambda_c), \chi) \quad (2.8)$$

$$\alpha^{\mathrm{S/C}} = \begin{cases} 0 & \lambda_c \leq -1.95 \\ 0.3 + 0.4\,(\lambda_c + 1.2) & -1.95 < \lambda_c < 0.55 \\ 1.0 & \lambda_c \geq 0.55 \end{cases}$$
$$\mu_1^{\mathrm{S/C}} = \begin{cases} -0.6 & \lambda_c \leq -1.1 \\ -0.6 - 0.318\,(\lambda_c + 1.1) & -1.1 < \lambda_c < 0 \\ -0.95 & \lambda_c \geq 0 \end{cases}$$
$$\sigma_1^{\mathrm{S/C}} = \begin{cases} 0.1 & \lambda_c \leq -1.3 \\ 0.1 + 0.2\,(\lambda_c + 1.3) & -1.3 < \lambda_c < -0.3 \\ 0.3 & \lambda_c \geq -0.3 \end{cases} \tag{2.9}$$
$$\mu_2^{\mathrm{S/C}} = \begin{cases} -1.2 & \lambda_c \leq -0.7 \\ -1.2 - 1.333\,(\lambda_c + 0.7) & -0.7 < \lambda_c < -0.1 \\ -2.0 & \lambda_c \geq -0.1 \end{cases}$$
$$\sigma_2^{\mathrm{S/C}} = \begin{cases} 0.5 & \lambda_c \leq -0.5 \\ 0.5 - (\lambda_c + 1) & -0.5 < \lambda_c < -0.3 \\ 0.3 & \lambda_c \geq -0.3 \end{cases}$$

Instead, for fragments with L_c lower than 8 cm, the A/m distribution is completely derived by SOCIT ground experiments. It is modeled as a single log-normal distribution, valid for both spacecraft and upper-stages (see Equation 2.10 and 2.11). In Section 2.4, concerns relative to the validity and applicability of SOCIT results are discussed.

$$D_{A/m}^{SOC} = N(\mu^{SOC}(\lambda_c), \sigma^{SOC}(\lambda_c), \chi) \tag{2.10}$$

$$\mu^{\mathrm{SOC}} = \begin{cases} -0.3 & \lambda_c \leq -1.75 \\ -0.3 - 1.4\,(\lambda_c + 1.75) & -1.75 < \lambda_c < -1.25 \\ -1.0 & \lambda_c \geq -1.25 \end{cases}$$
$$\sigma^{\mathrm{SOC}} = \begin{cases} 0.2 & \lambda_c \leq -3.5 \\ 0.2 + 0.1333\,(\lambda_c + 3.5) & \lambda_c > -3.5 \end{cases} \tag{2.11}$$

In all previous equations, the variable of the distributions is χ, expressed as the logarithm of the A/m value, while N represents the Probability Density Function (PDF) of a normal distribution, as reported in Equation 2.12.

$$
\begin{aligned}
\lambda_c &= log_{10}(L_c) \\
\chi &= log_{10}(A/m) \\
N &= N(\mu, \sigma, \chi) = \frac{1}{\sqrt{2\pi\sigma^2}} e^{\frac{x-\mu}{\sigma}}
\end{aligned} \tag{2.12}
$$

For fragments with characteristic length of $8cm \leq L_c \leq 11cm$, no distribution is referred to, hence a technique to close the gap should be implemented. A first approach is to compare a generated random number $\zeta_d \in [0.0, 1.0]$ with a value $\widetilde{\zeta_d}$, which can be derived from Equation 2.13.

$$
\widetilde{\zeta_d} = \begin{cases} 10(log_{10}(L_c/[m]) + 1.76) & \text{for rocket bodies} \\ 10(log_{10}(L_c/[m]) + 1.05) & \text{for spacecraft} \end{cases} \tag{2.13}
$$

If $\zeta_d > \widetilde{\zeta_d}$, then the fragment is assumed to belong to the larger group and consequently the bi-modal distribution is applied, otherwise, the single-mode distribution for smaller fragments is used [4]. The alternative approach, instead, consists modeling the gap between the two boundary lengths through an actual bridge function. The simpler method is to use a linear function [17][18], as shown by Equation 2.14.

$$
\begin{aligned}
&D_{A/m}^{BRIDGE} = \beta \times D_{A/m}(\lambda_c, \chi) + (1 - \beta) \times D_{A/m}^{SOC}(\lambda_c, \chi) \\
&\text{where } \beta = \frac{L_c - 0.08}{0.03}
\end{aligned} \tag{2.14}
$$

Since the distribution for bigger fragments is governed by the sum of two log-normal distributions, there is the presence of bi-modal behaviour of A/m for $L_c > 11cm$. Instead for smaller debris, this trend is not recorder because a single log-normal distribution is enough to model the A/m values. In fact, this feature is confirmed in Figure 2.3, where two peaks appear for greater characteristic lengths. It is of fundamental importance, in order to understand the workflow of the model, to underline that the area-to-mass ratio distribution directly depends on the characteristic length value. Starting from the value of area-to-mass ratio, it is possible to derive the mass and the cross-sectional area of each particle. The latter is linked to the characteristic length with a one-to-one correspondence, expressed by Equation 2.15.

$$
\begin{cases} A_x = 0.540424 L_c^2 & \text{for } L_c < 0.00167 \text{ m} \\ A_x 0.556945 L_c^{2.0047077} & \text{for } L_c \geq 0.00167 \text{ m} \end{cases} \tag{2.15}
$$

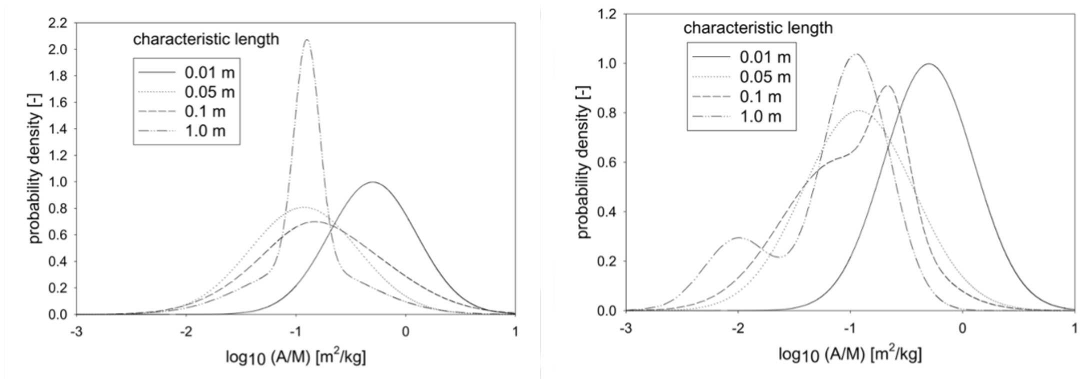

(a) Rocket body (b) Spacecraft

Figure 2.3: SBM's area-to-mass probability density function [17]: (a) rocket body, (b) spacecraft

Once this parameter is known, the mass of a fragment can be computed as following in Equation 2.16. This mass is a purely statistical quantity and the derivation does not consider the mass conservation principle at all.

$$m = \frac{A_x}{A/m} \tag{2.16}$$

It is worth to notice that the area-to-mass ratio distributions have been derived from the decay rates due to the aerodynamic drag, but for A/m values greater than $1m^2/kg$ the effect of the radiation pressure cannot be neglected. This means that the A/m is able to effectively derive the ballistic coefficient and, hence, the orbital lifetime, but determining the mass of a particle through a relationship with L_c is not so optimal [15].

2.2.3 Imparted velocity magnitude distribution

The imparted velocity distribution is the most important feature of a break-up model, since velocities are needed to initialise and propagate a debris cloud. Knowing the initial position and orbital speed of the parent and the additional ΔV imparted by the break-up, the state vector of each fragment can be built. NASA's Standard break-up Model is capable to provide to the user only the ΔV magnitude distribution. As it has already been stated in the paragraph 1.3 and at the beginning of the current section, the direction of the applied ΔV has a direct influence on the resulting trajectory, and consequently on the collision probability for a spacecraft. Hence, a model for the imparted velocity direction distribution must be adopted, as it will be explained in the paragraph 3.2.

SBM's velocity distribution has been derived thanks to in-orbit data for large fragments, and to ground tests data for smaller and not detectable particles [15]. The model supports the distinction between collisions and explosions, and uses the area-to-mass ratio as an independent variable instead of the characteristic length. Equation 2.17 shows the velocity distribution for collisions, while Equation 2.18 refers to explosions [15].

$$
\begin{aligned}
&D^{\Delta V}_{COL}(\chi, \nu) = N(\mu^{COL}(\chi), \sigma^{COL}(\chi), \nu) \\
&\text{where } \mu^{COL} = 0.9\chi + 2.9 \text{ and } \sigma^{COL} = 0.4
\end{aligned} \tag{2.17}
$$

$$
\begin{aligned}
&D^{\Delta V}_{EXP}(\chi, \nu) = N(\mu^{EXP}(\chi), \sigma^{EXP}(\chi), \nu) \\
&\text{where } \mu^{EXP} = 0.2\chi + 1.85 \text{ and } \sigma^{EXP} = 0.4
\end{aligned} \tag{2.18}
$$

Both distributions are modeled by a single normal distribution, where χ is the independent variable expressed as the logarithm of the ΔV (see Equation 2.19).

$$
\begin{aligned}
&\nu = log_{10}(\Delta V) \\
&\chi = log_{10}(A/m) \\
&N = N(\mu, \sigma, \chi) = \frac{1}{\sqrt{2\pi\sigma^2}} e^{\frac{x-\mu}{\sigma}}
\end{aligned} \tag{2.19}
$$

It can be noticed that the difference between collisions and explosions is not in the distribution type, but only on a scaling factor. In fact, Figure 2.4 shows that the two distributions have the same shape (since they are both log-normal), the same amplitude (since they have the same constant standard deviation value), but probability density functions for collision varying the A/m value are more separated from each other with respect to the explosions case.

Unlike the area-to-mass ratio distribution case, only the mean of the distributions is still a function of the the A/m, while the standard deviation is constant with A/m. It is worth highlighting that within the ΔV magnitudes derivation, the kinetic energy conservation law is not ensured, since the process is completely statistical.

2.2.4 Default workflow

Figure 2.5 is a block diagram representing the main steps of the SMB's workflow [9]. The diagram models the algorithm for collisions, but the explosions case is even simpler. Starting from the initial conditions, state vectors of both primary and secondary are required in order to compute the impact velocity as the norm of the relative velocity. State vectors can be reconstructed from the ephemeris of the parents or, if available, from the TLEs. Once the impact velocity is known, it can be used, along with the masses of parents, to apply the kinetic-energy criterion in order to determine the collision type and to compute the fragmented mass. This step is of fundamental importance, since it directly

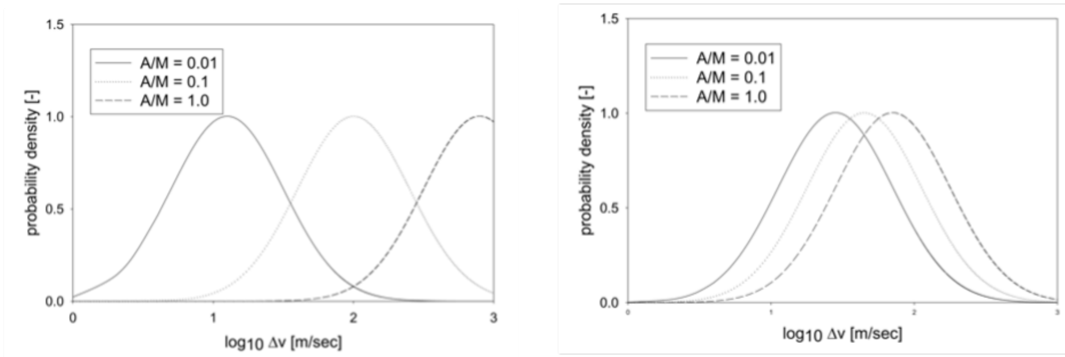

(a) Collision (b) Explosion

Figure 2.4: SBM's imparted velocity magnitude probability density function [17]: (a) collision, (b) explosion

affects the total number of generated fragments. Then, the distribution evaluation step can be carried out. In case of explosions, all steps before the distribution evaluation are skipped, since only the parent mass and the explosion type are needed to estimate the scaling factor, which is the only input required to compute the total number of generated fragments. At the end of this process, each fragment will be characterised by a size (L_c), an area-to-mass ratio (hence an area and a mass) and an imparted velocity magnitude. A proper implementation may also provide imparted velocity directions. In this case, a state vector for each fragment can be derived, where the position is given by the break-up event location (it is the same for every fragment), and the orbital velocity is determined summing the received imparted velocity to the initial orbital speed (parent velocity before the fragmentation event).

Figure 2.6 reports a focus on the distribution evaluation step of the previous diagram, i.e., fragments extraction. Once the event type is known, a distribution between the explosion and collision case must be selected. For both cases, according to Equation 2.3 and 2.5, the characteristic length is the only missing parameter. As already stated in the previous paragraphs, it must be intended as a minimum length to set. For historical reasons linked to the detection capabilities of sensor networks, the model assumes L_c = 10 cm as a lower bound. However, the SBM is validated for debris size up to L_c = 1 mm [4]. Once the user has set a minimum L_c value, the total number of generated debris can be estimated from Equation 2.3 or 2.5, according on wheter the event is a collision or an explosion, respectively. As many fragments will be extracted as the total number calculated previously, where for extraction it is meant the characterisation of each individual fragment. Each extraction is characterised by 6 steps. First, a characteristic length value is randomly selected from the proper size distribution. As already stated in the paragraph 2.2.2, a given L_c value corresponds to a specific area-to-mass ratio distribution, from which an A/m is randomly extracted. The fragment average cross section can be computed through Equation 2.15, knowing L_c, and given an A/m value, the mass of the debris can be computed. Each individual mass must be added to the total fragmented mass. Finally, for a given area-to-mass ratio value, a particular imparted velocity distribution exists, from which a ΔV magnitude is randomly extracted. If direction is also known, it is possible to derive the perturbed state vector for that fragment. The process ends when the number of extracted fragments has reached the total number of generated fragments computed at the first step.

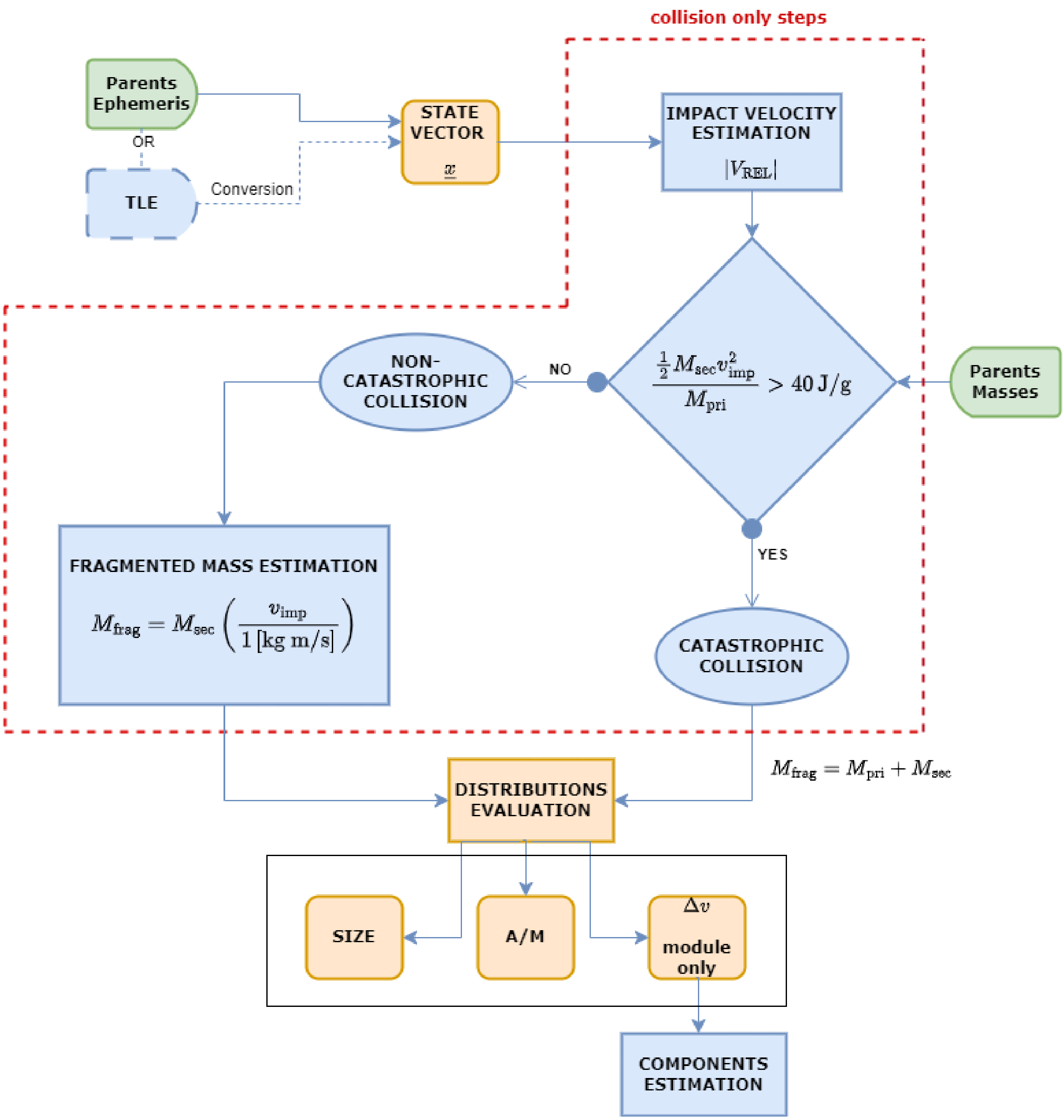

Figure 2.5: Workslow of NASA's SBM

From this purely statistical workflow, it is evident that no conservation law is ensured. An important observation can be made: since the total number of generated debris is only a function of the minimum L_c, which is set by the user, and the scaling factor or the fragmented mass, two different events characterised by the same input will produce exactly the same number of fragments. It should be obvious that this is a quite hazardous and physically unrealistic assumption, given the unpredictability of a fragmentation event.

The implementation of mass conservation represents a valid solution to this physical incoherence. The check on the mass must be performed when the extraction of all possible fragments is completed, so that the workflow is not affected by this modification. If the sum of all extracted masses is lower than the initial computed fragmented mass $m_{output} < m_{input}$, then extractions of new debris must continue. In the opposite case, $m_{output} > m_{input}$, a filtering step must be applied. The latter can be designed following various criteria, for example:

- Removing fragments with small or massive L_c;
- Removing fragments with negative semi-major axis, corresponding to hyperbolic orbits;
- Removing fragments of altitude below a given threshold (120 km), since they will decay.

The two last fragments categories can be filtered out because, in a collision risk assessment scenario, fragments with hyperbolic trajectories or too low altitude are not of interest, since they do not affect the application. In this way, two distinct events with the same input may generate a different number of debris.

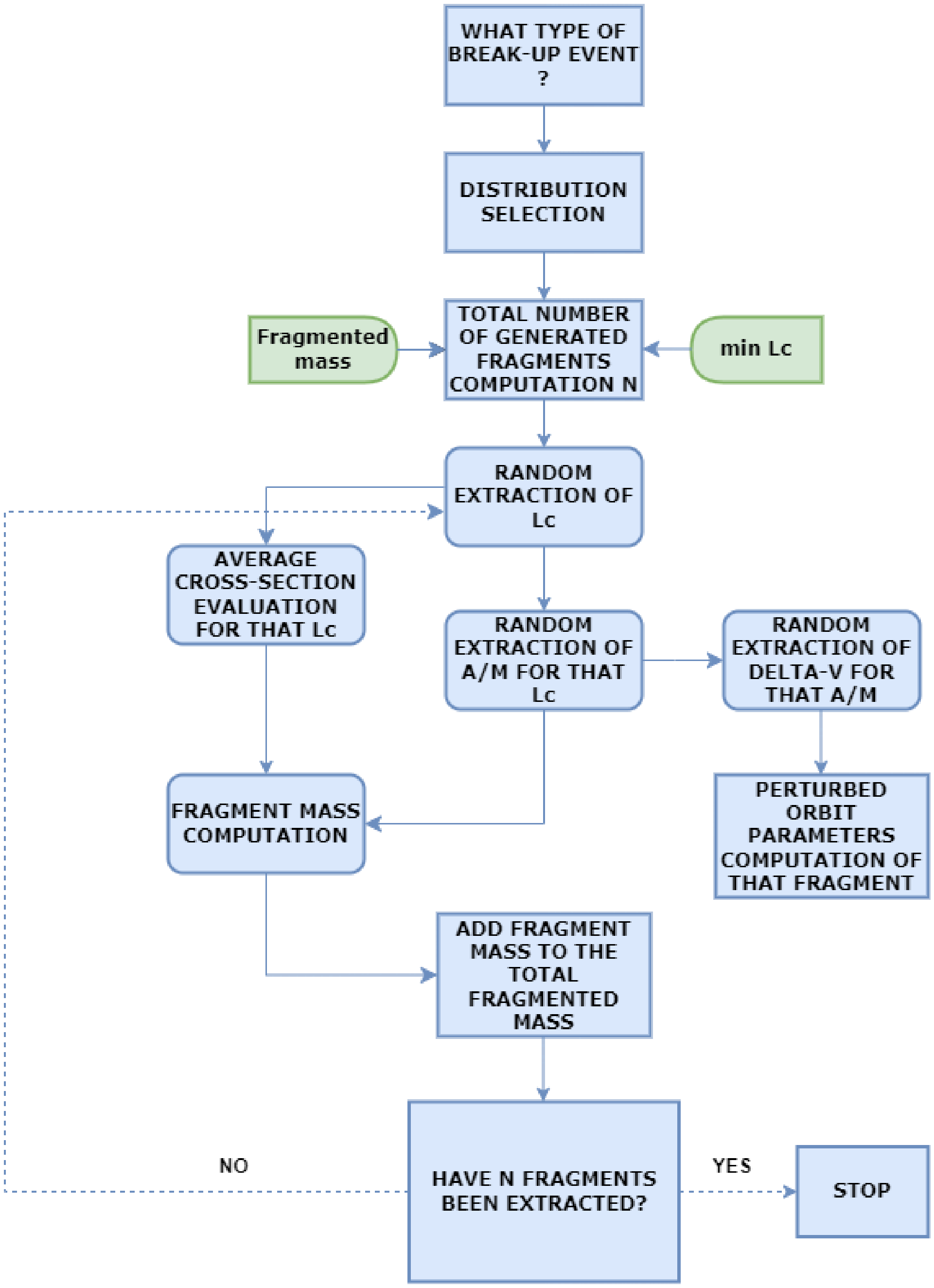

Figure 2.6: Fragments extraction process of NASA's SBM

2.2.5 Implementations and improvements

Although no official SBM's implementation is available on the internet, numerous attempts have been made by third parties. This enables the existence of a collection of slightly different implementations of the same model, based on the same statistical distribution but with a diversity of methods of ensuring conservation laws. The most complete open-source and validated code that is worth to be cited is the one developed in C++ by [18], born with the purpose to remove the incompleteness and lack of clarity of previous open-source implementations. Not only all possible event cases are implemented following the basic guidelines given by original empirical distributions, but mass and momentum conservation are enforced. After the execution of the default extraction of fragments, if the total output mass is above the fragmented mass value, some debris are deleted until the maximum mass is reached. While the latter process is an obligation, if the total generated mass is below the initial value, the mass conservation can be enforced optionally by the user. If selected, the extraction of new fragments continues until the threshold is reached. Furthermore, the C++ implementation performs direction assignment to imparted velocity magnitudes extracted by the relative distribution. The directions distribution is assumed to be isotropic hence, velocity vectors are uniformly distributed in azimuth and elevation.

Kinetic energy is still not ensured in this version, but a tool developed by ESA is capable to also perform these checks. The software in question is FREG tool, which is embedded in the FREMAT software (Fragmentation Event Model and Assessment Tool). For completeness, the primary tool consists of three components, with the first one being the Fragmentation Event Generator (FREG) capable of simulating fragmentation events. The subsequent one is the Fragmentation Events on Spatial density Tool (IFEST), developed for long-term debris evolution. The last one is the Simulation of On-Orbit Fragmentation Tool (SOFT), which has the purpose of extracting debris information like parent object identification from actual observed fragmentation events. FREG follows the guidelines given by NASA's SBM, asking for the same inputs but employing some additional mathematical and statistical functions, such as mass, momentum and kinetic energy conservation. The strategy to enforce mass conservation is to reject the most massive fragments until the final mass is equal to or lower than the initial one. If after this process, the final mass is lower than the initial one, an additional fragment whose mass matches exactly the mass gap is added. In contrast to the original NASA's standard break-up model that does consider a single debris cloud, FREG tool adopts a two-clouds approach for collisions. Two sub-collision clouds are considered and centered in the two CM of the two parents that will be treated separately. Then, it solves the conservation of momentum by distributing the ejection velocity vectors uniformly around the center of mass of each parent object. The kinetic energy conservation is enforced through an estimation of the energy loss. A hyper-velocity impact, such as a collision, is not really an ideal elastic impact, hence the energy is not actually conserved. If the total energy is greater than the initial value, spread velocities norms are scaled downward until the energy is conserved (assuming a null loss, which is physically not correct), while if the total energy is lower than the initial one, the difference is assumed to be the energy loss and no scaling actions are applied.

Another example of SBM implementation and upgrade is provided by the work presented in [9]. The latter proposes an iterative approach to estimate the model inputs, particularly focusing on the masses of the parent bodies involved in a collision event. The iterative process leverages the knowledge of Two Line Elements (TLE) of the fragments at a specific time after the event to adjust the input parameters of the breakup model. The objective is to achieve a realistic number of fragments within a certain tolerance.

The above versions show that NASA's standard break-up model is constantly improved in various aspects.

2.3 IMPACT model

IMPACT is a semi-analytical break-up model developed by the Aerospace Corporation, whose fundamental relationships are primarily informed by ground test and on-orbit collision and explosion data from several decades and, notably, data from the 2014 DebriSat hyper-velocity ground test [19]. In contrast to NASA's SBM, it enforces boundary conditions and conservation laws, such as mass, momentum and kinetic energy to ensure self-consistent results and prevent physically impossible outputs. Both collision and explosion scenarios are implemented.

2.3.1 Energy transfer

The initial step involves the estimation of the kinetic energy variation in the debris cloud motion from the pre-collision and post-event state vectors. The variation is caused by the associated kinetic energy loss and, in case of collision, momentum transfer. In case of explosion, the debris cloud has the center of mass that continues to follow the parent orbit. The model includes three types of objects representing the target and the projectile, if needed:

- Boosters, characterised by the tendency to generate a few very large particles and a number of smaller particles;
- Satellites, characterised by the tendency to generate a larger number of fragments than the one produced for a booster, since they are basically solid bodies with no internal large open volumes;
- Post-boost vehicles, with the satellite's characteristics of being solid bodies and the booster's tendency to produce a few numbers of very large intact debris.

Depending on which object is selected, the model assumes a percentage of its mass to remain intact. The energy transfer for collisions involves the computation of the energy loss as the fraction of total available kinetic energy used to fragment the objects, spread pieces and generate light and heat. The energy loss causes a shift of velocity vectors of the centers of mass of the two debris. The post-collision relative velocity of both target and projectile is a function of the energy loss. The energy transfer for explosions is much simpler: for the momentum conservation, the velocity vector of the debris cloud center of mass is the same as the parent center of mass velocity. The energy for heat, light, body fragmentation and pieces spreading is provided by the energy of explosion itself. The energy released by the explosion must be completely dissipated through at least one of these forms.

2.3.2 Mass distribution

In contrast to the SBM size distribution that uses the characteristic length as an independent variable, IMPACT involves a mass distribution, with the mass as the independent parameter. For collisions, the cumulative mass distribution is a power law, expressed by Equation 2.20, where the exponent is a function of the impact kinetic energy and the scaling constant is an empirical parameter.

$$N(m) = a\left(\frac{m}{m_{Tot}}\right)^{-b} \tag{2.20}$$

When the collision does not involve a great value of kinetic energy, hence the collision is more likely to be not catastrophic, the model considers a larger portion of the target mass to remain intact. Only the residual mass follows the appropriate power law. This situation can also occur in explosion events where the energy released is not enough to fragment the entire object. IMPACT includes another type of event, which is the partial collision, i.e., an event that does not involve a body-to-body impact. This is similar to non-catastrophic collisions, but the energy loss is typically reduced.

The cumulative mass distribution for explosion is, instead, modelled as an exponential law, expressed by Equation 2.21, where again the exponent b is a function of the impact kinetic energy and the scaling constant a is an empirical parameter.

$$N(m) = ae^{-b\sqrt{m}} \tag{2.21}$$

Hence, IMPACT model still considers the fact that explosion events may tend to generate larger fragments, since they tend to have lower energy than collisions.

2.3.3 Imparted velocity distribution

Once fragments are characterised by individual masses and the event energy is specified by the user, spread velocities for each fragment can be determined. The total spreading energy is distributed among mass bins using the concept of equipartition of energy, which assumes that each fragment receives the same amount of kinetic energy. The velocity norm associated with each mass bin is determined as a function of the mass and characteristic velocity of the largest mass bin (m_0 and V_0), as expressed by Equation 2.22.

$$V_i = \sqrt{\frac{m_o}{m_i} V_o^2} \tag{2.22}$$

Once the characteristic velocities for all mass bins have been determined, spread velocity magnitude distributions are applied to each of the mass bins to determine velocities of individual fragments. The distributions in question are beta distributions, expressed by Equation 2.23, where A is a scaling constant and α and β are shape parameters.

$$\begin{aligned} &D(x) = Ax^{\alpha-1}(1-x)^{\beta-1} \\ &\text{where } x = \frac{V}{V_i} \end{aligned} \tag{2.23}$$

IMPACT model is capable of also attributing directions to spread velocities, in contrast to the magnitude only imparted velocity distribution of NASA's model. The spread velocity vectors distribution is assumed to be spherically symmetric (isotropic) about the post-fragmentation ECI velocity vector of the debris cloud's center of mass. This approach is supported by the observation that high-energy break-up may not show regular patterns of asymmetry, hence, the isotropic assumption is conservative. The algorithm to assign directions uniformly is based on sampling a sphere by subdividing the faces of an icosahedron. A direction for each fragment is chosen randomly and then, it is scaled by the appropriate spread velocity magnitude to generate the spread velocity vector of each fragment. Within the process of direction assignment, the momentum conservation is also implemented. While many fragmentation events are well-represented by an isotropic distribution, some occurrences tend to spread fragments in preferred directions. For this reason, the asymmetrical velocity computation option was developed. The spread velocity directions are assigned, enabling the appropriate conservation of momentum. The resulting imparted velocity distribution is no longer symmetric but still maintains the appropriate momentum and energy distributions.

2.3.4 Size characteristics distributions

At this point, it should be obvious that IMPACT is a purely energy-based model, hence the size of fragments is not an interesting parameter to obtain the spread velocity distribution. However, associating sizes to fragments extracted within the model is very useful, since are visible by radars or other sensors. Overall, the size of a fragment is a fundamental parameter for the long-term behaviour of a debris cloud, since the ballistic coefficient depends on it, hence the area-to-mass ratio. For these reasons, IMPACT model also involves the derivation of size characteristics distributions. This process is based on empirical data, and includes fundamental thickness, fundamental area, width-to-length ratio, apparent thickness and area-to-mass ratio distributions as output.

2.3.5 Comparison between IMPACT and NASA's SBM

The integration of conservation laws makes the result of the break-up model more consistent in relation to the event physics. Based on this, a semi-analytical model, such as IMPACT, is able to provide a more realistic characterisation of the debris cloud with respect to the purely statistical and empirical output of an empirical fragmentation model. Furthermore, IMPACT model can be applied for a wider range of fragmentation scenarios. However, to achieve these better results, more inputs are required. Firstly, since it is an energy based model, an estimation of the break-up energy is necessary. This is a critical point, since it is very hard to obtain detailed information about a fragmentation event, overall in the short-term. Hence, the risk of making a not coherent assumption on the energy value translates into the risk of losing the model's advantages. Also, for spread velocity directions and area-to-mass distribution evaluation, information about the preferred ejection direction and materials is needed.

As a conclusion, the advantages on the quality of the debris cloud charcaterisation that IMPACT model provides can be exploited only when a good knowledge of many more inputs is available.

2.4 Ground experiments

Before introducing complex break-up models and to conclude the discussion about empirical and semi-analytical ones, an overview of ground experiments is provided. As already stated in the previous paragraphs, empirical and semi-analytical break-up models may rely on fragments database obtained through hyper-velocity impact tests on ground, in addition to data of real in-orbit break-ups, especially for smaller fragments. The reason is the fact that small particles from space cannot be accurately observed by ground sensors. In this paragraph, the two previously cited ground experiments, the SOCIT series and the DebriSat Project, are presented.

2.4.1 SOCIT series

The Satellite Orbital Debris Characterization Impact Test (SOCIT) series is a sequence of four hyper-velocity impact tests, conducted at Arnold Engineering Development Center (AEDC) in 1991/1992 [20]. The fourth test (SOCIT4) has provided the data to describe the area-to-mass ratio and imparted velocity distributions for small fragments, used in the 1998 NASA Standard Break-up Model. In the latter experiment, the break-up of a flight-ready payload was performed, the U.S. Transit navigation satellite, shown by Figure 2.7, through a collision. The target satellite was a cylindrical octagon of 46 cm in diameter and 30 cm of height, weighting 34.5 kg. The projectile was a 2024 aluminum solid sphere of 4.7 cm of diameter and a weight of 0.15 kg. The Transit was suspended by cables from the ceiling of a test chamber, surrounded by ten stacks of multi-layered polyurethane foam mounted on plywood. The collision occurred near the center of Transit panel with an impact velocity of 6.1 km/s. The recorded energy-to-mass ratio was of 78 J/g, well above the 40 J/g threshold of the kinetic-energy criterion to determine the collision type. With that value, the collision is defined as catastrophic. Indeed, both the target and the projectile were completely fragmented. Most of the mass ended up in many large fragments, which were collected from the laboratory floor. Less than 5% of the total mass was destroyed, and intact debris from sub-millimeters to several centimeters of size were generated by the remaining mass and were delivered to the General Research Corporation (GRC) and to Kaman Sciences for further analysis. In all, 4762 fragments were recorded in the 1995 database. Particles were divided into 10 shape categories (flat plate, curled plate, box, sphere, flake, rod, cylinder, box and plate, other and nugget) and into 6 material categories (aluminum, steel, copper, phenolic/plastic, fiber/glass and other).

Although the SOCIT4 database was a effort required to model smaller fragments as well, it was subject to a non-negligible limitation. SOCIT tests were performed with satellites from the 1960s, an epoch in which space platforms were built with traditionally heavy materials. This means that the database is not really representative of break-up events that occurred between new generation spacecraft, which involve much lighter and high-performance materials [20]. As a consequence, the characterisation of small debris of a cloud generated from a modern spacecraft fragmentation may be inadequate.

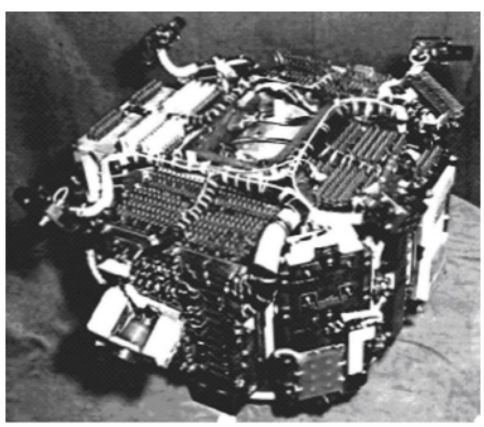

Figure 2.7: SOCIT4 Transit spacecraft [20]

2.4.2 DebriSat project

As new materials and construction techniques have been adopted for modern space platforms, the need for new laboratory-tests to improve the existing DOD and NASA's break-up model has grown. The necessity of such tests was supported also by discrepancies between model predictions and observations relative to fragmentation events of modern satellites, including the Iridium 33 and Fengyun 1-C. Hence, a new ground experiment, called the DebriSat Project, was performed in 2014 as a collaboration of the NASA Orbital Debris Program Office (ODPO), the Air Force Space and Missile Systems Center (SMC), the Aerospace Corporation (Aerospace), the University of Florida (UF), and the Air Force Arnold Engineering Development Complex (AEDC) [21].

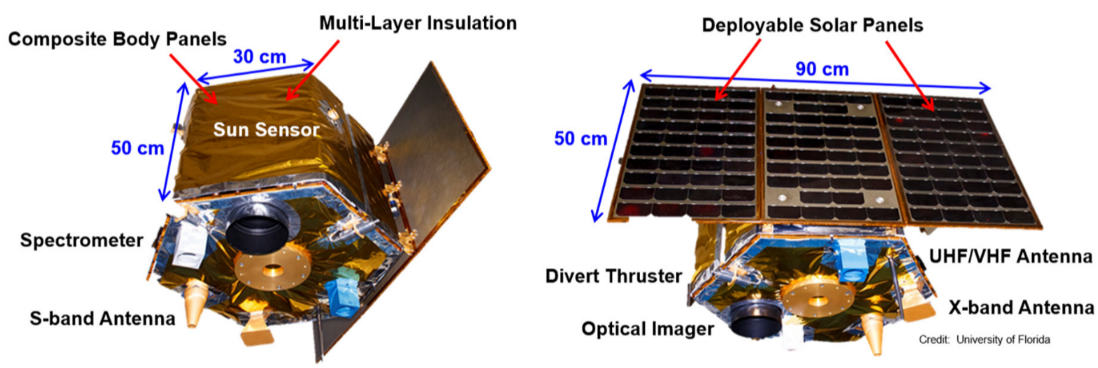

Figure 2.8: DebriSat design [22]

The project had four objectives:

1. Designing and building a 56 kg satellite, representative of new generation satellites in LEO environment (see Figure);
2. Conducting a hyper-velocity impact test (HVI) to simulate a catastrophic collision;
3. Collecting and classifying generated fragments down to 2 mm in size;
4. Deriving new coefficients to improve DOD and NASA existing break-up models.

To increase the success of the project, a launch vehicle upper stage (DebrisLV) was built and used as a target for a second HVI test. The projectiles were hollow aluminum cylinders of about 600 g of weight, embedded in a nylon cap. Both collisions occurred with an impact velocity of about 7 km/s, and classified as catastrophic collisions.

Once all possible fragments have been collected and stored, the charcaterisation process began. Each fragment's physical (observed and derived) parameters were archived in the DebriSat Categorization System (DCS), which is a database solution designed specifically to manage the large amounts of data generated by the DebriSat project.

A comparison against the classic NASA break-up model (which includes only SOCIT data) was performed [22]. The characteristic length distribution derived from the DebriSat database well matches the SBM's size distribution. The area-to-mass ratio distribution with respect to the characteristic length of the DebriSat data is analysed for low, medium, and high-density fragments. In all cases, the SBM mean appears to be lower than the DebriSat results. All comparison graphs are reported in the work presented in [22]. In conclusion, the new DebriSat database appears to agree with NASA's Standard Break-up Model, despite some discrepancies in the area-to-mass distribution. Although a direct study on the effect of the ejection velocity distribution caused by DebriSat data has not been conducted, it can be inferred that it also deviates from NASA's model, as it is directly linked to the area-to-mass distribution.

However, an open-source implementation of the NASA or DOD models, including the DebriSat database, is not currently available and the fragments collection and classification is not concluded yet.

2.5 PHILOS-SOPHIA model

PHILOS-SOPHIA is a software tool developed as a collaboration of the Fraunhofer Institute for High-Speed Dynamics and the European Space Agency. It allows the user to perform hydrocodes simulation of hyper-velocity collisions in orbit, hence, it is an implementation of a complex break-up model [23]. It is based on the well assessed EMI-hydrocode SOPHIA as solver, which has been developed for analysing impact fragmentation within the context of missile defence, hence it can only treat hyper-velocity collision applications. This model works also considering the interaction between generated particles.

SOPHIA couples a meshless smoothed particle hydrodynamics (SPH) method with a mesh-based finite element method (FEM). The latter method is often used in structural dynamics computation, but when simulating impact processes, severe deformations may occur that heavily distort the mesh, leading to a reduction in calculation accuracy. The meshless SPH method does not suffer from such limitations, but the computational effort is significantly higher. The coupled FEM-SPH approach of SOPHIA starts with a pure FEM model in which distorted elements are converted into particles. Alternatively, deleted elements may also be replaced by simple mass points, also referred to as eroded nodes. Eroded nodes carry the mass and linear momentum of the eroded elements and interact with other surface elements but not with each other.

The PHILOS-SOPHIA solver has been tested and validated against numerous hyper-velocity impact experiments, comparing the results with the debris cloud formation in high-speed recordings. The work presented in [23] proves that PHILOS-SOPHIA is able to reproduce complex impacts, since the code results precisely match the debris cloud behaviour. The solver has also been crosschecked with commercial hydrocodes of general purpose, such as ANSYS AUTODYN. Similar results of the mass distribution of fragments have been found, but PHILOS-SOPHIA better matched the experimental measured velocity of the cloud. Furthermore, PHILOS-SOPHIA needed less computation time than commercial software.

2.5.1 Comparison between PHILOS-SOPHIA and NASA's SBM

The work of [23] selects different collision scenarios to perform a comparison against NASA's SBM. The cases present various energy-to-mass ratio, colliding objects size, impact geometry, and impact point, and each one occurs with an impact velocity of 11 m/s. For the case of an oblique impact of a 12U Cubesat of 10 kg, less fragments are generated by the hydrocode with respect to the SBM prediction. However, they seem to follow the same slope as the empirical model. For what concerns the area-to-mass distribution, hydrocode values quite match the SBM distribution, showing a tendency towards higher values. Furthermore, the variation from the mean is lower than the standard deviation predicted by the SBM. A comparison against the other configurations shows that distributions are directly influenced by the collision geometry and this effect is completely neglected by NASA's SBM. All collision scenarios are presented in [23].

The PHILOS-SOPHIA tool offers various advantages as a complex model. More accurate results are obtained, since it considers the actual physics of the event and for the same reason it is characterised by the ability to model any complex event, making it suitable for an incredibly wide range of scenarios, in contrast to the strong limitations of empirical models. However, it shows some very important features that translate into disadvantages and limitations. First of all, it requires a much higher number of inputs, often not accessible, such as the collision geometry and the impact point and knowledge of continuum mechanics, impact physics, and computer aided engineering is needed. Then, even if the user is able to set the simulation to include all required inputs, the problem of very high computational time can not be solved and is not negligible. Although PHILOS-SOPHIA achieves a significantly shorter computational time compared to other commercial hydrocodes (9 hours versus 27 hours for 20 μs of simulated physical time), it is still not a fast-running model, which limits its operational usability.

–3–
Debris cloud evolution over time

In the previous chapter, it has been shown how break-up models are able to describe the outcome of fragmentation. In particular, NASA's standard break-up model provides characteristic length, area-to-mass ratio and ejection velocity magnitude distributions of fragments. The output of this break-up model can be seen as the initial conditions of the debris cloud just after the fragmentation. Once a debris cloud has been characterised in these terms, the analysis of its dynamical evolution over time can be performed. The primary objective of this chapter is to identify and understand the assumptions and conditions that occur during the short-term phase, which is the specific time window to compute the debris cloud probability of collision targeted by the tool.

In this chapter, a detailed description of evolution phases is provided, with a focus on which perturbation affects the cloud's behaviour the most. Another section aims at investigating the effect of the imparted velocities on the initial orbit parameters of fragments. After an overview of possible ejection velocity direction models, a break-up is simulated and analysed with the purpose of demonstrating the cloud's dynamics in each phase. Orbital perturbation effects are considered individually and a study on the decayed fragments is also carried out. Finally, a procedure to compute the duration of the short-term phase is outlined.

3.1 Phases of debris cloud evolution

The request for a computationally fast model for space debris cloud evolution has always forced a number of simplifying assumptions to be made to make the problem manageable, almost always made at the expense of accuracy [24]. The most intuitive way to follow the dynamics of a cloud over time is to consider each fragment individually. Using the magnitude and direction of the fragment ejection velocity, the orbital position and velocity of the parent at the time of break-up (i.e., at the break-up point), post break-up state vectors of each fragment can be computed, meaning new orbits of fragments caused by the event are determined. The orbits of the individual fragments can then be evolved using a standard orbit propagator. Since fragmentation events may generate up to millions of debris, a lower limit on debris size has to be set to decrease the computational expense of this approach and it can, for example, be taken according to the minimum trackable debris size [24]. An alternative approach consists of treating the cloud as a continuum, which means considering it as a three-dimensional envelope in space that contains all the debris. In this case, the parameters under study are the debris density and cloud volume over time. The last procedure is only suitable for medium and long-term phases, as it will be clear soon.

In any case, cloud evolution models can be classified with respect to the length of time after the fragmentation that they are valid for, or the period of the cloud's lifetime they aim at simulating. Within the orbital debris community, three main phases are identified:

- Short-term phase;
- Medium-term phase;
- Long-term phase.

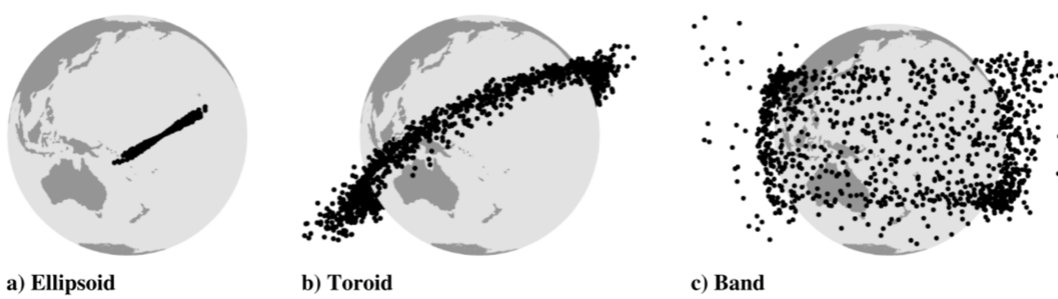

Figure 3.1: Debris cloud evolution phases [25]

Short-term refers to the time just after the break-up, in which the cloud has an ellipsoid shape, meaning that fragments are still quite close to the parent. Due to ejection velocity caused by the break-up, the orbital periods of fragments are changed. Consequently, fragments start to gradually spread all along the entire orbit. The cloud behaviour can also be explored in terms of orbital parameters distributions. In particular, the true anomaly distribution of fragments has initially only a bias with respect to the parent value, but it will go towards the randomization as fragments spread along the orbit. On the other end, the argument of perigee and the right ascension of the ascending node distributions still have a bias with respect to the initial break-up values. The reason for this behaviour lies in the fact that all orbital perturbations can be neglected during this phase, because the only driver is the effect due to the ejection velocities. The short-term phase usually lasts some hours and it ends when the true anomaly randomization is reached, which marks the cloud's transition into a closed toroid. Without any orbital perturbation, the toroid presents a pinch point at break-up position. This is a direct effect of the fact that, under Kepler's motion assumption, all fragments must pass through the break-up point, but not necessarily at the same time. Similarly, a pinch line occurs along the radial in the parent orbit plane 180° from the pinch point because all debris must pass through the orbit plane along this line [24]. Since the cloud volume collapses to zero, or more precisely to a minimum value, at the pinch point, identifying pinch zones is important because these regions have a high debris density and pose a significant collision threat to orbiting objects passing through them. Without the effects of orbital perturbations, the cloud would keep the pinched toroid shape indefinitely. In reality, perturbing forces are present and significantly affect the medium and long-term evolution of the cloud [11].

Medium-term phase starts just after the formation of the closed toroid, when the true anomaly is already random, while the right ascension of the ascending node and argument of perigee are still only biased. This phase is completely governed by $J2$ perturbation. The Earth's oblateness has two main secular effects, expressed by Equation 3.1 and 3.2. Firstly, it causes the precession of the argument of perigee, rotating the apsidal line of the debris orbits in their orbital planes. Secondly, a precession in the right ascension of the ascending nodes is registered.

$$\frac{d\omega}{dt} = \dot{\omega} = \frac{3}{2} J_2 \frac{R_E^2}{p^2} n \left(2 - \frac{5}{2} \sin^2 i\right) \tag{3.1}$$

$$\frac{d\Omega}{dt} = \dot{\Omega} = -\frac{3}{2} J_2 \frac{R_E^2}{p^2} n \cos i \tag{3.2}$$

As both precession rates depend on the semi-major axis, inclination and eccentricity of the specific orbit, the variations are different for each fragment. As a consequence, these two parameters start to spread along the orbit, going towards the randomization. This causes the toroid to be slowly dismantled and become a band surrounding the Earth, whose latitude is limited by the inclination of the parent orbit. At the end of this phase, the true anomaly, argument of perigee and right ascension of the ascending node are all random distributions. The medium-term phase usually lasts several months or years, but its duration is strongly affected by initial conditions of break-up.

Long-term phase starts just after the band formation. Since all three distributions are already random, the $J2$ perturbation effect is not visible anymore and, as a consequence, can be neglected. On the other hand, it is finally possible to consider the atmospheric drag, whose only effect is to reduce the debris cloud density. It causes fragments to de-orbiting, but its effect is highly dependent on the altitude and initial conditions of the break-up.

Figure 3.1 provided by [25] shows the debris cloud shape in each phase. The process to switch from the toroid to the band is not instantaneous but very slow and progressive, which could take several years. Therefore, a transition phase is added to cover the period in which the different nodal precession rates start to open the tours at the equator. At beginning, the density will be higher at high latitudes, since pinch zones are present, as shown in Figure 3.2 provided by [26].

Figure 3.2: Bridge-phase of debris cloud evolution: open toroid [26]

Hence, each phase has different geometry and driving forces. Since the only driver during the short-term is the change of orbital energy due to the imparted velocity distribution, the early dynamics of the system can be studied by applying Kepler's motion assumptions. It is worth mentioning that the thesis' objective is to compute the debris cloud probability of collision during the short-term phase, so we are interested in understanding conditions and assumptions occurring in this time window.

Actually, the Earth's oblateness, represented by the $J2$ zonal armonic, has another important secular effect. The precession rate of the mean anomaly is expressed by the following equation.

$$\frac{dM}{dt} = \dot{M} = n\left[1 + \frac{3}{2}J_2\frac{R_E^2}{p^2}\sqrt{1-e^2}\left(1 - \frac{3}{2}\sin^2(i)\right)\right] \tag{3.3}$$

However, this effect is not really visible in any evolution phase, even if its changing rate is three orders of magnitude higher compared to the argument of perigee and right ascension of the ascending node precession rates ($\dot{\Omega} = \dot{\omega} = O(10^{-3}\dot{M})$), thus it varies much faster. Therefore, when orbit parameters are visualised in the long term, the mean anomaly would have already been randomised for a long time due to $J2$. However, its distribution becomes uniform already in the short-term phase because of the fact that each fragment has a slightly different energy caused by the break-up. Hence, $J2$ effect on the mean anomaly is not visible. This is the evidence that ensures the validity of Kepler's dynamics assumptions in the short-term phase. This statement will also be demonstrated in the following sections.

3.2 Ejection velocity direction models

As seen in Chapter 2, NASA's standard break-up model provides ejection velocity distribution of fragments only in terms of magnitude, but no ejection direction is specified. A magnitude only distribution is of no real use to debris cloud propagation or collision hazard analysis applications, as it has already been clarified in Section 1.2. Different approaches able to describe the outcome of a break-up in terms of ejection directions exist. The isotropic ejection model is the most commonly used to describe a debris cloud for debris cloud evolution and conjunction risk assessment applications. Its main advantage lies in its simplicity and in the fact that it does not consider a preferred direction of ejection, making it conservative when the break-up physics are not well understood and the potential ejection geometry is unknown. Although it is difficult to determine the ejection pattern, if such information is available, an anisotropic model can be used, which may be more coherent with the fragmentation physics. An overview of both ejection models is provided in the following two subsections.

3.2.1 Isotropic ejection model

The simplest way to model a debris cloud's behaviour is to assume that all fragments are ejected isotropically from the break-up point [11], meaning that a fragment has the same probability to be ejected in every direction. This model is based on the assumption that the fragmentation energy is equally distributed in all directions. Hence, the isotropic model considers that all imparted velocity directions are uniformly distributed over a surface of a sphere, causing the cloud to initially be a sphere. A uniform distribution over a surface of a sphere can be translated as the extraction of two angles, azimuth and elevation, from two distinct uniform distributions. The two angles can be defined in RTN reference frame, as shown in Figure 3.3.

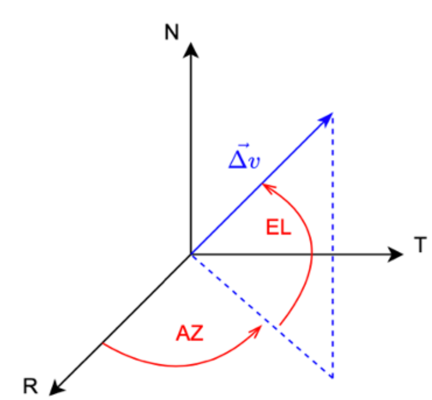

Figure 3.3: Azimuth and elevation angles in RTN reference frame

Uniform distribution means that all azimuths from 0° to 359° and all elevations from -90°

to 90° have the same probability to being extracted. So, each fragment is characterised by a velocity vector of magnitude extracted from the ejection velocity distribution provided by the SBM and of direction given by two angles extracted from two uniform distributions. Following this idea, the final ejection velocity model, including both magnitude and direction, can be seen as a series of concentric spherical shells of iso-probability, as shown in Figure 3.4. Every single shell represents the probability value of a specific ΔV magnitude provided by the SBM probability density function. Any ejection velocity vector of a given norm has the same probability to have every direction, that is why it is a spherical surface of iso-probability.

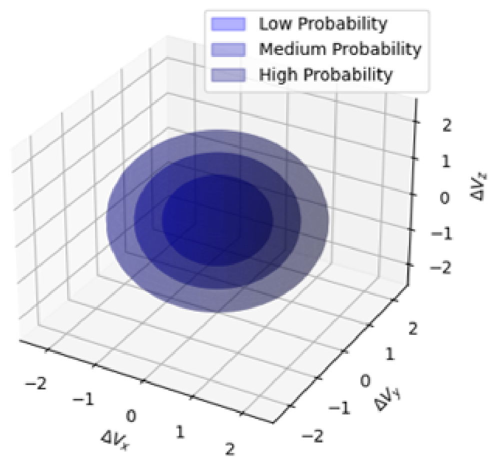

Figure 3.4: Iso-probability curves of ejection velocity

The main advantage of the isotropic model is its simplicity. At the same time, it may not accurately represent the outcome of a fragmentation. By assuming that all fragments are ejected uniformly in all directions, an isotropic cloud model smooths out the effects of regions of high/low fragment density in a specific direction [11]. Hence, an isotropic model can either underestimate or overestimate the number of fragments ejected toward a certain range of directions. However, this approach appears to be very conservative, since no preferential ejection direction is considered, which is very suitable for preliminary risk assessments and general predictions.

3.2.2 Anisotropic ejection model

Although it is very hard to obtain information regarding the preferential directions of ejection, if such information is available, it is possible to adopt a anisotropic model that abandons the assumption that fragments are ejected uniformly. An anisotropic model is able to reflect many realistic scenarios, but it appears to be much more complex, since it considers additional factors, such as the initial velocity vector of the parent, the spacecraft orientation and the dynamics of the explosion or collision. Assuming the knowledge of a given bias of ejection directions, the probability density functions of the two angles can be modified in order to achieve this condition. For example, for a forward bias, a stepped distribution from -45° to 45° of azimuth and elevation may be considered, as shown by Figure 3.5.

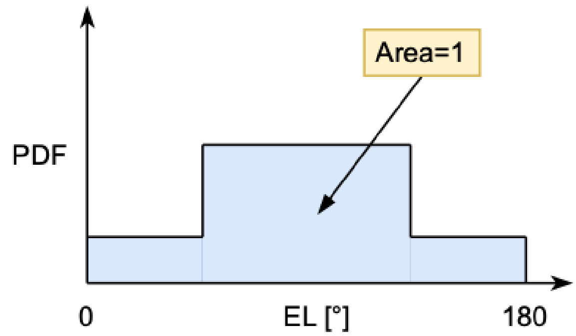

Figure 3.5: Stepped PDF of ejection directions for a forward bias

This is just a numerical example developed following the work proposed by [11]. There can be different types of bias, and depending on break-up characteristics, suitable probability density functions of ejection angles can be employed.

In any case, to delineate a physically coherent scenario, the momentum conservation should be satisfied. This can be done using direction/anti-direction coupling [27], which allows to ensure Equation 3.4, in which n is the total number of fragments and m_i is the i-th mass.

$$\sum_{i=1}^{n} m_i \Delta\vec{V}_i = 0 \tag{3.4}$$

Since the purpose of this section is to follow the dynamics of a debris cloud, an ejection velocity directions model is also required. Because it is the most used model within debris cloud evolution and collision risk assessment tools and because of its simplicity, the isotropic ejection model has been chosen to be used for the analysis of debris cloud evolution.

3.3 Test case

To verify the cloud dynamics evolving in time, a break-up event has been simulated. The approach consists in generating fragments, computing each initial state vector and propagating them individually. An in orbit explosion has been considered for this analysis. The parent is assumed to be a 1000 kg spacecraft with a drag wet surface of 3.2 m^2, and its orbital parameters at break-up time are summarised in Table 3.1.
To simulate the break-up and generate the fragments characteristics database, the C++ implementation of NASA's standard break-up model by [18] has been used.

a [km]	e	i [°]	Ω [°]	ω [°]	M[°]
6880	0.001159	97.44	275.44	142.02	271.59

Table 3.1: Initial orbital parameter of the parent

The reason for choosing an empirical break-up model lies in the fact that the SBM is the most widely used model within debris environment tools and fragmentation outcome determination.

Event type	*Platform type*	*Mass* [kg]	L_c [m]
Explosion	Spacecraft	1000	0.10

Table 3.2: Parent input for the break-up model

The inputs required by the code are the event type (explosion or collision), parent mass and minimum characteristic length, which are summarised in Table 3.2. The explosion feature has been selected and according to the platform type (spacecraft or upper-stage) and mass of the parent, the appropriate scaling factor is automatically selected by the tool. Since the objective of this analysis is to visualise how fragments orbit parameters evolve over time, there is the necessity to propagate them individually, hence the lower bound of characteristic length was set to 10 cm to limit the computational expense and time.

3.4 Initial conditions of the debris cloud just after the break-up

Before truly analysing the evolution of the fragments over time, it is necessary to focus on the initial conditions of the debris cloud immediately after the break-up. The break-up model has generated a total number of fragments of 1200, enforcing mass conservation option provided by the tool. As already stated in Chapter 2, ejection velocities distribution is the most relevant for our purpose. As it can be seen in Figure 3.6, ΔV magnitudes range from few m/s to almost 400 m/s, with some fragments reaching up to 1300 m/s. The red vertical line indicates the average of magnitudes, which is located to about 70 m/s.

The code employs an isotropic distribution for velocity vector directions, meaning the azimuth and elevation of each vector are selected uniformly over a sphere. Figure 3.7 displays the outcome of this model in the parent RTN reference frame. Arrows represent ΔV vectors centered in the break-up point and the spherical dark shell is the mean of the magnitude. In this plot, nadir and parent orbital velocity direction are also represented as black and red arrows, respectively. Imparted velocity vectors are plotted in two different colours: blue arrows indicate fragments subject to de-orbiting, while green vectors are referred to $\Delta\vec{V}s$ that are not causing decay. All ejection velocity vectors causing a decay have a common feature: they are all located on the right side of the graph, meaning that they are characterised by a velocity component opposite to the parent motion. Obviously, an anti-tangential component of imparted velocity causes a reduction of the semi-major axis, which is the main potential reason to induce the fragment to reentry. Since an isotropic ejection model is involved, roughly half of fragments receive from the break-up a $\vec{\Delta V}$ with an anti-tangential component with respect to parent orbital velocity. On top of all, if one thinks to typical values of ΔV required for an altitude change of a LEO spacecraft, which are on order of tens meters per second for a limited variation, it should be intuitive that so high ΔVs in negative direction are likely to cause the decay. The combination of these two factors leads to a high percentage of immediate de-orbiting.

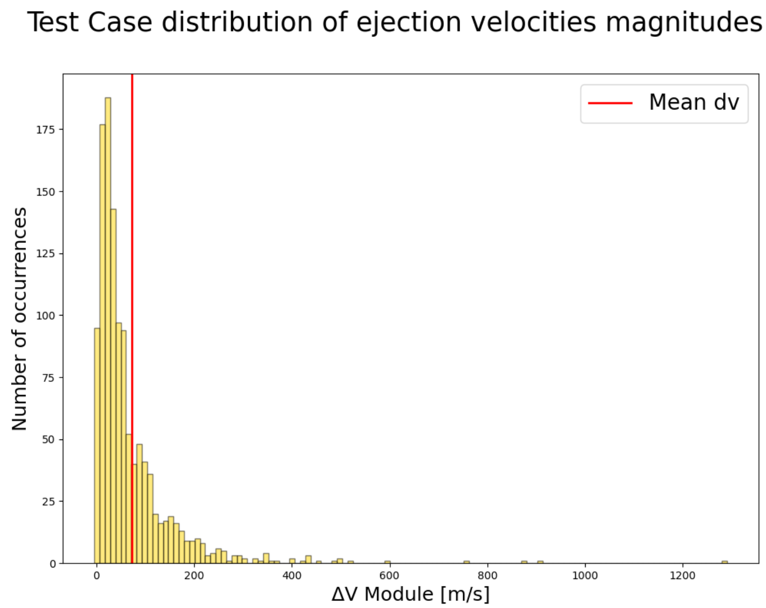

Figure 3.6: Distribution of ejection velocities magnitudes of the test case

The same situation can be analysed through the Gabbard diagram plotted in Figure 3.8. Gabbard diagrams plot perigee and apogee altitudes against semi-major axis altitudes (i.e., orbital period) and are suitable to analyse a scenario with many fragments [28]. The horizontal orange line represents the Earth's atmosphere threshold, set to 180 km. Any fragment below this threshold is considered to have decayed. Red dots represent apogee altitudes of fragments, instead perigee altitudes are seen as blue dots. The "X" shape is due to the fact that the parent orbit is almost circular. Fragments located on the left size of the plot have received net retrograde impulses, instead on the right site they have received posigrade net impulses. It can be noticed the apogee altitudes of retrograde pieces are similar to the perigee altitudes of posigrade pieces. This reflects the fact that an impulse at perigee (apogee) affects only the perigee (apogee) altitude and has no effect on the apogee (perigee) height. For a circular orbit, perigee and apogee are defined once the impulse is applied.

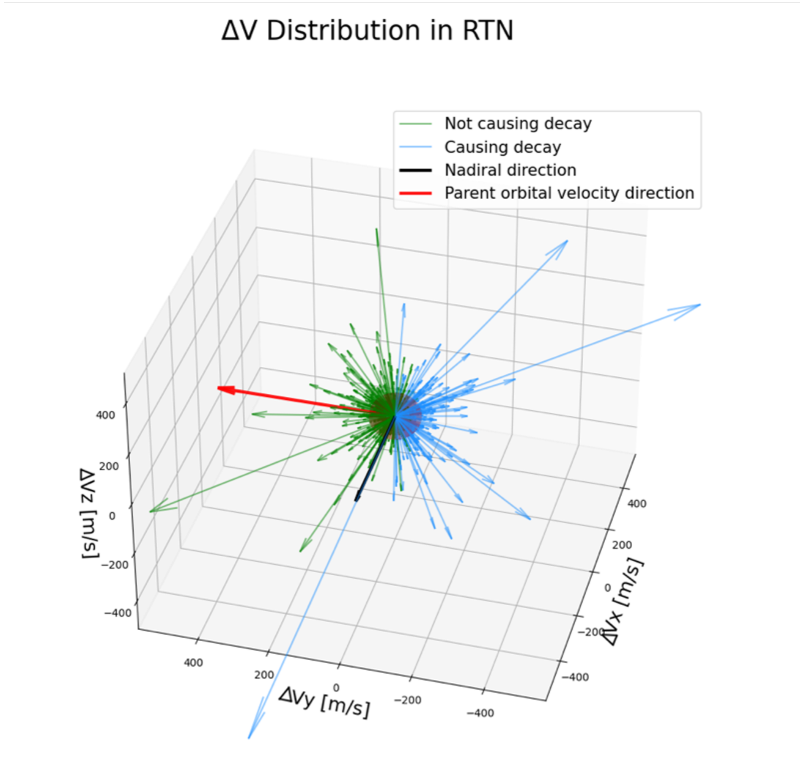

Figure 3.7: Ejection velocity vectors in RTN of the test case

However, most fragments are close to the initial orbital features of the parent, but still, there are some pieces much more dispersed, with very different apogee and perigee heights. From the diagram, it is evident that many fragments have a perigee below the atmospheric threshold immediately after the break-up, meaning that they will practically de-orbit soon. Additionally, a significant number of fragments, while having a perigee above the threshold, are still very close to it, and consequently, we expect them to decay in the future.

Each fragment state vector can be derived through a very simple procedure. Two distinct time instants, identifying the moment just before and after the break-up respectively, are defined as t_0^- and t_0^+. At time t_0^-, no fragment already exists but the parent is located at position $\vec{r}_0$ with orbital velocity $\vec{V}_0$. It can be assumed that the parent has not moved at time t_0^+, so fragments are all generated at the same position $\vec{r}_0$, while because of the break-up they will acquire an additional $\vec{\Delta V}$ to their initial orbital velocity $\vec{V}_0$. Hence, the state vector of the i-th fragments is determined like in Equation 3.5, ensuring that the vectorial sum is performed in the same reference frame.

$$SV_i = [r_0, V_0 + \Delta V_i] \tag{3.5}$$

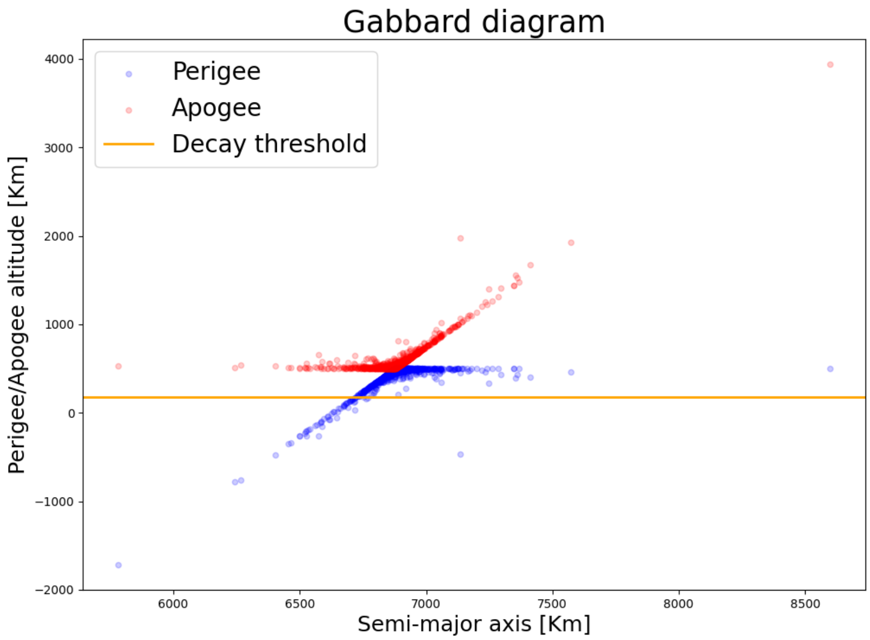

Figure 3.8: Gabbard diagram of the test case at break-up time

Once all debris initial state vectors are known, it is possible to pass to initial Kepler's elements. All initial orbital parameters at time t_0^+ of each fragment are estimated, resulting in slightly different orbits with respect to the original parent trajectory. Since this analysis involves a conspicuous number of fragments, the best way to visualise their orbital parameters is through distributions.

Figure 3.9 shows histograms representing distributions of initial orbit parameters of fragments of the test case at time t_0^+, and orbit parameters of the parent are represented as vertical red lines.

The histogram on the high left corner shows the semi-major axis distribution. It is both reduced and increased with respect to the parent value. Most fragments are quite close to the parent. For both the inclination and right ascension of the ascending node, the average registered variation is less than 1°, but very few pieces are characterised by a heavier change.

Until now, parameters are represented in their absolute definition. The problem for the argument of perigee and the mean anomaly is that they are measured starting from the ascending node and perigee angular position, which are both changed because of the break-up. To visualise their coherent distribution, they must be referred to a constant point, i.e., the parent value.

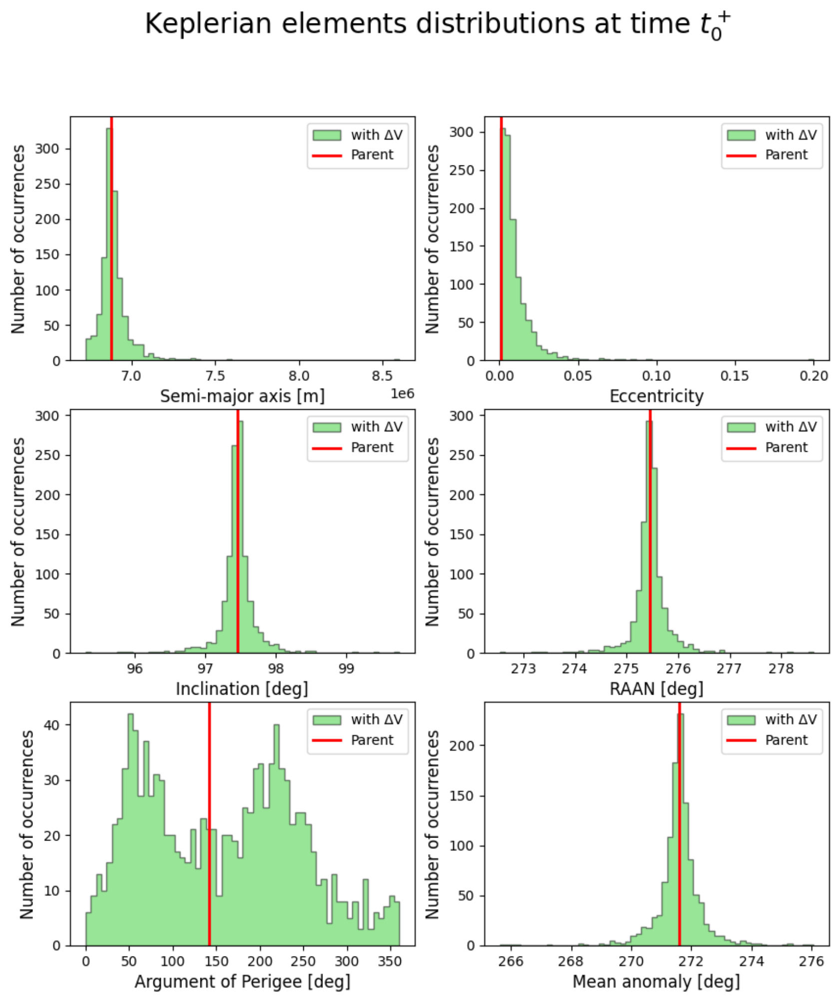

Figure 3.9: Keplerian elements distributions at time t_0^+ of the test case

The transformation can be computed through simple geometric considerations, leading to the following relationships.

$$\omega = (\Omega_i - \Omega_{parent}) + \omega_i \tag{3.6}$$

$$M = (\omega_i - \omega_{parent}) + M_i \tag{3.7}$$

The mean anomaly distribution is shown in the low right corner and most fragments receive a variation of a few degrees (2° maximum), and a small group deviates a bit more, but still in a limited way. It can be noticed that a, i, Ω and M have in common the fact that their distribution is bounded and center in the parent value.

The last statement seems to be invalid for eccentricity and argument of perigee. Indeed, both distributions are not centered on the parent value. In the eccentricity histogram, it can be observed that the number of fragments gradually reduces for higher values of eccentricity. Finally, the argument of perigee distribution is completely different. This parameter disperses all over the orbit, there is no conspicuous group that remains close to the parent value. Instead, two separate peaks are placed on the right and on the left of the red line, and their displacement seems to be of about $\pm 90°$. The reason for this behaviour lies in the fact that the parent initial orbit is almost circular. Both eccentricity and argument of perigee are very sensible parameters to orbital velocity changes. For example, the ΔV magnitude needed to change the angular position of the perigee with a single impulse is expressed by the following relation.

$$\Delta V = 2e \sin \frac{\Delta\omega}{2} \sqrt{\frac{\mu_E}{p}} \tag{3.8}$$

It is evident that lower is the eccentricity, lower is the required additional velocity to move the perigee. Since ΔV norms involved are very high, this explains why the argument of perigee is subjected to such a strong variation.

An even stranger trend regarding the argument of perigee is observed. Not only it is not centered in the parent value, but it is spread along the entire orbit, seeming already random. Consequently, its distribution appears to be wider than the mean anomaly. As stated in Section 3.1, only a bias of ω, Ω and M with respect to the parent is expected in the short term, and the mean anomaly is supposed to be the first distribution to reach the randomization. In reality, this does not seem to be the case. To understand this behaviour, the key point to bear in mind is that the time evolution of parameters has not yet been considered. The histograms in Figure 3.9 show the orbital parameters of the fragments at the initial time t_0^+ right after the break-up, hence only the effect of ejection velocities is present.

However, to correctly visualise the time evolution of orbit parameters of fragments, a change of perspective is necessary. The effect of ejection velocities on the distributions caused by the break-up should be concealed. Therefore, for the sole purpose of properly visualising the phases of the debris cloud evolution, distributions will henceforth be expressed as differences between instantaneous fragment parameters and initial fragment elements at t_0^+.

As a conclusion, in all distributions, except for the argument of perigee and eccentricity, it can be observed that most fragments still have very elements similar to the parent ones, hence, a single peak centered in the parent value is clearly visible. Figure 3.10 shows distribution of orbital parameters differences with respect to the corresponding parent parameter, in which limited bias of a, i, Ω, M distributions are even more visible.

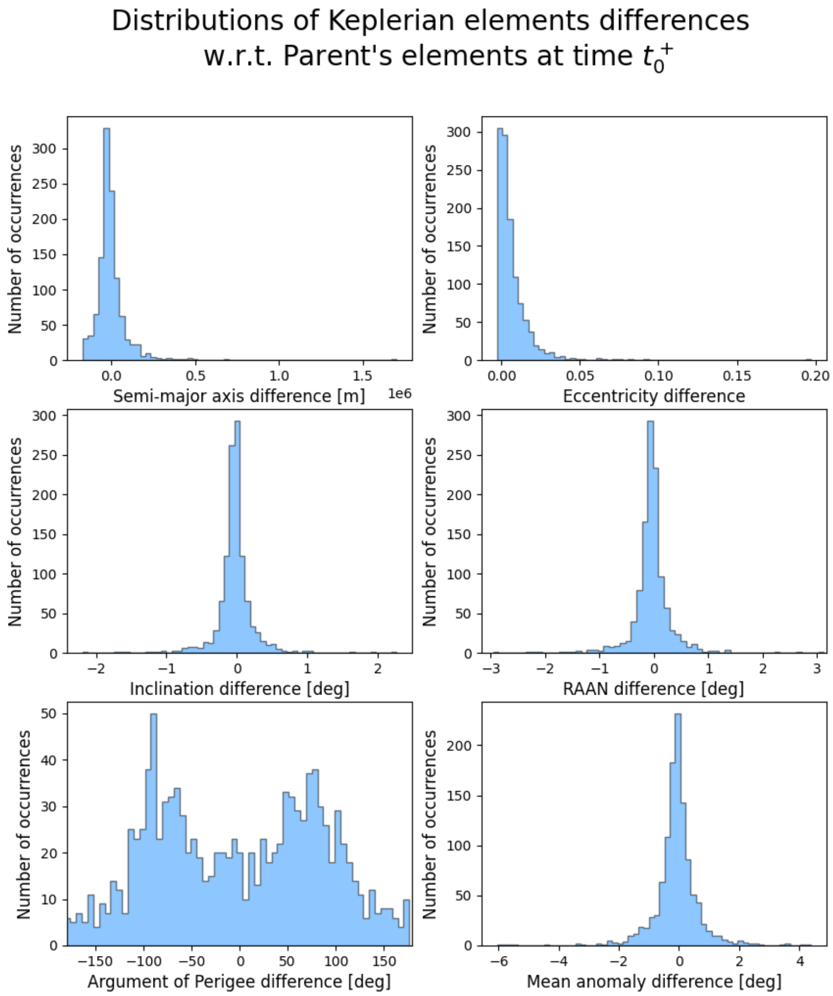

Figure 3.10: Distributions of Keplerian elements difference w.r.t. parent value at time t_0^+ of the test case

.

3.5 Orbits of fragments without perturbations

As already stated in Section 3.1, the cloud evolution in medium and long-term is governed by the Earth's oblateness effect. If no perturbation is considered, once the mean anomaly randomization is reached, the cloud would keep a stationary pinched toroid shape indefinitely over time. State vectors of fragments, computed through Equation 3.5, can be converted into orbital elements, in order to visualise their orbits. In Figure 3.11, all orbits of fragments with a perigee altitude above the 180 km threshold are plotted and analysed from two perspectives: from an external observer and from the pinch point. This would be the stationary ensemble of orbits in Kepler's motion assumptions.

The red cross in the plot represents two characteristic points, the break-up point and the pinch point, while the blue line indicates the pinch line. This is a result of the fact that each fragment receives its $\Delta\vec{V}$ at the same point, which is the break-up point $\vec{r}_0$, so they must pass again through it, but not necessarily at the same time, since each orbit will have a different orbital period. If all fragments passed for the pinch point at the same time, this would be an infinity cloud density point, since the cloud volume would collapse to zero. Even if in reality the volume will never be zero, the density would still be very high, representing a critical condition for collision risk assessment for operational spacecraft that are close to the pinch point location.

Furthermore, as already mentioned in Section 3.1, pinch points are not the only high density regions, but a pinch line exists and is located 180° from the pinch point in the parent orbit plane. All debris must pass through the orbit plane along this line and as evidence of this, removing the Earth for graphical reasons and looking to the same previous graph from the anti-pinch point (located 180° from the pinch point), a pinch line can be recognised, since all orbits pass through it.

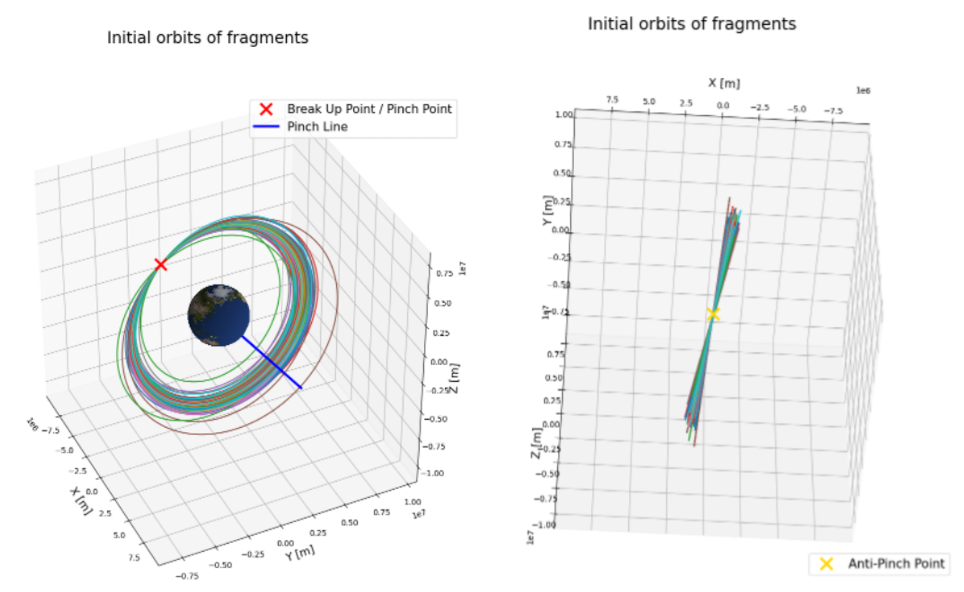

(a) (b)

Figure 3.11: Fragments initial orbits forming a pinched toroid: (a) pinched torus, (b) pinch line

3.6 Debris cloud evolution over three months

Once each fragment is associated with a state vector, their individual propagation can be performed. It is worth noting that the aim of this chapter is to identify the assumptions and conditions that occur during the short-term phase, as the collision probability must be estimated within this time window. In particular, the following section presents the evolution of a debris cloud from its generation to the toroid formation phase through the numerical propagation of individual fragments. Hence, the analysis aims at following the debris cloud evolution during the short term until the cloud shape switches to a closed toroid and the medium term starts.

To observe the short term dynamics, only a few days of simulation are needed. For the specific test case, it has been chosen to follow the debris cloud every hour for 3 days, since the early dynamics is sufficiently fast. Since the mean anomaly randomization is due only to the ensemble of different orbital periods imposed by the fragmentation event itself as stated by [24], no perturbation is considered. For demonstration purposes only, the cloud behaviour continues to be observed every 15 days after the toroid formation, up to 3 months. The chosen time interval is coherent with the slower dynamics that characterises this phase. Kepler's motion assumptions are not acceptable anymore, since the Earth's oblateness effect governs the band formation. Hence, only the J_2 perturbation is included in the propagation, while the atmospheric drag is neglected, according to what is stated about the relative importance of perturbations in Section 3.1

A filtering process, in which all fragments with an initial perigee altitude below a threshold of 180 km are removed, precedes the actual propagation. No further filtering is needed, since only the Earth's oblateness effect is considered during the second time span, which has secular effects only on variation of Ω, ω and M elements. Hence, an average change of the semi-major axis is not expected, meaning no further decays are predicted, but short and long period oscillations in a, e and i elements may still be visible.

3.6.1 Short-term analysis

Firstly, the analysis of debris cloud evolution in the short-term phase is presented. According to the theory of phases of evolution, the expectations are to observe that the M distribution gradually extends its bounds over time until it is dispersed along the entire orbit, while all other distributions should appear only with a bounded bias with respect to the parent and remain unchanged, since no perturbation is considered. To demonstrate the randomization of the mean anomaly, fragments are propagated for two days through an analytical propagator. The figures provided represent the distributions at 1, 12, 36, and 48 hours after the break-up. Furthermore, it is noted that, in order to conceal the effect of the initial ΔV, the distributions are expressed in terms of differences relative to the values of the orbital parameters at time t_0^+, as clarified in Section 3.4.

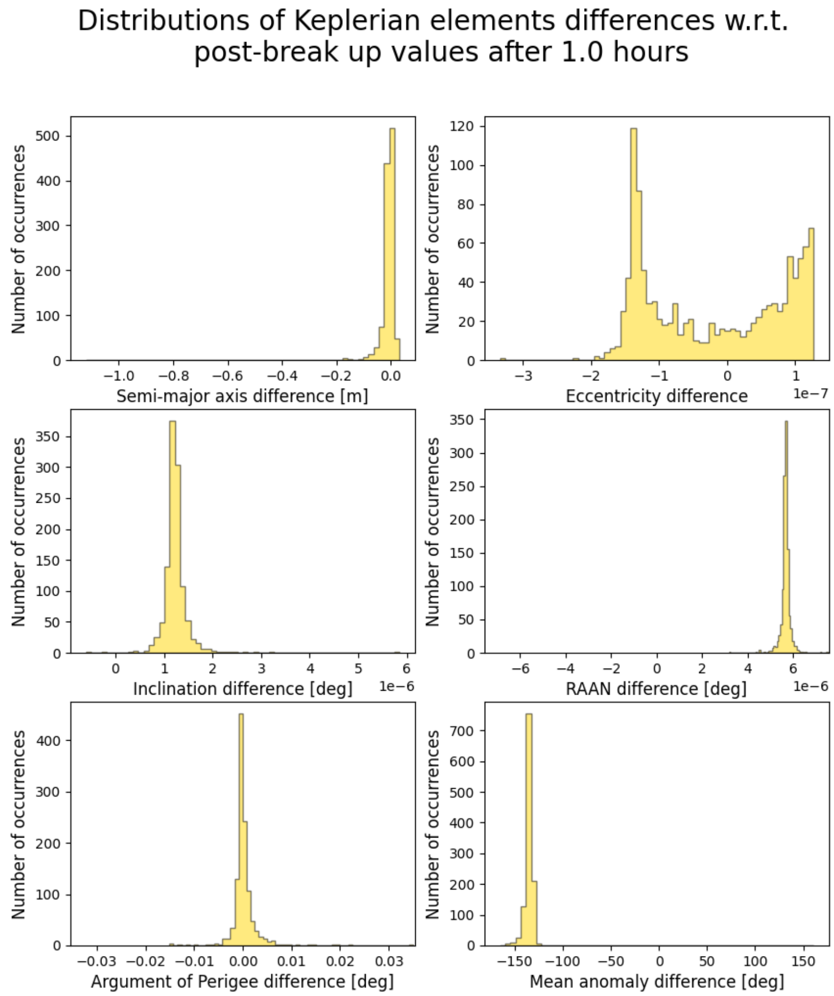

Figure 3.12: Keplerian elements differences distributions w.r.t post break-up elements after 1 hour

It is possible to observe how, as expected, the mean anomaly distribution tends to become wider over time and moving away from the parent mean anomaly at the same time instant. Initially, just one hour after the event, the distribution spans less than 50°, but it extends to cover 360° within 12 hours. This does not mean that the mean anomaly has already become random after 12 hours, because the distribution is far from random and still shows a peak centered in the parent position. In the meantime, a, e, i, Ω and ω distributions remain unchanged during this time span, showing only a bias with respect to the parent value, as already predicted. It is important to note that the scales are very small, so the extent of these distributions is practically close to zero. A careful observer might notice that the distributions are not actually constant over time. These slight variations are due to approximation errors in subsequent state vector to Kepler elements conversions.

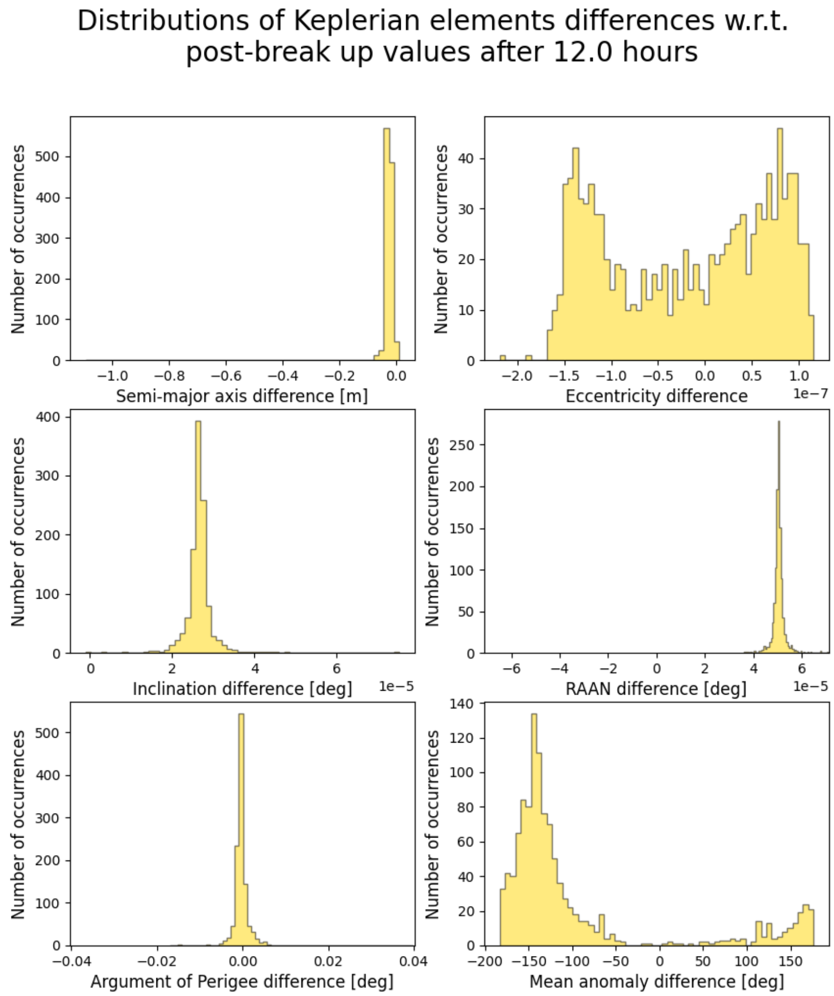

Figure 3.13: Keplerian elements differences distributions w.r.t post break-up elements after 12 hours

Thanks to the appropriate representation, also the argument of perigee distribution appears to be always narrow with respect to the mean anomaly. Instead, the latter is the only distribution that is changing, and it is actually expanding along the orbit, tending to reach a uniform distribution when the randomization is completed. Since there are different orbital periods induced by the break-up, M is the only parameter that is changing, instead the others are related only to the ejection velocities effect. In this particular case, it can be seen that after 2 days of propagation, the M distribution is still not completely uniform, but in relative terms, it is much more random with respect to distributions at previous time instants.

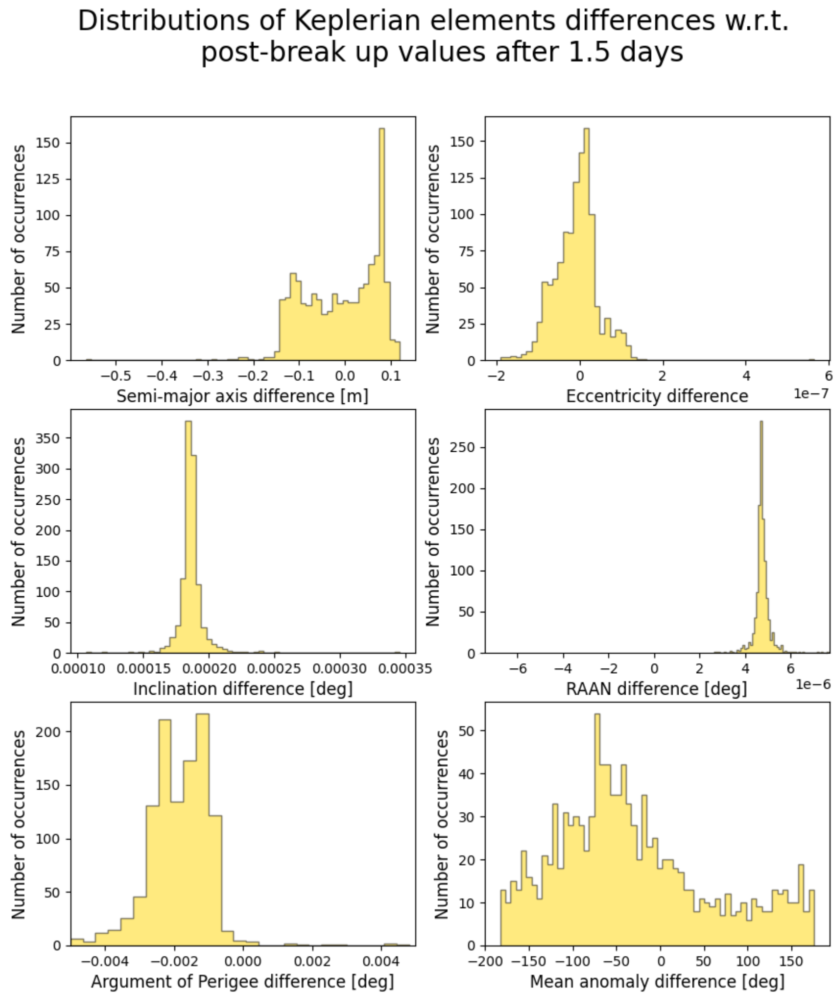

Figure 3.14: Keplerian elements differences distributions w.r.t post break-up elements after 36 hours

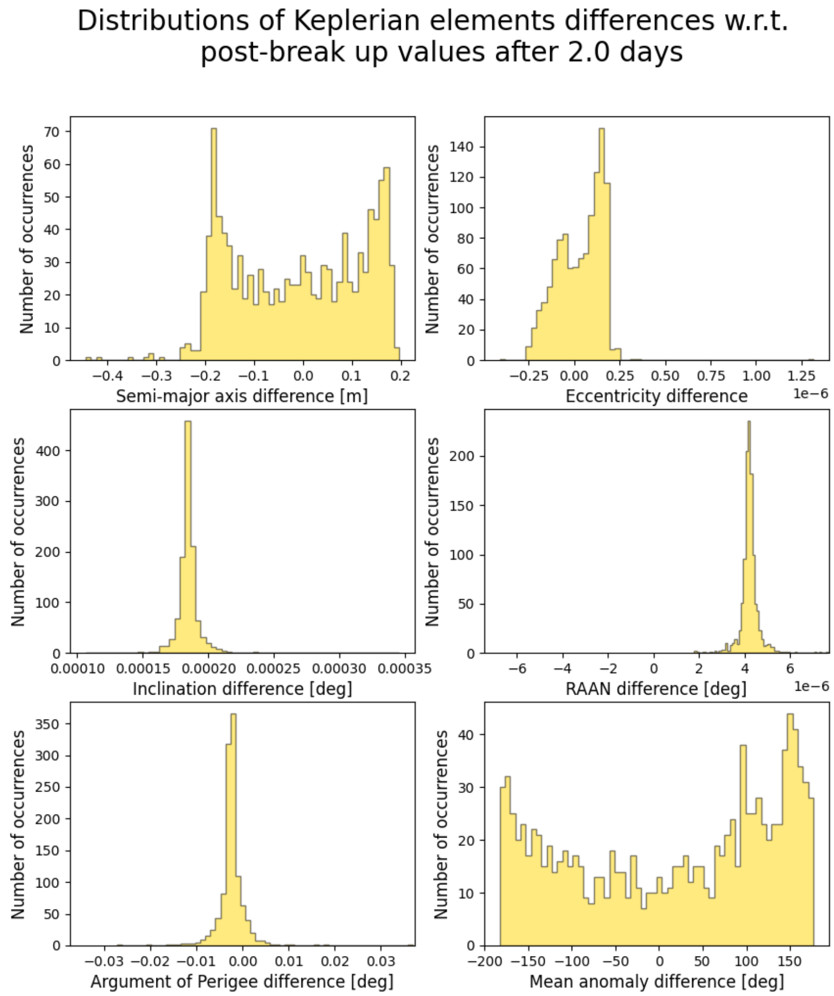

Figure 3.15: Keplerian elements differences distributions w.r.t post break-up elements after 48 hours

It is possible to analyse the dynamics of the cloud shape during the propagation, displayed by Figure 3.16. After 1 hour, the debris cloud appears to be very tiny and practically located in proximity of the parent. This condition reminds of the shape of the first evolution phase presented in Section 3.1, i.e., the ellipsoid. Increasing the time, the cloud starts to spread along the orbit and after 12 hours it has already covered more than half orbit. The shape is moving towards the torus, which signs the end of the short-term phase, but is not closed yet. Furthermore, it can be seen that the debris density is much higher as it is closer to the parent position. Instead, after 36 hours the torus seems to be closed, indicating the achievement of the mean anomaly randomization.

However, Figure 3.14 and 3.15 suggest that the mean anomaly randomization is not attained either after 36 or 48 hours, as the distribution is still clearly not uniform in both cases. In Section 3.8, the time required to reach the randomization is computed following a classical and alternative approach.

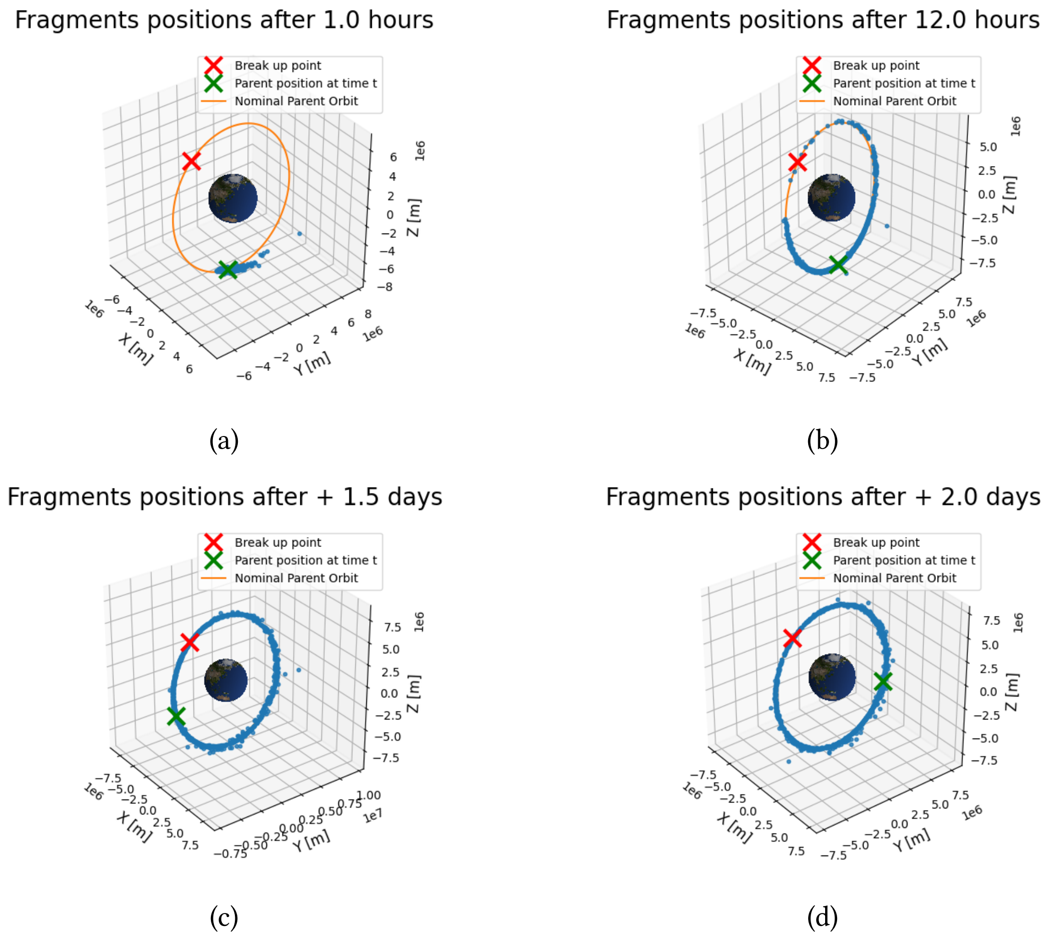

Figure 3.16: Short-term debris cloud evolution after: (a) 1 hour, (b) 12 hours, (c) 36 hours, (d) 48 hours

3.6.2 Short-term analysis under the Earth's oblateness effect

As stated in Section 3.1, the only driving force governing the short-term phase is the $\Delta\vec{V}$ effect caused by the break-up, which leads to the mean anomaly randomization. The objective of this section is to demonstrate that the $J2$ perturbation, which rules the subsequent phase, has no effect in the short-term, as stated in the literature. To achieve this goal, the fragments are propagated again over the same time span, but this time using a numerical propagator that takes into account the Earth's oblateness perturbation. The following figures represent respectively Keplerian elements distributions after 1, 12, 36 and 48 hours from the break-up.

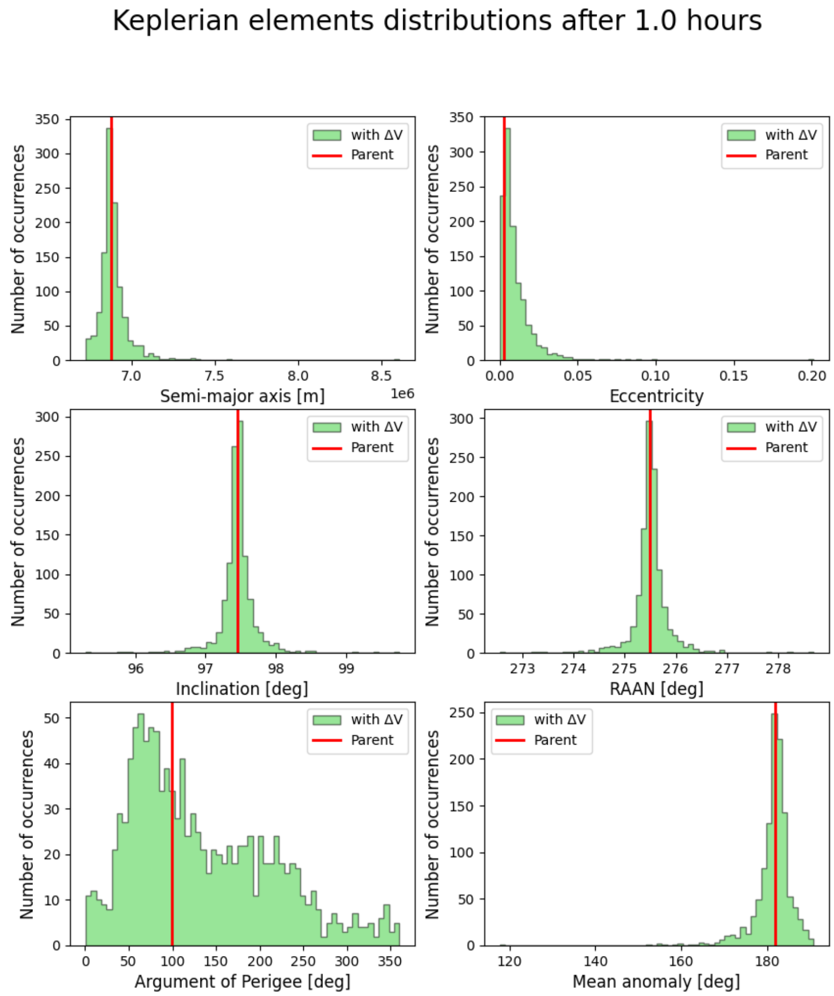

Figure 3.17: Keplerian elements distributions with $J2$ effect after 1 hour

Only for graphical reasons, distributions are not expressed anymore in terms of differences with respect to post break-up values, but their absolute representation is reported. First of all, a, i, Ω distributions are very bounded in every time of observation, while for ω and e distributions, all the considerations made in 3.4 are valid. The mean anomaly shows the same trend as in the case in absence of perturbations, starting from a very narrow distribution, which increases its width over time. The key point to observe is that a, i, e, Ω and ω distributions practically remain constant over time. As a consequence, the mean anomaly is the only orbital parameter that changes over time in the presence of $J2$, just as it does in the absence of perturbations.

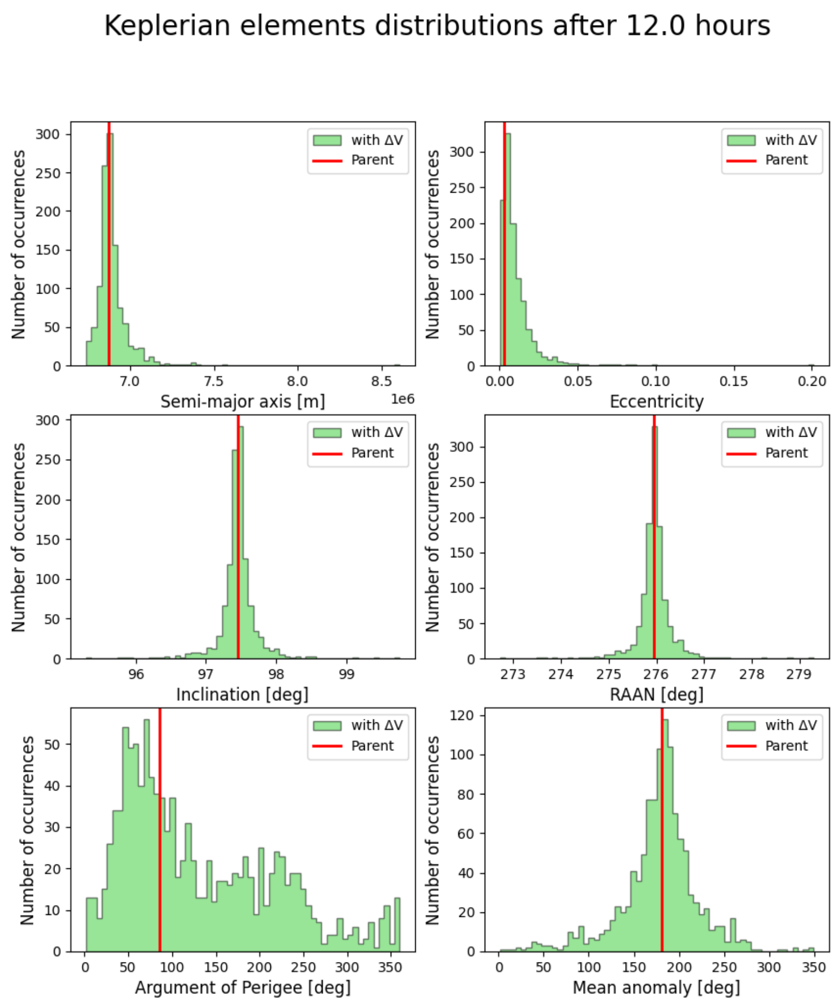

Figure 3.18: Keplerian elements distributions with $J2$ effect after 12 hours

This condition corresponds to motion under the assumptions of Keplerian dynamics, where the orbit itself remains constant and the only changing element is the object position, specifically represented by the true anomaly. Consequently, this reasoning leads to the conclusion that Keplerian dynamics assumptions are valid in the short-term phase. Since the objective of this thesis is to develop a tool for calculating the debris cloud probability of collision in the short-term phase, the assumption of no orbit perturbations can be applied in the development of this tool. This result is not surprising, as the short-term phase has a brief duration, and during such short periods, a Keplerian orbit is only weakly affected by orbit perturbations like $J2$.

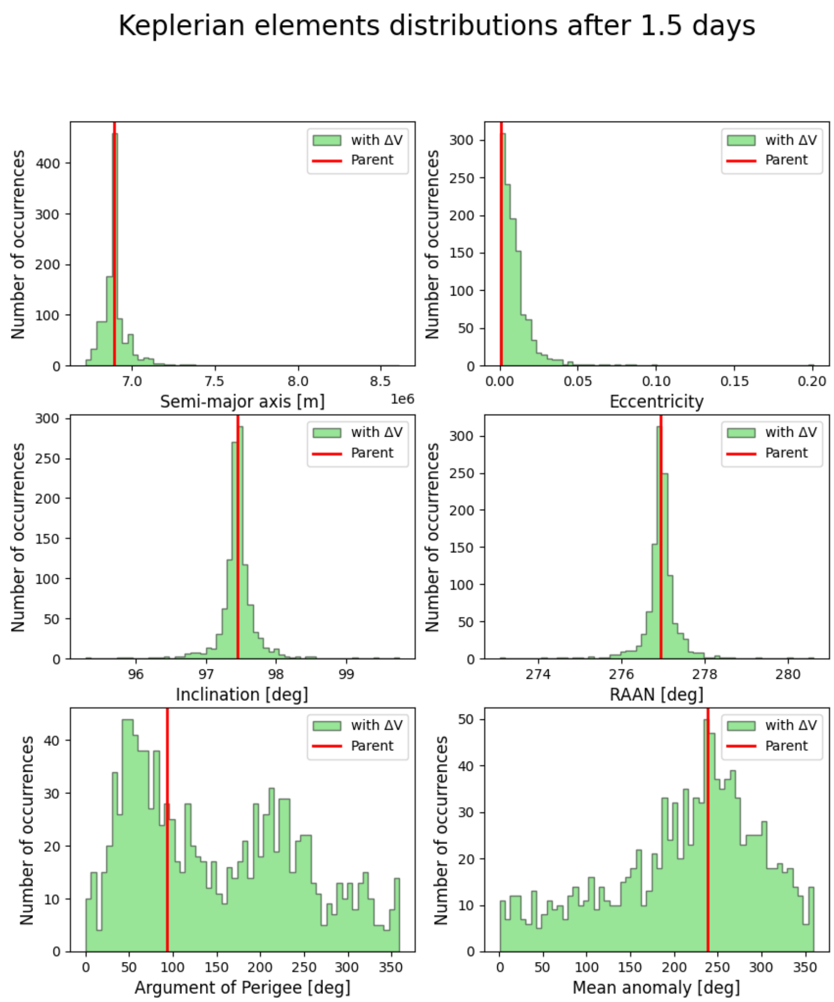

Figure 3.19: Keplerian elements distributions with $J2$ effect after 36 hours

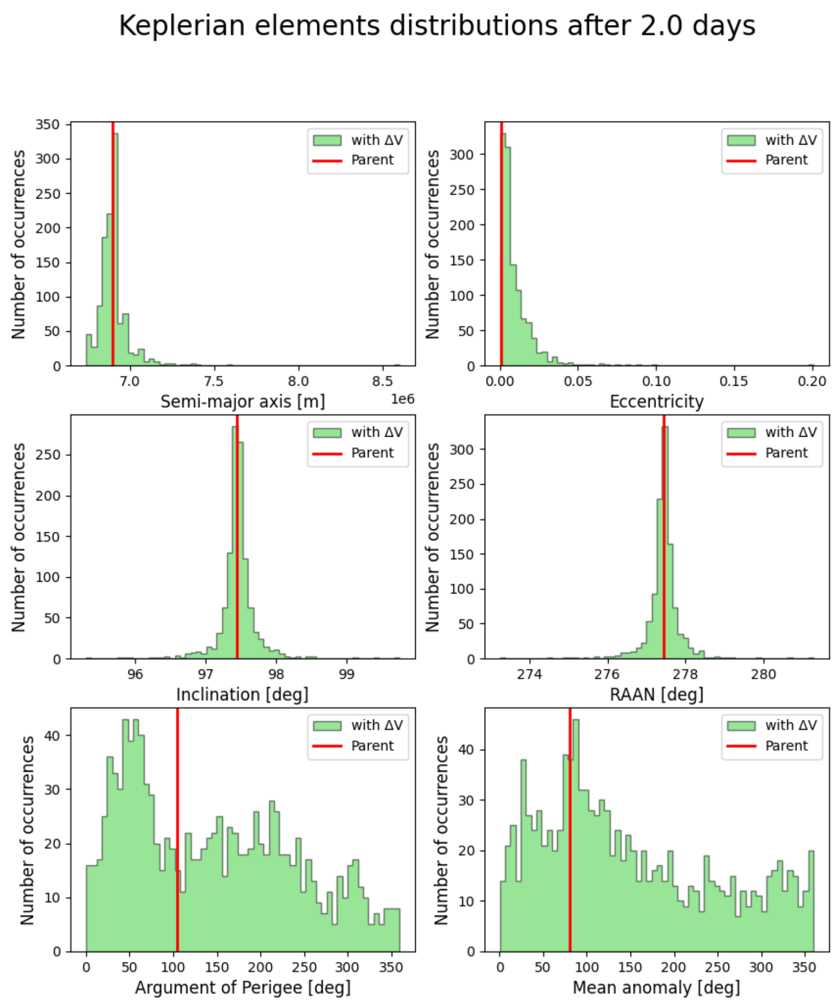

Figure 3.20: Keplerian elements distributions with $J2$ effect after 48 hours

Indeed, in the General Perturbation Method for describing the motion of a space object in the presence of perturbations, osculating orbits, i.e., instantaneous Keplerian orbits that closely approximate the behaviour of the perturbed orbit, are utilised. The method involves solving a second-order differential equation for $\delta\vec{r}$, which represents the difference between the perturbed and Keplerian solutions. The method is based on the fact that a perturbed orbit can be approximated to a keplerian trajectory if $\delta\vec{r}$ is sufficiently small. If $\delta\vec{r}$ becomes too large, the Keplerian solution no longer accurately represents the perturbed orbit, necessitating periodic re-initialisation of the osculating orbit (rectification process). This re-initialisation is required when the perturbations have a significant effect over longer time periods.

3.6.3 Medium-term analysis

In this section, for demonstration purposes only, the analysis of the medium-term debris cloud evolution is presented, even though it is not essential for calculating the debris cloud probability of collision in the short-term phase.

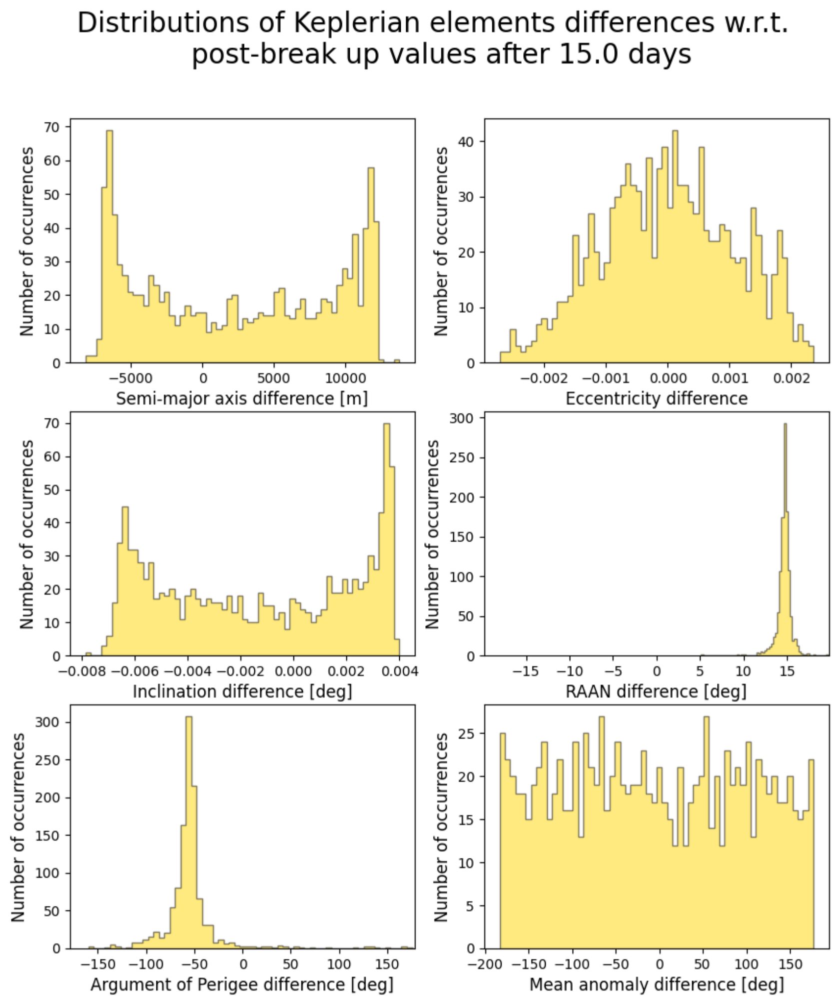

Figure 3.21: Keplerian elements differences distributions w.r.t. post break-up elements after 15 days

According to the theory of phases of evolution, the expectation is to observe the mean anomaly M distributed across the entire orbit (indicating that randomization has already occurred), resulting in a uniform distribution that remains quite stable over time. In contrast, the distributions of ω and Ω should gradually disperse along the orbit due to $J2$, with Ω dispersing at a slower rate than ω, as indicated in Equation 3.2 and 3.1. Conversely, the distributions of a, e and i should remain practically unchanged on average.

Figure 3.21, 3.22, 3.23 and 3.24 represent orbital elements distributions expressed in terms of differences with respect to post break-up values after 15, 45, 60 and 90 days from the fragmentation event. First of all, the mean anomaly distribution is finally a uniform distribution, which is not changing over time on average, and no trace of the parent value is visible anymore. However, it is still possible to see some slight changes in its distribution because the Earth's oblateness also has an effect on this parameter. In the meantime, the argument of perigee and the right ascension of the ascending node are becoming wider, increasing the propagation time.

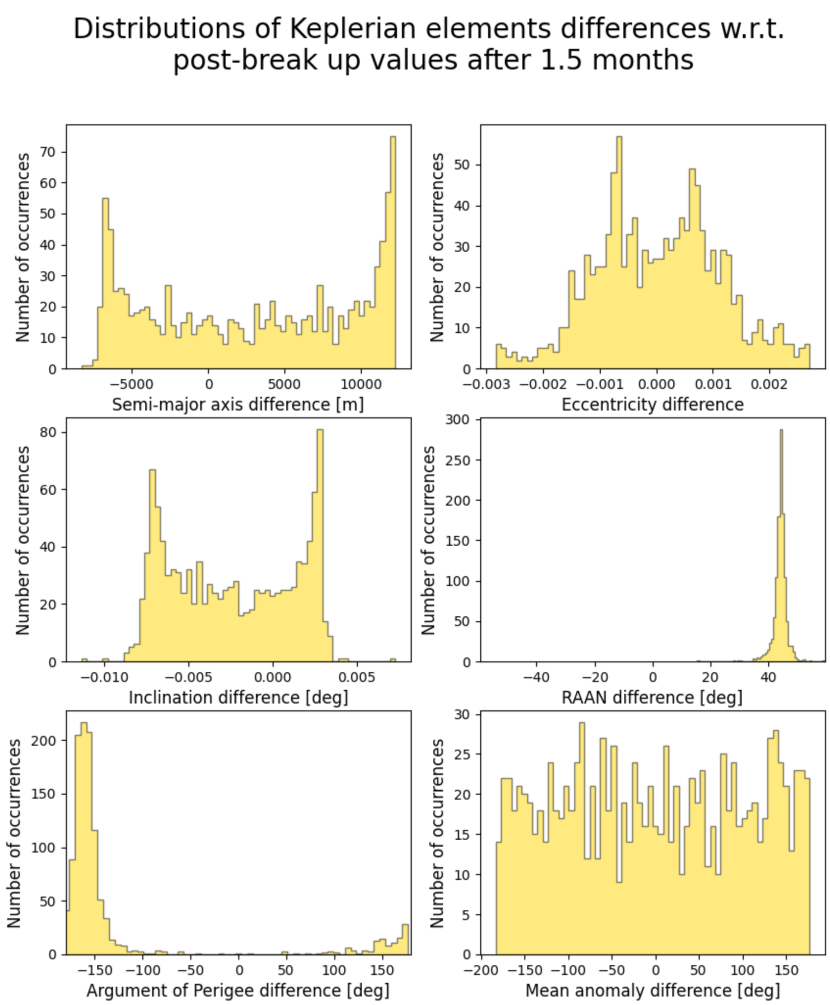

Figure 3.22: Keplerian elements differences distributions w.r.t. post break-up elements after 45 days

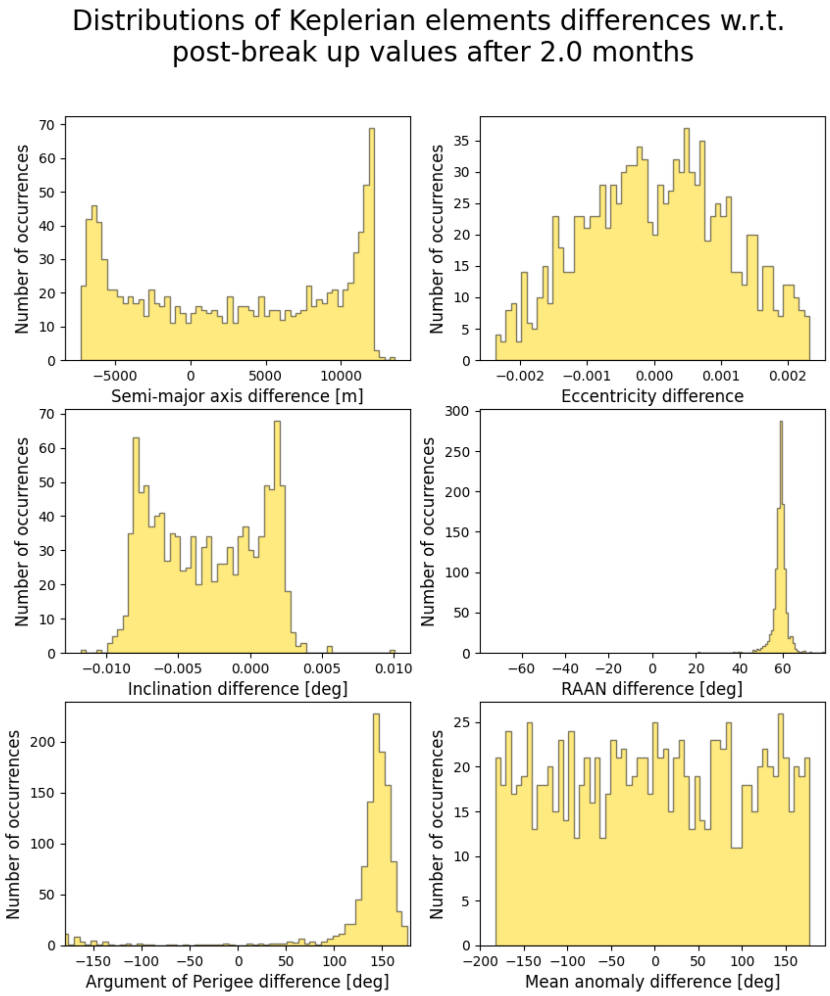

Figure 3.23: Keplerian elements differences distributions w.r.t. post break-up elements after 60 days

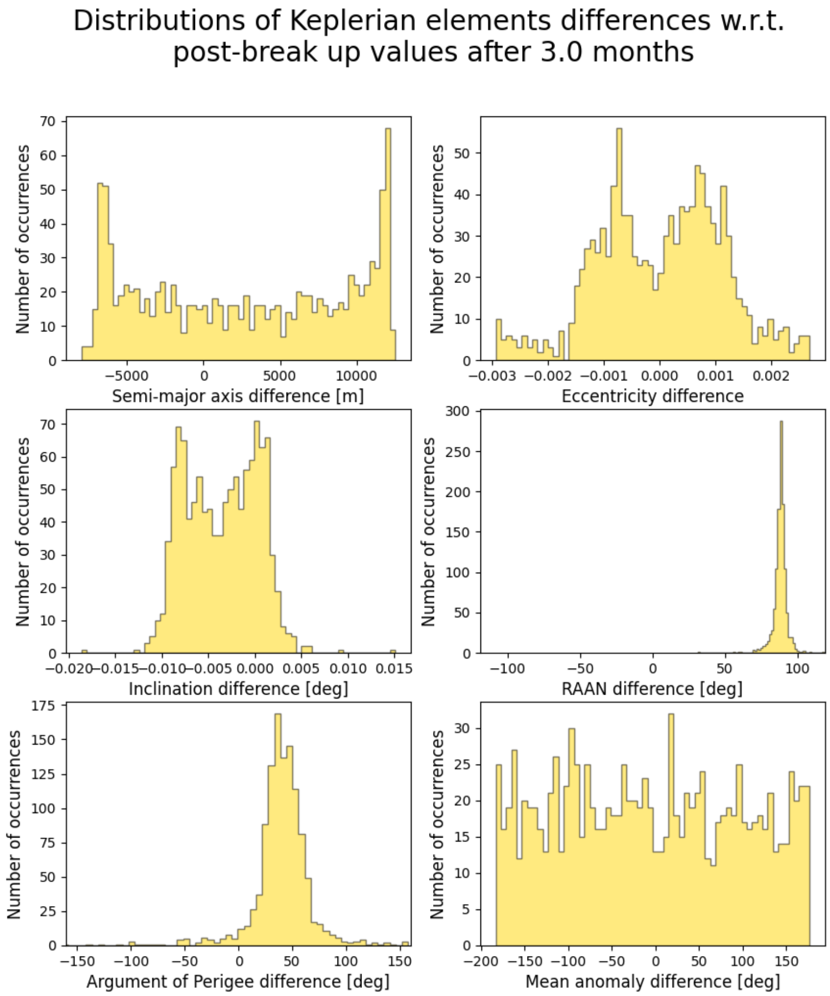

Figure 3.24: Keplerian elements differences distributions w.r.t. post break-up elements after 90 days

For ω, this feature is supported by the fact that the peak of number of fragments is decreasing over time, passing from a maximum of almost 300 to 175 fragments. Instead, regarding the Ω distribution, its dispersion is clear observing the increase of its bounds. In fact, the range of its distribution is increasing over time, passing from [10°, 20°] to [50°, 125°].

As expected from Equation 3.2 and 3.1, the variation rate of the argument of perigee is higher than the one of the right ascension of the ascending node, meaning the the randomization of the first parameter occurs earlier in time. However, three months of propagation are not enough to register a full randomization of Ω and ω, which was expected since the band formation might take several years.

This is supported by Figure 3.25, representing the cloud shape over time. In fact, the cloud shape is closer to a toroid than a band in every time instant. However, the toroid seems to become wider and wider, suggesting that the band formation is in progress. In the same plots, it can be observed that the debris cloud no longer intersects the break-up point but instead appears to rotate around the vertical axis. This behaviour is attributed to $J2$ perturbation, which induces a prograde precession of the lines of nodes for retrograde orbits. This effect arises because the initial parent orbit has an inclination greater than 90°, and since a significant ΔV is needed to alter this parameter, all fragments ultimately end up on retrograde orbits. Hence, lines of nodes are rotating counterclockwise.

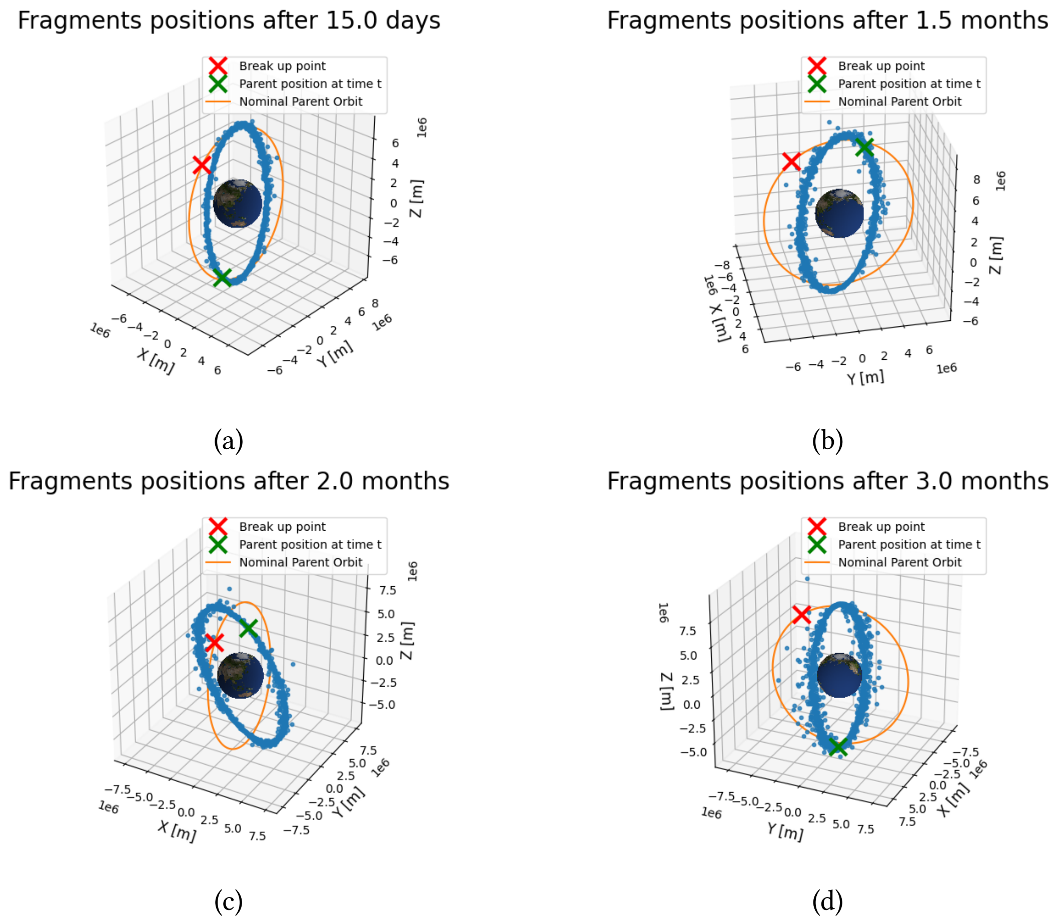

Figure 3.25: Medium-term debris cloud evolution after: (a) 15 days, (b) 45 days, (c) 60 days, (d) 90 days

As stated at the beginning of this section, J_2 perturbation has no secular effect on the semi-major axis, eccentricity and inclination, meaning that on average no variation is expected. But despite this, in Figure 3.21, 3.22, 3.23 and 3.24, a, e and i these distributions slightly change in time and, above all, fragment values move away from the corresponding initial orbital element.

It could seem to be not coherent with what has just been stated, but the reason lies in the fact that J_2 perturbation affects these parameters with short and long periodic oscillations. To demonstrate these effects, the parent object has been propagated for the same time window (3 months) and Figure 3.26 shows how its semi-major axis changes in time with respect to its initial value. As it can be seen, the semi-major axis is not constant over time, but a short periodic oscillation is clearly visible. Furthermore, its mean is not constant and located in zero, but seems to decrease. This is instead due to the long periodic oscillations. The same considerations are also true for e and i.

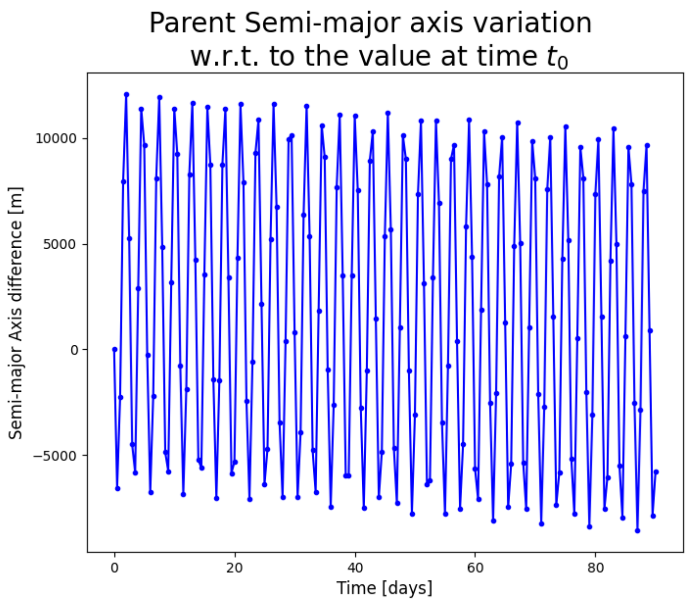

Figure 3.26: Variation of the parent semi-major axis with respect to its initial value

3.7 Analysis on decayed fragments

The main effect on the debris cloud evolution of the Earth's atmospheric drag is to cause the reentry of a given number of fragments, decreasing the cloud density and, as a consequence, also the probability of collision. This perturbation is neglected both in the short and medium-terms, since the first one is governed by the variety of orbital period and the second by the Earth's oblateness perturbation. This does not mean that the drag does not affect the cloud, but its relative importance is low, hence it can be neglected. The same is not true during the long-term, in which argument of perigee, right ascension of the ascending node and mean anomaly have reached the randomization. Hence, the J_2 perturbation no longer affects the already uniform distributions, and the atmospheric drag becomes the most relevant perturbation.

However, the atmospheric drag is a perturbation anything but constant, instead it is strongly dependent on the orbital altitude. As a consequence, its relative importance with respect to other perturbations depends on the parent initial orbit, but also on the break-up outcome. In fact, the atmospheric drag is proportional to the ballistic coefficient, i.e., to the area-to-mass ratio, of which each debris has one. It is worth to underline that this perturbation has effects mainly on the eccentricity, circularising the orbits, and on the semi-major axis. A combination of low altitude break-up, high anti-tangential ejection velocity components, which causes the semi-major axis to decrease, and a large ballistic coefficient may have as a result an early decay of some fragments.

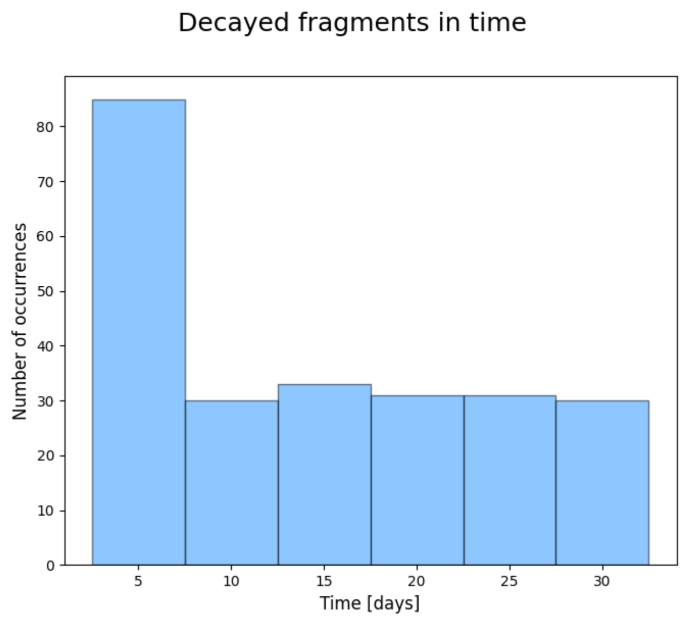

Figure 3.27: Histogram of the number of decays in 1 month

For the specific test case, 60 out of 1200 generated fragments are subjected to an instantaneous decay, meaning that their orbits deriving from the break-up are characterised by a too low perigee altitude, making them unfeasible. This means that 5% of the total decays immediately, which is a quite high rate. As it should be intuitive, the reason for that is a combination of a very high ballistic coefficient and a very large anti-tangential component of the ejection velocity. Once again, the ejection velocity model has a strong effect.

An analysis on the number of decays within one 1 month has been carried out, through individual propagation with a time step of 5 days. From Figure 3.27, it can be seen that a much greater number of decays occurs within 5 days after the fragmentation, while it remains practically constant among the other bins of time. The reason for this behaviour is that the 5-day bin includes not only fragments that decay due to drag but also those that experience instantaneous decay because of great ΔV norms. After 1 month, almost 20% of fragments have decayed. However, the decay rate seems to be higher than expected. The reason for this very high decay rate has already been clarified in Section 3.4, in particular by Figure 3.7. In this specific case, the isotropic ejection model plays the fundamental role of assign great ejection velocity norms to the right (negative tangential component) and left side (positive tangential component) of the motion axis with the same probability, neglecting the impact geometry. This leads to the fact that many fragments experience a significant reduction in their semi-major axis, leading to orbital decay.

3.8 Estimation of short-term phase duration

This section is proposed to provide an estimation of the time required to reach the mean anomaly randomization, which ends the short-term phase of a debris cloud evolution. This has a fundamental importance when a proper method for collision risk assessment must be chosen according to the desired time of analysis, since some methods may be more suitable for medium and long-term than short-term and vice versa. In this specific case, the estimation of the short-term phase duration translates into the determination of the time validity of the debris cloud probability of collision tool.

3.8.1 Classical approach

The simplest approach to compute the time to the toroid formation is to consider the time that the fastest moving fragment takes to catch the center of mass of the cloud in true anomaly [29]. It is assumed that the center of mass of the cloud has the same orbit of the parent. Orbits of fragments, which have received retrograde velocity impulses, i.e., with an anti-tangential velocity component, result in lower altitude orbits, meaning that they will complete more revolutions over time than higher altitude fragments. Following this approach, the time to the torus formation expressed in seconds can be computed through the following equation.

$$T_T = \frac{360^\circ}{(n_F - n_P)} \tag{3.9}$$

The parameter n_F represents the mean motion of the fastest fragment, which is dependent on the minimum semi-major axis, while n_P is the mean motion of the parent, and they both are angular velocities. Since the mean motion is typically measured in [rad/s], a proper conversion to [°/s] must be performed. It should be obvious that this method is affected by the ejection velocity model, since it influences the minimum semi-major axis, and by the parent initial orbit (only its semi-major axis).

Injecting parent and fragments orbit parameters of the test case presented in Section 3.3, the time to the toroid formation is only of about 3 hours and 10 minutes. This value is not actually confirmed by the previously performed propagation. Indeed, Figure 3.16 shows that after 12 hours the toroid has just covered only half of the orbit, and the corresponding mean anomaly distribution, which can be seen in Figure 3.13, is anything but uniform. Hence, the time to toroid formation computed through Equation 3.9 is much more underestimated with respect to reality. This could have been predicted, since only the fragment with the lowest altitude was considered and not the entire ensemble of debris. Once again, the velocity model has the most impacting effect, since it determines the semi-major axis of all fragments, including the minimum value. However, this approach is exclusively intended to perform a very preliminary estimation, avoiding the actual propagation.

3.8.2 Alternative approach

In order to have a more accurate estimation, one should work directly on the mean anomaly distribution. A possible idea could be to apply the Kolmogorov-Smirnov test, which compares the empirical cumulative distribution function and a reference cumulative distribution function. In this specific case, the mean anomaly distribution at each time instant would be compared to a uniform distribution, until a sufficiently low Kolmogorov-Smirnov distance D_n is registered [25]. An alternative way is to apply a chi-squared goodness of fit test that determines whether the distribution is uniform [26].

Since the propagation of fragments is required in order to work directly on mean anomaly distributions over time, an alternative and simplified method is now provided. The mean anomaly distribution can be represented as a histogram, which means associating each fragment to a mean anomaly bin, covering the entire orbit (360°). When the randomization is reached, it is expected to be almost the same number of fragments per each bin. The check can be performed by comparing the standard deviation of the number of fragments in each bin of the mean anomaly distribution over time with a reference value. The latter should represent the randomization condition, hence, it can be chosen equal to a value sufficiently ahead in time, making sure that the mean anomaly has become random. When the standard deviation of the number of fragments in each bin has decreased up to the randomization value, then the short-term phase can be considered concluded.

For the specific test case, it has been noted that, during the medium-term propagation, the standard deviation of interest is quite fixed to a value oscillating around 4. The following figure shows the standard deviation evolution, which presents a decreasing and asymptotic behaviour down to the reference value. It can be noticed from this graph, that after almost 90 hours the standard deviation appears to be practically constant and fixed around the reference value, suggesting that the randomization has been concluded and the toroid has been formed.

Figure 3.29 and Figure 3.30 show the mean anomaly distribution and the cloud shape after 90 hours from the break-up event, respectively. It can be seen that the distribution is practically uniform, since the parent trace has been almost lost, and the toroid has been closed.

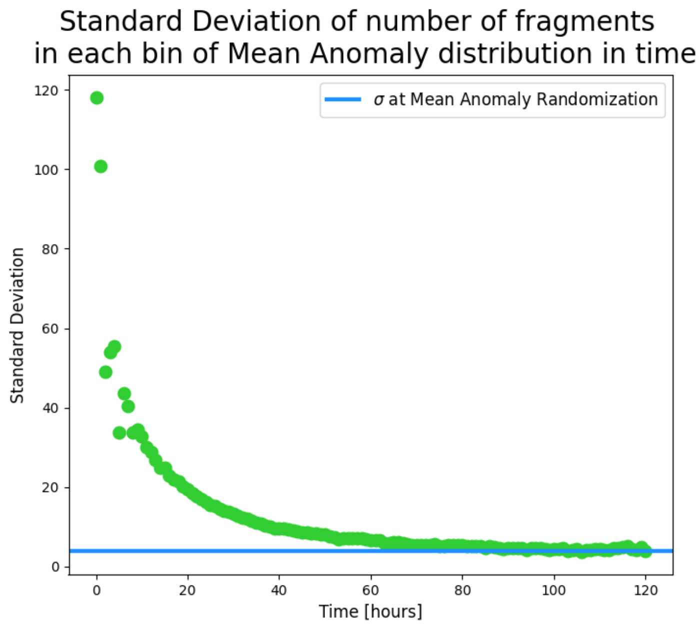

Figure 3.28: Standard deviation of number of fragments in each bin of mean anomaly distribution over time

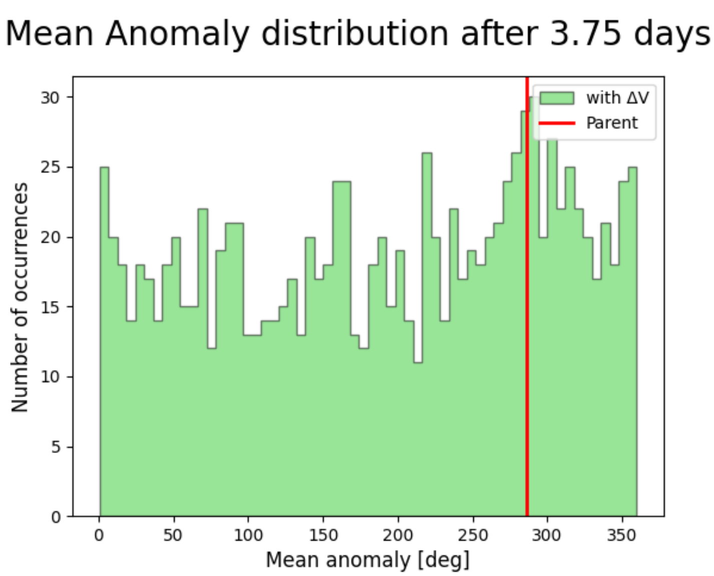

Figure 3.29: Mean anomaly distribution after 90 hours from the break-up

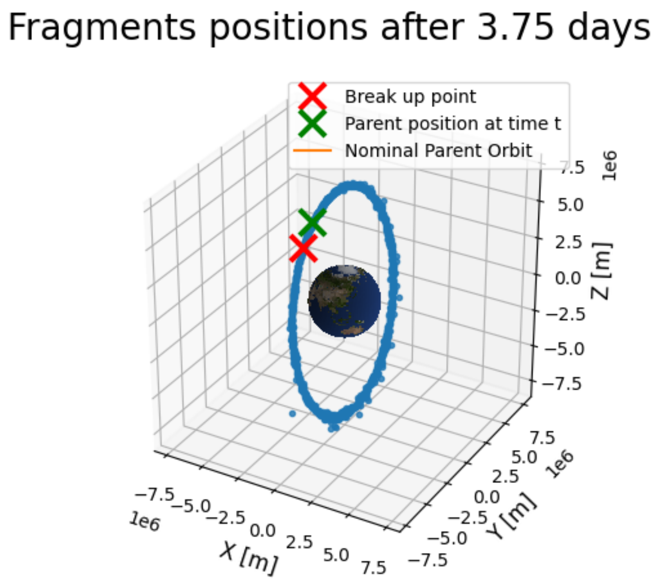

Figure 3.30: Debris cloud shape after 90 hours from the break-up

As a conclusion, this approach has demonstrated that the approach proposed by [29] underestimates the short-term phase duration since it does not consider the whole ensemble of debris.

–4– Debris cloud probability of collision

The discussions presented in the previous chapters have been essential in achieving a full comprehension of the characteristics and behaviour of a debris cloud resulting from an in-orbit break-up event. Chapter 2 clarified how the fragments generated can be described in terms of statistical distributions of size, area-to-mass ratio and ejection velocity using NASA's standard break-up model, highlighting the importance of both norm and ejection direction of imparted velocity. The significance of this aspect was further underscored in Chapter 3, which was crucial to understand how the debris cloud evolves over time.

The primary outcome demonstrated in this chapter is the identification of the conditions and assumptions that occur during the short-term phase. These conditions influence the operational framework of the debris cloud collision risk assessment tool. Furthermore, the duration of this phase plays a significant role in determining the tool's temporal validity.

As stated in Section 1.3, the problem of collision risk assessment in a debris cloud scenario presents several challenges that prevent addressing the issue using the methodologies applied in the classical scenario, where only two objects are involved. The objective of this chapter is to present the methodology developed for calculating the probability of collision of a debris cloud with an operational satellite in the short-term phase. To ensure greater clarity, it is important to gain a deeper understanding of both the classical probability of collision and the debris cloud collision probability problem from a physical and theoretical perspective.

4.1 Classical probability of collision

Before delving into the core issue of collision risk posed by a debris cloud to an operational satellite, this section focuses on analysing the classical collision problem between two objects. The probability of collision has been used as the main parameter to assess the collision risk between two Resident Space Objects (RSOs) since 1981 [30].

Many methods to compute collision probability are only suitable for specific encounter types. Encounters between two RSOs are generally classified into two categories based on their relative motion:

- short-term encounters;
- long-term encounters.

It is important to stress that these terms are not temporal definitions and do not refer to the evolutionary phases of a debris cloud as presented in Section 3.1. Short-term encounters occur with large relative velocities between RSOs, which are on the order of several kilometers per second. Therefore, the time spent in the encounter region is less than a few seconds and the relative velocity remains constant during the encounter, meaning that the relative motion between the two objects in the encounter region can be seen as uniform rectilinear motion. As a consequence, position uncertainties remain constant during the whole encounter and they can be described by two uncorrelated constant covariance matrices, equal to the value at the closest approach point. Furthermore, the velocity uncertainty of two RSOs can be considered negligible since it is significantly smaller compared to their relative velocity. In conclusion, to compute the probability of collisions for short-term encounters, the integration can be reduced to a two-dimensional integral in the encounter plane [30].

On the other hand, long-term encounters refer to encounters with very low relative velocity. The rectilinear motion assumptions become invalid since the time spent in the encounter region is significant. In such cases, the relative velocity can no longer be considered constant. Consequently, the combined error covariance matrices cannot be treated as constant, and the relative trajectory between the two objects becomes curved [30]. Hence, the integral cannot be simplified to a two-dimensional operation.

It is worth better understanding the concept of collision probability. Let r_p and r_s describe the radii of two spheres: the first one circumscribes the primary RSO, the second includes the secondary RSO. The combined sphere of radius $r = r_p + r_s$, denoted as the Hard Body Radius (HBR), is centered on the secondary RSO. If the primary passes in the combined sphere, then a collision will occur and the collision probability is defined as the probability of occurrence of this event [30].

Among all existing procedures to compute the classical collision probability, the most accurate and reliable method is through Monte Carlo simulations, but, on the other hand, it is the most computationally expensive approach [30]. The first step is to randomly sample the initial positions and velocities of two objects according to their error covariance matrices, leading to the generation of many virtual RSOs. Then, the initial orbit states of all virtual objects are propagated for the time of interest, recording the relative distance d of each pair of virtual RSOs over time. If the recorded relative distance is smaller than the HBR, then a collision occurs and it is counted. The total number of collisions N_c recorded is divided by the total number of samples N_t, and the collision probability is given by this ratio, as expressed in the following equation.

$$P_C = Pr(d < HBR) = \frac{N_c}{N_t} \tag{4.1}$$

This procedure is valid to compute the instantaneous collision probability, i.e., the collision probability at a given single time instant. The cumulative collision probability, which is the overall probability of collision within a period of interest, can be computed in the same way, but initial states of virtual RSOs are propagated step by step and collisions are counted at each time instant. However, the reliability of the Monte Carlo simulation depends on the total number of samples, which must be as large as possible, increasing the computational expense and limiting its application in operational scenarios [30]. For this reason, different numerical methods exist to compute the collision probability in both encounter cases, improving the computational time at the expense of accuracy.

To summarise the key point, to calculate the probability of collision for long-term encounters, the required inputs are the state and the position and velocity uncertainties at time of closest approach of both RSOs. In the case of short-term encounters, thanks to the simplifications caused by the assumption of uniform rectilinear motion, the state and only the position uncertainties of the two RSOs at TCA are needed. In the case of a debris cloud, it is not possible to obtain the necessary inputs related to the generated fragments because the cataloguing process takes considerable time, and very small fragments are often lost, as discussed in Section 1.3. This leads to the conclusion that the classical approach for calculating collision probability cannot be applied to the case of a debris cloud.

4.2 Short-term debris cloud probability of collision

The collision risk assessment cannot be approached in the same way for short, medium, and long-term phases due to the different debris cloud dynamics. Estimating the collision risk posed by a debris cloud to an operational spacecraft in the short-term phase is much more challenging than addressing the problem in the medium and long-term phases.

The most suitable way to compute the collision probability in the medium or long-term is through the continuum approach, as proposed by [31]. The continuum approach of the just cited work models the debris cloud as a continuous density distribution, treating it like a fluid and using the continuity equation to efficiently calculate collision probability by averaging the effects of debris over time and space. In addition to its ability to simplify the problem, one of the primary advantages of the continuum approach is its excellent computational efficiency.

By treating the debris cloud as a continuous spatial density distribution, the model avoids the need to track each fragment individually, significantly reducing the computational burden. As a result, the continuum approach is particularly effective for long-term collision risk analysis, where managing a large number of fragments would otherwise be computationally prohibitive.

However, this method cannot be effectively applied in the short-term, because it relies on assumptions of uniformity and continuous distribution, which do not hold immediately after a fragmentation event. In the short-term, the debris cloud is highly irregular and non-uniform, making the averaged effects and fluid-like treatment of the debris inaccurate for predicting collision probability in these initial phases. As explored in Chapter 3, in the short-term phase, the mean anomaly, argument of perigee and right ascension of the ascending node distributions are anything but random. Above all, short-term mean anomaly distribution is highly time-dependent, meaning that the cloud density is highly unstable during this phase. Therefore, an approach that accurately captures this behaviour is necessary. Additionally, in Chapter 3 it was demonstrated through the analysis of orbital parameter distributions that immediately after a break-up event, the only parameter that evolves and changes over time is the mean anomaly, indicating that the short-term phase is governed by Keplerian dynamics. However, during the medium and long-term phases, orbital perturbations such as $J2$ effects and atmospheric drag become significant, making it clear that the assumptions of Keplerian dynamics no longer hold. Therefore, this means that the tool developed and proposed in this thesis, which, as will be shown shortly, operates under Keplerian assumptions, cannot be applied for medium and long-term collision risk assessment.

Methods based on Boundary Value Problems (BVPs) are particularly suited to accurately consider the unstable nature of the short-term phase, since they remove the assumptions inherent in continuous approaches. BVP methods employ a change of variables technique to transform the probability density function from physical conjunction space into the initial spread velocity space [32]. This process involves solving a Lambert's problem, which may require accounting for multiple orbital revolutions over several hours following the event, in order to calculate the velocity (or velocities) necessary to reach the target position [32]. The developed tool proposes the use of boundary value problems and follows the mapping technique initially introduced by [33], which has been recently implemented by [32] and [34].

4.3 Problem description and assumptions

Assume the break-up of a parent object with orbital velocity $\vec{V}_1$ occurring at position $\vec{r}_1$ at time t_0 (break-up time), resulting in the generation of a debris cloud. The event could be either a collision or an explosion; however, for simplicity, an explosion is assumed. Following the break-up, each fragment acquires an additional velocity leading to a new orbital velocity of $\vec{V}_1 + \Delta\vec{V}_i$ for $i = 1, \ldots, N$, where N represents the total number of generated fragments. Consider a primary object with position $\vec{r}_2$ and velocity $\vec{V}_2$ at time of break-up t_0. The goal is to compute the probability of collision between the debris cloud and the primary within a specified time window, consistent with the short-term duration.

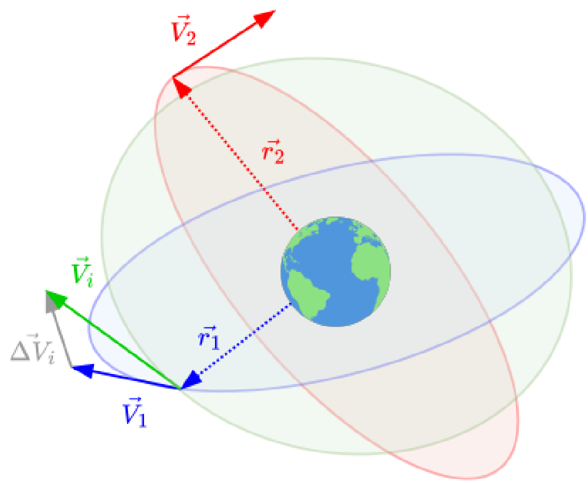

Figure 4.1: Problem description at break-up time

Figure 4.1 provides a graphical representation of the initial conditions. The total number of fragments N and their ejection velocities $\Delta\vec{V}_i$ depend on the specific break-up model involved. In this study, a simplified version of NASA's standard break-up model is used, with further details provided in Section 4.4.5. In any case, the ensemble of ejection velocities can be described by the probability density function of imparted velocity provided by the model. Since the collision probability is calculated by integrating a probability density function over a control volume, the PDF of the imparted velocity can be used to compute the probability of collision for the debris cloud. This requires performing the integral in the velocity space, which is a key concept of the proposed method. This technique will be thoroughly addressed in Section 4.4.1.

The proposed tool works under some simplifying assumptions, which are aligned with the ones employed by the current state of the art:

- Keplerian dynamics;
- Considering the velocity uncertainty of the parent through the SBM;
- Not considering the uncertainty on the parent position at time t_0;
- Not considering the uncertainty on position and velocity of the primary.

First of all, Keplerian dynamics is assumed, meaning that no orbital perturbation is considered. As seen in Section 3.6.2, during the short-term phase the dynamics of the debris cloud is not significantly affected by perturbations, making this a reasonable assumption in the hours immediately following the break-up.

As explored in Section 4.1, uncertainties on position and velocity of both primary and secondary are required in order to estimate the collision probability. The velocity uncertainty of the parent at time t_0 is taken into account through the PDF of ejection velocity provided by the SBM. This approach is actually effective because the SBM is a statistical model, meaning that by definition it is very uncertain and is suitable for considering velocity uncertainties on the initial velocity of the parent.

The uncertainty on the parent position at break-up time, i.e., the break-up epoch, is neglected. This is indeed a strong assumption, given that determining the exact break-up time of a space object is inherently complex and, above all, not deterministic. Nevertheless, in Section 5.3, an original method is proposed to account for these uncertainties.

The uncertainties on both position and velocity of the primary are also neglected. At first glance, these assumptions of neglecting uncertainties might seem hazardous and overly simplistic. However, the key factor that makes them more acceptable is the use of the SBM. Since it is an inherently statistical model with significant uncertainties and approximations, the uncertainties it introduces on the parent velocity far outweigh the remaining ones. As a result, the uncertainties on the parent position, the primary velocity and position are effectively masked by the larger uncertainties associated with the SBM. It is important to note that these assumptions are commonly made in most state-of-the-art studies because the problem is already highly complex, even with these simplifications.

The work proposed by [32] actually solves the problem of considering uncertainties, removing these simplifying assumptions. The uncertainties are managed through high-order Taylor expansions and automatic domain splitting techniques, enabled by differential algebra, which represents a much more complex approach.

4.4 Adopted methodology

This section offers a comprehensive analysis of the method employed to calculate the collision probability of a debris cloud. The approach is grounded in the theoretical and mathematical principles originally introduced by [33]. By delving into these fundamentals, this analysis not only clarifies the underlying methodology, but also demonstrates how these principles are integrated into the practical application of the tool.

4.4.1 Mapping of the primary into spread velocity space

Before delving into the mathematical details, it is worth introducing and defining the spread velocity space at time of break-up t_0. When a break-up event occurs, each fragment of the debris cloud acquires an additional velocity. These $\Delta\vec{V}$ vectors can be represented within a new conceptual framework known as the spread velocity space at time of break-up t_0. In this space, each point corresponds to a $\Delta\vec{V}$ vector associated with an individual fragment. The spread velocity space effectively visualises the distribution of these velocity changes immediately following the break-up, providing a clear representation of how the fragments disperse from the original object.

Debris cloud motion can be interpreted as a time-dependent mapping from spread velocity space at time of break-up t_0 to physical position space at a certain time t. This relationship can be mathematically expressed as below.

$$\vec{r}(t) = g(\vec{r}_0, \vec{V}_0, \frac{A}{m}, t) = h(\Delta\vec{V}, \frac{A}{m}, t) \tag{4.2}$$

In the above equation, $\vec{r}(t)$ represents the ECI position of a fragment at time t and can be described through two different functions. Firstly, it can be linked to its initial ECI position $\vec{r}_0$ and velocity $\vec{V}_0$ at time of break-up, thanks to the propagator function g. Obviously, this function also requires the area-to-mass ratio of the fragment A/m and the time of propagation t as input. The second relation involves a different function h, equivalent to g, but it maps the fragment image $\Delta\vec{V}$ in spread velocity space at time of break-up to position $\vec{r}(t)$ at time t. Indeed, $\Delta\vec{V} = \vec{V}_0 - \vec{V}_{P0}$ is the fragment position vector in the initial spread velocity space, where $\vec{V}_0$ is the ECI orbital velocity of the fragment just after the break-up and $\vec{V}_{P0}$ is the ECI velocity of the debris cloud center of mass at break-up time (i.e., the parent orbital velocity at time t_0). For each fragment of the debris cloud, there is at least one image point in spread velocity space.

For our application, these theoretical foundations are leveraged not to map the position of a fragment from spread velocity space to physical position space, but rather to execute the mapping of the primary position $\vec{r}_2(t)$ over time into spread velocity space at the time of break-up t_0.

Figure 4.2 is valuable for clarification purposes. A parent object, represented in blue, is considered and it is assumed to break-up at time t_0 at position $\vec{r}_1(t_0)$. On the other hand, an arbitrary primary object, represented in red, has position $\vec{r}_2(t_0)$ at time of break-up. Obviously, its position will evolve over time. Because of the fragmentation event, each fragment acquires an additional velocity $\Delta\vec{V}_i$, which changes their initial orbital velocity, equal to the parent value. This means that their state vectors change and they jump on new trajectories, which may or may not hit the target. This whole discussion happens in the physical position space. Based on the previous statements, the mapping of the primary trajectory into the spread velocity space can be performed by answering the following question: What is the $\Delta\vec{V}_i$ that a fragment at position $\vec{r}_1(t_0)$ with velocity $\vec{V}_1$ at time t_0 should have to collide with the primary at position $\vec{r}_2(t^*)$ at time t^*? If this discussion is carried out for every position of the primary in time, it is possible to obtain a series of $\Delta\vec{V}_i$ that fragments should have to cause a collision in the future. Therefore, the primary trajectory in the spread velocity space is represented by this series of additional velocities, which is indicated as the orange trajectory in Figure 4.2.

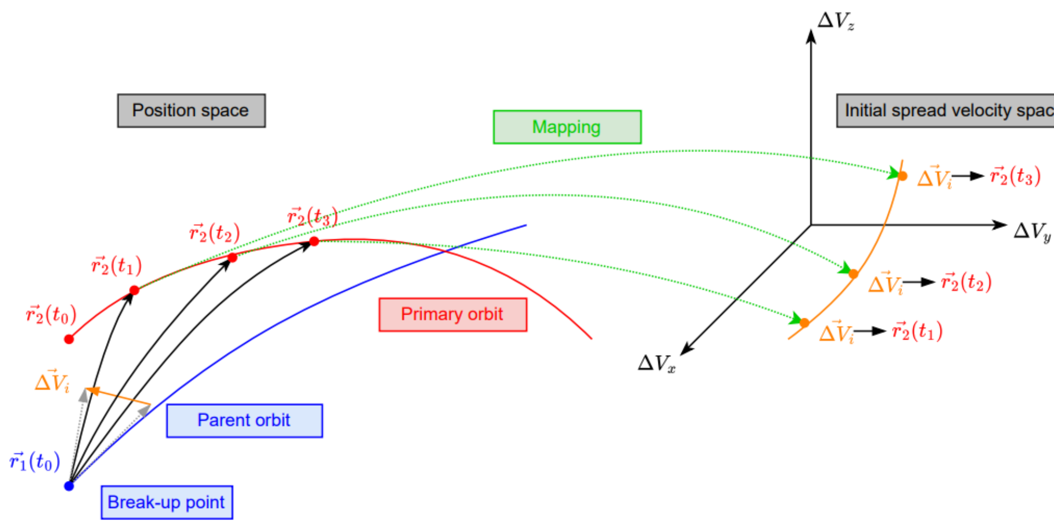

Figure 4.2: Mapping of the primary into spread velocity space

The solution to the previous question is provided by Lambert's problem, which is able to determine an orbit from two position vectors and the Time Of Flight (TOF). Consequently, the primary trajectory is continuously mapped into the spread velocity space, solving the Lambert's problem from the break-up position $\vec{r}_1(t_0)$ to $\vec{r}_2(t)$ in a TOF $\Delta t = t - t_0$ for each time instant t.

The actual solution provided by Lambert's problem is the orbital velocity of the transfer orbit linking the two position vectors. From the latter, the required additional velocity can be computed as $\Delta\vec{V}_i = \vec{V}_{Lam} - \vec{V}_1$. The real advantage of this methodology is that each $\Delta\vec{V}_i$ corresponds to a given value of the probability density function of ejection velocity provided by the SBM.

As a consequence of the fact that the collision probability is the integration of a PDF in a control volume, it can be computed by integrating the ejection velocity probability density function in the spread velocity space. In other words, the problem addressed solves the following question: What is the probability that a fragment acquires that $\Delta\vec{V}_i$ from the fragmentation event?

4.4.2 Lambert's problem

The Lambert's problem is defined as a boundary value problem for an object in a Keplerian force field [35]. The solutions to the Lambert's problem connect specified terminal positions and a given time of flight through conic sections. The output is the orbital velocity required to be on the transfer trajectory. The inputs required by the problem are the following:

- Cartesian 3D terminal position vectors: r_1 and r_2, interpreted as initial and final position;
- Desired time of flight Δt;
- Short or long-way solution, depending on the transfer angle, which defines the direction of motion (prograde or retrograde);
- Number of complete revolutions R.

Notably, more than one solution may be possible to link two position vectors within a specified TOF. In fact, the Lambert's problem can admit up to a maximum of $2R_{\max} + 1$ solutions per each sense of motion, where $R_{\max}$ is the specified maximum number of revolutions. It is well known that the zero-revolution Lambert's problem has a unique solution for every $\Delta t > 0$ per each direction of motion.

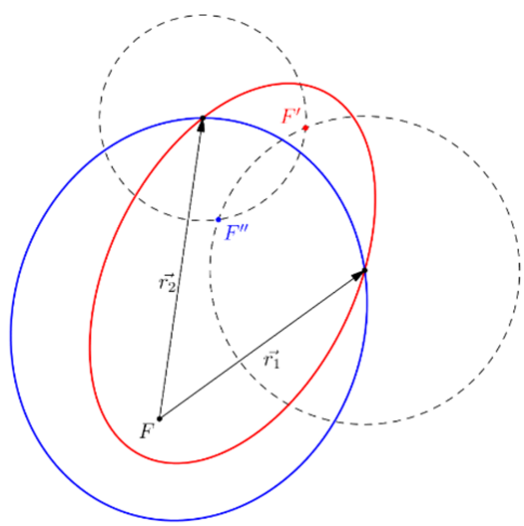

Figure 4.3: High and low path Lambert's solutions [36]

However, in the case of multiple revolutions, there are two solutions per each direction of motion: the short way or the long way, depending on their orbital period. If two solutions are found, they are distinguished as the short-period (SP) and long-period (LP) solutions. Figure 4.3 [36] shows two solutions for the same conditions. The red orbit has its focus F' higher than the segment $\overline{\vec{r_1}\vec{r_2}}$, while the blue orbit has its focus F'' lower. For this reason, the first orbit is referred to as the high-path orbit and, in contrast, the second orbit is defined as the low-path orbit. Both trajectories can be traced in two directions, resulting in one transfer path shorter than the other.

All solutions are of interest because the objective is to compute the collision probability, thus, all ΔV vectors leading to a future collision must be considered in the integration. Consequently, there will not be a single continuous trajectory representing the primary in the spread velocity space. For a fixed time instant (time of flight), there might be multiple solutions, i.e., different $\vec{\Delta V}$ vectors, resulting in several distinct trajectories that branch and multiply over time.

However, not all of these solutions correspond to physical orbits. For example, some trajectories might theoretically intersect the Earth's center or enter the atmosphere before eventually reaching the final position, which would not be feasible for practical scenarios.

Obviously, in the specific application of mapping, the number of solutions of the Lambert's problem for a fixed position of the primary $\vec{r_2}(t^*)$ depends on the time of flight $\Delta t = t^* - t_0$. It is impossible to have a solution that involves one or more revolutions if the TOF is very short, as there would not be enough time to complete the trajectory and still reach the final position, in accordance with the orbital period.

4.4.3 Collision probability integral formulation

Once the key concept of the methodology has been explored, the formulation of the integral that expresses the probability of collision can be addressed. Following [33], the probability of collision between the primary satellite and a single fragment P_i can be computed by determining the probability that the fragment will acquire a spread velocity inside any of the paths swept out by the satellite image in the spread velocity space. Mathematically, P_i is expressed by Equation 4.3.

$$P_i = \int_{\zeta} f(\Delta V)\, \mathrm{d}\mathcal{V} \tag{4.3}$$

The above integral is performed in the spread velocity space. In the equation, ζ is the primary object path in the spread velocity space, $f(\Delta V)$ is the ΔV probability density function, and $\mathrm{d}\mathcal{V}$ is the differential volume swept by the primary image in a time $\mathrm{d}t$ in the spread velocity space [32]. It is worth noting again that, within this context, the primary image represents the ensemble of ejection velocity vectors that correspond to the spacecraft position in physical space at a given time. The differential volume can be rewritten as in Equation 4.4.

$$\mathrm{d}\mathcal{V} = A \left\| \frac{\mathrm{d}\vec{\Delta V}}{\mathrm{d}t} \right\| \mathrm{d}t \tag{4.4}$$

In this expression, A is the collision cross-section of the primary in the spread velocity space, whose normal is parallel to $\frac{d\Delta\vec{V}}{dt}$. The latter, i.e., the time derivative of the position vector in spread velocity space, should not be interpreted as an acceleration, but as the "velocity in the velocity space" [33]. In this way, the product between the norm of the latter and dt represents a position in the spread velocity space.

Substituting Equation 4.4 into Equation 4.3, the collision probability that a single fragment hits the primary can be rewritten as follows.

$$P_i = \sum_k \int_{T_k} f(\Delta V_k) A_k \left\| \frac{\mathrm{d}\Delta\vec{V}_k}{\mathrm{d}t} \right\| \mathrm{d}t \tag{4.5}$$

In the above expression, the summation is required because of the simultaneous presence of multiple paths for a sufficiently long propagation window, which potentially leads to more than one Lambert's solution,i .e., conjunctions occurring at the same time instant but after a different number of revolutions of transfer orbit. The integration interval T_k depends on the time length of each path.

A graphical representation of the integral in Equation 4.5 is provided by Figure 4.4. In each primary image ΔV_i in the spread velocity space, a differential volume, indicated as a green cylinder, is centered, and it is the one swept by the satellite image. The latter is an ellipsoid. The cylinder cross-section is the satellite cross-section in spread velocity space with A_k as basis, whose normal is parallel to the time derivative of the position vector in spread velocity space, as previously stated. The next section will present the procedure to compute the collision cross-section of the primary image starting from the ellipsoids.
As it will be seen in Section 4.4.6, this integral is calculated numerically. This is due to the fact that the primary trajectory is discretised over time in order to provide the time of flight and the final position (primary position) as input to the Lambert's solver. This does not allow the integral to be solved analytically. For this reason, there will be zones of under or over-estimation, depending on the shape of the path in spread velocity space. Specifically, there may be a zone where two consecutive differential volumes overlap, causing the same information to be considered twice, or a zone where a gap exists between two consecutive differential volumes, resulting in some information being completely overlooked. These approximation errors can be reduced by decreasing the time step dt, although this comes at the cost of increased computational time, as it requires solving a greater number of Lambert's problems.

However, the objective is not to evaluate the collision probability of a single fragment from the debris cloud, but rather to assess the risk posed by the entire cloud. Once the collision probability of only one fragment is computed through Equation 4.5, the probability of collision caused by the entire cloud P_C is estimated through the following relationship, where N is the total number of debris.

$$P_C = 1 - (1 - P_i)^N \tag{4.6}$$

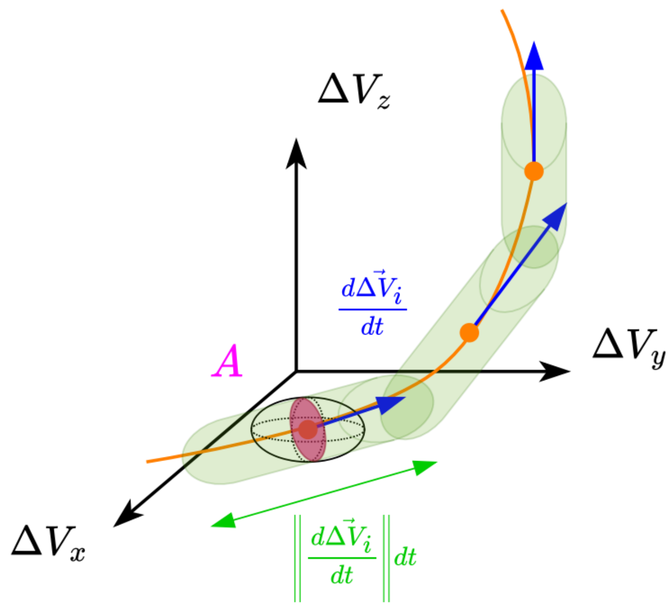

Figure 4.4: Integral evaluation

This expression arises from the fact that if the probability of a single fragment from the cloud colliding with the primary is P_i, then $(1-P_i)$ is the probability that the fragment does not cause a conjunction. Raising the latter to the power of N results in the probability that no fragment collides, given that there are N fragments and assuming that the collisions of individual fragments with the primary are independent events. Therefore, $1-(1-P_i)^N$ represents the probability that at least one fragment from the debris cloud collides with the primary within the given time window.

4.4.4 Collision cross-section in the spread velocity space

As it is considered in the classical conjunction 1-vs-1 scenario, the dimension of the two colliding objects should be taken into account. In this specific case, the dimension of fragments can be neglected for two main reasons. Firstly, the majority of fragments is much smaller than the entire platform. Additionally, given that their size cannot be easily and deterministically estimated, it is sufficient to consider only the primary. Since the integral to compute the collision probability is calculated in the spread velocity space, the collision cross-section must be expressed in this space.

Following [33], the relationship between collision cross-section and the differential volume in spread velocity space can be determined as follows. Consider the first variation of

Equation 4.2, shown in the following expression, in which the area-to-mass ratio is assumed to be constant.

$$\delta\vec{r} = \frac{\partial h}{\partial \Delta\vec{V}}\delta\Delta\vec{V} + \frac{\partial h}{\partial t}\delta t \tag{4.7}$$

In the latter, $\delta\vec{r}$ is the differential position change of the primary in a differential time interval δt in position space, and hence, it can be expressed as in Equation 4.8. The velocity variation $\delta\Delta\vec{V}$ corresponds to the differential position change of the satellite image in spread velocity space.

$$\delta\vec{r} = \vec{V}_{Pri}\delta t \tag{4.8}$$

The term $\vec{V}_{Pri}$ is the ECI velocity vector of the primary. Partial derivatives of the function h are well known. The first term is the 3 by 3 subset of the orbital state transition matrix $\mathbf{\Phi}$, which links the spread velocity space at break-up time t_0 to position space at time t. The time derivative of h is simply the ECI velocity vector of the fragment. The two expressions are summarised in the following equation.

$$\begin{aligned} \frac{\partial h}{\partial \Delta\vec{V}} &= \mathbf{\Phi}_{3x3}(\vec{r}_0, \vec{V}_0, t) \\ \frac{\partial h}{\partial t} &= \vec{V}_F(t) \end{aligned} \tag{4.9}$$

The velocity of the primary relative to the fragment $\vec{V_{PF}}$ can be expressed as follows.

$$\vec{V_{PF}} = \vec{V_{Pri}} - \vec{V_F} \tag{4.10}$$

Substituting Equation 4.8, 4.9 and 4.10 in 4.7, the following relationship is obtained.

$$\vec{V_{PF}}\delta t = \mathbf{\Phi}_{3x3}(\vec{r}_0, \vec{V}_0, t)\delta\Delta\vec{V} \tag{4.11}$$

This equation is the first order approximation to the mapping from spread velocity space to position space referenced to the local cloud motion. Differential volumes in the position space and spread velocity space can be related through the relationship between two differential volumes derived from advanced calculus. The absolute value of the Jacobian determinant J, which corresponds to the determinant of the linear mapping $\mathbf{\Phi}_{3x3}(\vec{r}_0, \vec{V}_0, t)$, measures the ratio of corresponding volumes for small regions near the chosen point [37]. The differential volume in position space represents the volume swept by the satellite during a differential time interval δt, and can be expressed by multiplying the collision cross-section A_r in the position space by the distance travelled during δt. By applying principles of advanced calculus, the relationship between the differential volume in position space $\Delta\mathcal{V}_r$ and in spread velocity space $\Delta\mathcal{V}_v$ is expressed as follows.

$$\Delta\mathcal{V}_r = A_r\|\vec{V_{PF}}\|\delta t = |J|\Delta\mathcal{V}_v \tag{4.12}$$

However, since the integral presented in Equation 4.5 is not performed in the position space, it requires the collision cross-section in the spread velocity space. It can be easily computed assuming that the primary is a sphere of diameter D in the physical position space. A sphere in the position space is mapped into an ellipsoid in the spread velocity space. The transformation is mathematically obtained through the sub-part of the state transition matrix that links the position at time t to the velocity at time t_0.

The equation of transformed ellipsoid in the spread velocity space is expressed by Equation 4.13, which has been derived by [32].

$$\Delta\vec{V}^T \mathbf{\Phi'}^T_{3\times3}(t)\mathbf{\Phi'}_{3\times3}(t)\Delta\vec{V} = \left(\frac{D}{2}\right)^2 \tag{4.13}$$

The matrix $\mathbf{\Phi}'_{3x3}$ is the subpart of the state transition matrix that links the position at time t to the velocity at time t_0. From this expression, the matrix representing the ellipsoid can be easily recognized. Now, the ellipsoid must be projected onto the plane whose normal is parallel to the time derivative of the $\Delta\vec{V}$ vector. The projection of an ellipsoid is an ellipse, whose area is the collision cross-section in the spread velocity space and can be computed as follows.

$$A = \pi ab \tag{4.14}$$

The lengths of the semi-major axis a and the semi-minor axis b of the projected ellipse can be computed by finding the eigenvalues of the ellipse matrix.

As a conclusion, Figure 4.5 shows graphically the transformed ellipsoid and the collision cross-section in the spread velocity space.

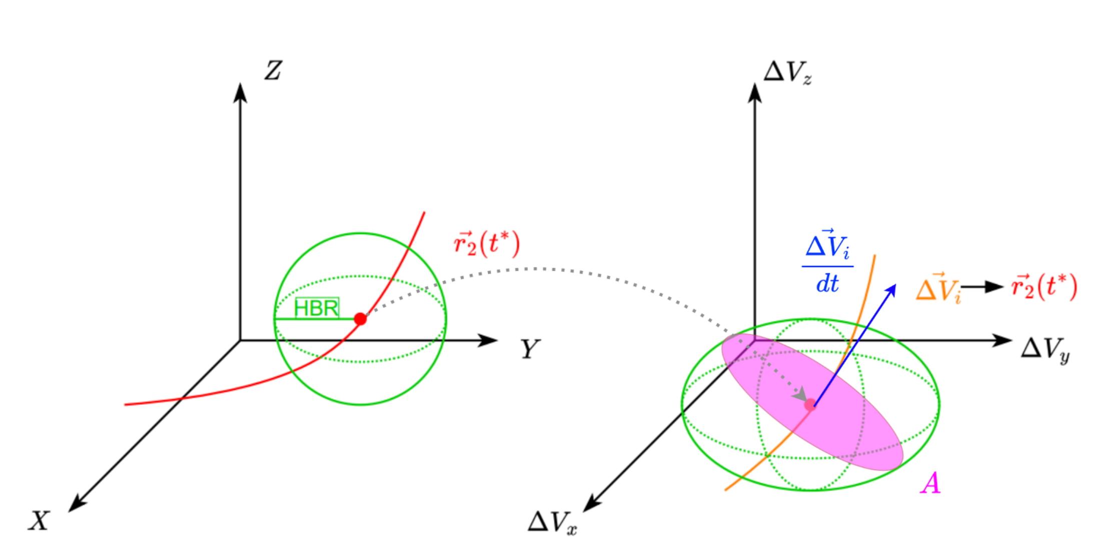

Figure 4.5: Sphere in position space to ellipsoid in spread velocity space transformation

An important feature to highlight is that the ellipsoids tend to shrink over time, leading to a reduction in the primary cross-sectional area in the spread velocity space. This causes the integration volume to become thinner. This is due to the fact that as the debris cloud evolves, its density decreases, reducing the probability of collision [33].

4.4.5 Probability density function of ejection velocity

The last piece that is missing in the probability integral of Equation 4.5 is the probability density function of ejection velocities. As explored in Chapter 2, NASA's SBM provides ejection velocities PDF in terms of magnitude only, but ejection directions are needed to fully characterise a debris cloud. However, the norm's PDF of the SBM depends on the specific area-to-mass ratio value, which in turn depends on the extracted characteristic length.

For the sake of simplicity, in this work a simplified PDF is used, which is not influenced by the specific value of area-to-mass ratio. The PDF in question has been developed in the work [38]. The initial distribution of $log_{10}\Delta V$ is assumed to be normal, with mean $\mu = 2.63[log_{10}m/s]$ and standard deviation $\sigma = 0.482[log_{10}m/s]$. As is clear, the standard deviation is constant and does not depend on the area-to-mass ratio value. This distribution has already been adopted in the literature, for example by [34].

At this point, it is clear the importance and role of ejection direction models. According to the state of the art, an isotropic ejection model is assumed. Hence, the PDF of ejection velocity vectors can be expressed as follows.

$$f(\vec{\Delta V}) = \frac{f(log_{10}\Delta V)}{4\pi\Delta V^2[\Delta V ln(10)]} \tag{4.15}$$

The above equation shows the PDF of ejection velocity norms divided by the surface of a sphere of radius equal to ΔV norm, which reflects the meaning of the isotropic nature of the ejection direction model. A correction factor due to the fact that the numerator is a distribution of $log_{10}\Delta V$ is included.

Theoretically, each ΔV corresponds to a given PDF value, which has a contribution in the overall probability of collision. However, very high and very low ejection velocity norms lead to very small PDF values, because there is a reduced likelihood of such extreme velocities in a break-up. As a consequence, a maximum ejection velocity value ΔV_{Max} exists, above which the PDF value is considered negligible. This means that if the Lambert's solution corresponds to an extreme ΔV, it will not contribute to the overall probability. This approach allows to save computational time, since these solutions can be completely neglected.

4.4.6 Implementation

This section aims at presenting some details about the practical implementation of the theoretical methodology just explored. The tool has been developed in Python, it manages cases of in-orbit explosions (only one parent is considered) and requires the following inputs:

- State vectors or Keplerian elements of the primary and the parent at time of break-up t_0;
- Size parameter of the primary, i.e., the radius of the sphere HBR;
- Simulation time T;
- Number of generated fragments.

The simulation time, representing the period of interest for evaluating collision risk, is used as the upper bound to generate a discretised time vector, while the break-up time t_0 represents the starting point. The time step is fixed to 10 seconds, as a trade-off between computational time and accuracy.

Then, inputs for the Lambert's solver are generated. The starting position corresponds to the break-up position, which can be extracted from the state vector or Keplerian elements set of the parent. The final position is the position of the primary at any time instant of the time vector. In order to obtain the latter, the primary is propagated using an analytical propagator, thus in unperturbed motion, along the time vector. Finally, the times of flight vector is generated, simply performing the $t - t_0$ operation for each element of the time vector.

At this point, a series of Lambert's problems for each couple of final position and TOF is solved. The employed Lambert's solver is based on Izzo's algorithm [39], which is capable of managing multi-revolutions problems. The solver requires the number of revolutions R, a boolean prograde=[True,False] representing the direction of motion, and a second boolean low_path=[True,False] to select the type of orbit if two solutions are available. The parameter low_path refers to short-period or long-period solutions presented in Section 4.4.2. Therefore, it should be clear that a consistent number of Lambert's problems must be solved, one for each combination of number of revolutions, direction of motion and type of orbit, affecting the computational time. The maximum number of revolutions leading to the existence of at least one solution depends on the time of simulation T. In a LEO scenario, the orbital period of a generic transfer orbit is $T_t \sim 90min$, so the maximum number of revolutions allowed can be computed as T/T_t. Of course, as also stated in Section 4.4.2, there is a minimum TOF for which a given number of revolutions is feasible. This leads to the fact that for initial values of times of flight vector there are no solutions for a higher number of revolutions.

Once a Lambert's solution is provided, the additional velocity needed to jump on this trajectory is computed as $\vec{\Delta V} = \vec{V_{Lam}} - \vec{V}_1$, ensuring consistency of reference frames. When all $\vec{\Delta V}$ for a given combination of [R, prograde, low_path] are available, their time derivatives are computed with a forward scheme, while for the last point the backward scheme is used. The direction of each time derivative vector is computed in order to find the plane onto which the ellipsoid must be projected later.

As previously mentioned, not all solutions represent physical orbits. First of all, some transfer orbits may first intercept the Earth's center or enter the atmosphere (causing de-orbiting) and then actually collide with the primary. Obviously, these solutions are not of interest, since they do not pose a real risk for the primary. Additionally, as stated in Section 4.4.5, it is unlikely that a fragment would have an extreme ΔV from the break-up. For this reason, transfer orbits requiring a $\Delta V > \Delta V_{Max}$ are not of interest, as they do not significantly contribute to the overall analysis. Therefore, a filtering step on these two conditions is applied, which has the advantage of saving computational time.

Then, the mapping of the primary sphere into an ellipsoid in the spread velocity space is performed. The ellipsoids are projected on the local plane, whose normal has the direction of the time derivative of ejection velocity vectors, previously computed. The projection is an ellipse, of which the area is computed.

Once all pieces of the integral of Equation 4.5 are known, the integration is performed numerically. For each time instant, probability values of all [R, prograde, low_path] combinations are summed together. Finally, the cumulative collision probability related to only one fragment is computed, and then transformed to the cumulative debris cloud collision probability through Equation 4.6. The just described algorithm is summarised in the following pseudo-code.

Algorithm 1 Debris cloud collision probability calculation

Input: Initial state vectors of Parent SV_1 and Primary objects SV_2, simulation time T, dimension of the Primary HBR, number of generated fragments N
Generate time vector t_{vec} from t_0 to $t_0 + T$ with a time step $dt = 10s$
Set the position of the Parent at t_0 as the initial position r_1
for each t in t_{vec} **do**
    Propagate the Primary and compute its position r_2
    Take the state transition matrix $\mathbf{\Phi}$
end for
for each combination of R, prograde, and low_path **do**
    for each time of flight Δt **do**
        Solve Lambert's problem with terminal positions r_1 and $r_2(\Delta t)$
        Compute ΔV required for the transfer $\Delta V = V_{Lam} - V_1$
        Calculate $\frac{\mathrm{d}\Delta\vec{V}}{\mathrm{d}t}$
    end for
    Filter for physical solutions
    for each ΔV **do**
        Transform the Primary sphere into an ellipsoid in the spread velocity space through the subpart of $\mathbf{\Phi}$
        Project the ellipsoid onto the plane where the normal is aligned with $\frac{\mathrm{d}\Delta\vec{V}}{\mathrm{d}t}$
        Find the area of the projected ellipse
        Extract the PDF value for a given ΔV
        Compute the instantaneous collision probability P_i of a single fragment
    end for
    Compute the cumulative collision probability P_{Ci} of a single fragment
end for
Compute the cumulative P_C of the debris cloud $P_C = (1 - P_{Ci})^N$
Output: Cumulative PoC P_C of the debris cloud over the simulation time

–5–
Testing and validation

The previous chapter provided a detailed overview of the methodology for the debris cloud collision risk assessment just after the break-up. This chapter aims at presenting how the developed tool has been tested.

The Python tool has been validated by comparing its results for a test case commonly found in the literature with results of reference. Indeed, the latter has been used in many works, like the ones proposed by [32], [34] and [40], in which their own methodologies are presented and implemented. However, the ground truth of the test case resides in the Monte Carlo simulation, which was performed and successfully compared with the results obtained from the previously mentioned works.

Additionally, to position the tool within an operational context, the collision probability is presented in relation to the maneuver threshold.

5.1 Analysis of the test case

The test case of interest simulates the collision risk posed by a debris cloud generated by the explosion of a 900 kg satellite, referred to as Brksat, producing 2.2×10^6 fragments larger than 1 mm. The probability of the debris cloud impacting the International Space Station (ISS) is computed over a period of 6 hours following the break-up event. Table 5.1 shows the initial orbit parameters of the primary and the parent at time of break-up. The ISS has a length of about 100 m, thus the radius of the sphere in position space is set to 50 m. It is also worth mentioning that the time step is set to 10 seconds.

Object	a [km]	e	i [°]	Ω [°]	ω [°]	ν [°]
ISS	6800	1.800×10^{-4}	51.6	0	359.9973	307.7498
Brksat	7000	2.697×10^{-2}	50	0	180	139.6759

Table 5.1: Orbital parameters of ISS and Brksat

Figure 5.1 provides a graphical perspective of the initial situation in TOD, in which the primary is represented in red, while the parent in blue and their position at break-up time are indicated as crosses.

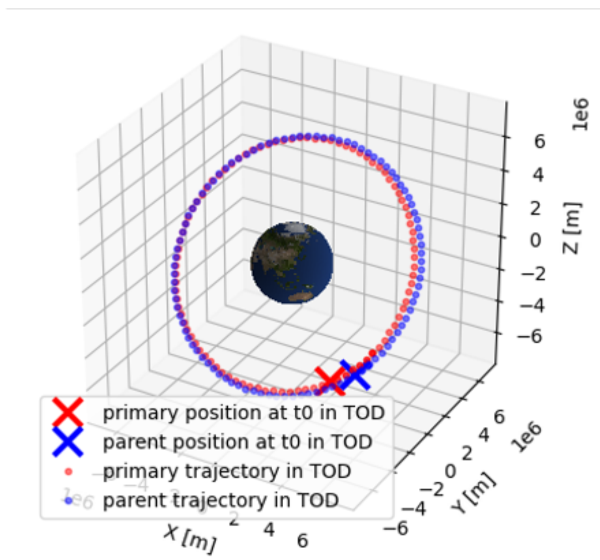

Figure 5.1: Orbits of the ISS and Brksat

Since the test case is in a LEO scenario, the minimum period of a generic transfer orbit is about 90 minutes. As stated in Section 4.4.6, the maximum number of revolutions allowed can be obtained by dividing the time of simulation by the minimum period of the transfer orbits. Considering a simulation time of 6 hours, this leads to 4 revolutions at maximum. This means that for each time instant, there are theoretically $2(2R_{\text{max}} + 1) = 18$ solutions at maximum. Practically speaking, it is not true that for each time instant (every TOF) all possible solutions are available, according to the issue of not enough time to do one or more revolutions presented in Section 4.4.2. Additionally, not all solutions are feasible.

Now the ensemble of Lambert's solutions is analysed. For example purposes, Figure 5.2 and 5.3 represent the transfer orbits for two different arbitrary settings of Lambert's problem: $[R = 0, prograde = False]$ and $[R = 1, prograde = True, low\_path = False]$, respectively. These trajectories start from the blue cross, which represents the break-up position, and end up at different positions on the primary orbit. Lambert's orbits are coded in colour gradient, which is representing the ΔV norm required to jump on these trajectories. Darker colours are associated with lower values of required additional velocity. Some observations can be made.

First of all, the general trend is that the lower the time of flight, the higher the required additional velocity, which can reach unfeasible values. As stated in the colour legend, the yellow orbits for the $[R = 0, prograde = False]$ case, that are linked to very short times of flight, may require up to 10000 m/s of additional velocity, which is clearly an enormous value. This happens for transfer orbits that ends at locations very close to the initial primary position.

Another behaviour that can be registered is the fact that, for a specific case, different families of transfer orbits can be observed. In general, the number of solutions tends to reduce as R increases. Additionally, transfer orbits change depending on the number of revolutions. Indeed, the situation in the first case is much different than the second case. To achieve greater graphical clarity, these plots have been generated setting a time step of 5 minutes, instead of 10 seconds by default. The entire ensemble of Lambert's orbits, for example for $[R = 0, prograde = False]$, is presented in Figure 5.4. In the latter, the presence of different families of transfer orbits is much more visible.

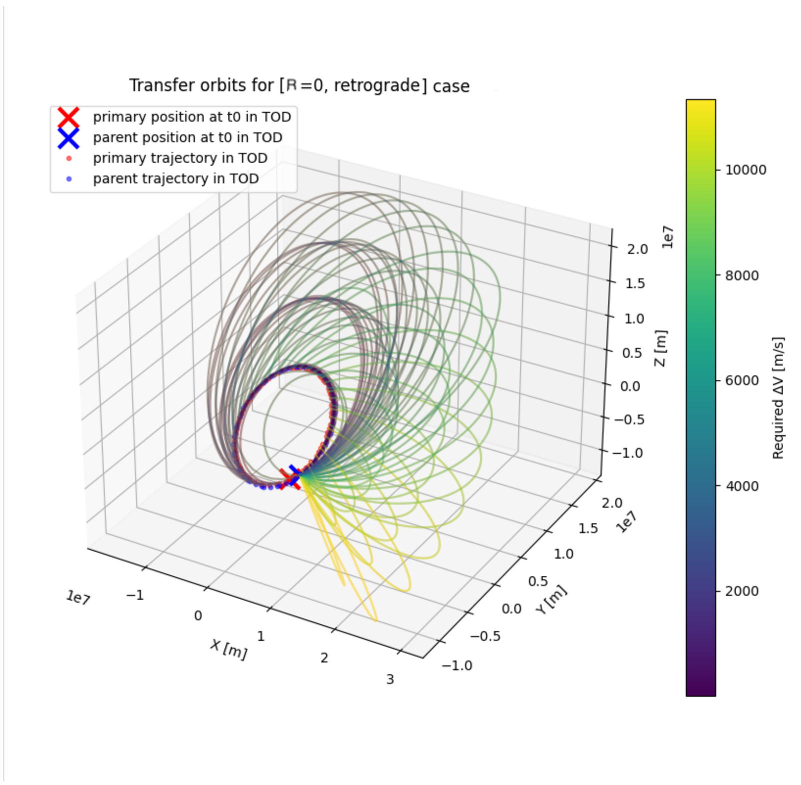

Figure 5.2: Lambert's solutions for $[R = 0, prograde = False]$ and dt=5 min

As already mentioned, not all solutions represent feasible orbits. The reasons they may not be so include premature decay or an excessively large required ΔV, which corresponds to a negligible PDF value. The latter is fixed to 3890 m/s, as done in [32]. Therefore, the tool applies a filtering step. Figure 5.5 shows the situation caused by pruning the solutions for $[R = 0, prograde = False]$. Red trajectory are filtered out, while green ones are kept. One of the red trajectories actually collides with the Earth's center before reaching the primary. The remaining red orbits are filtered out because the required additional velocity is $\Delta V > 3890 m/s$.

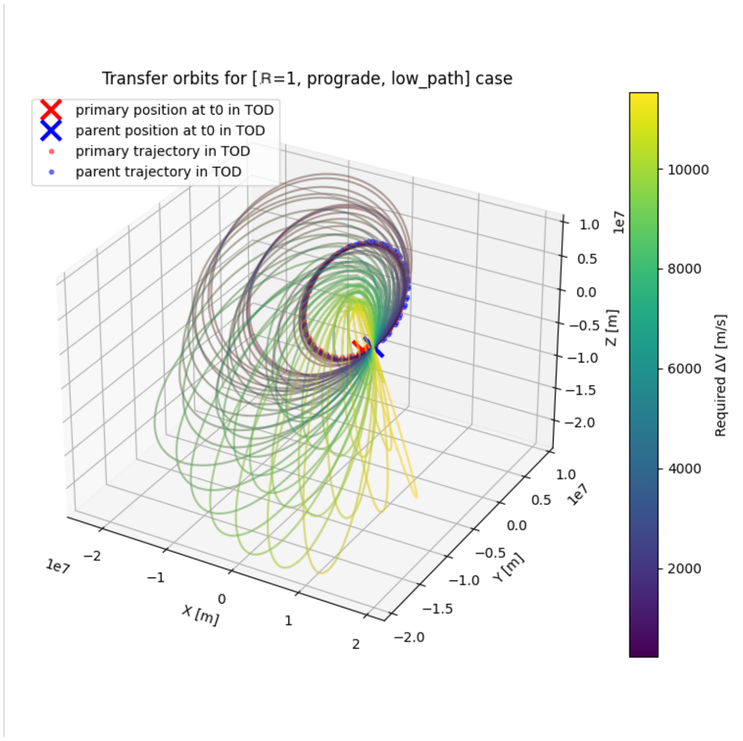

Figure 5.3: Lambert's solutions for $[R = 1, prograde = True, low\_path = False]$ and dt=5 min

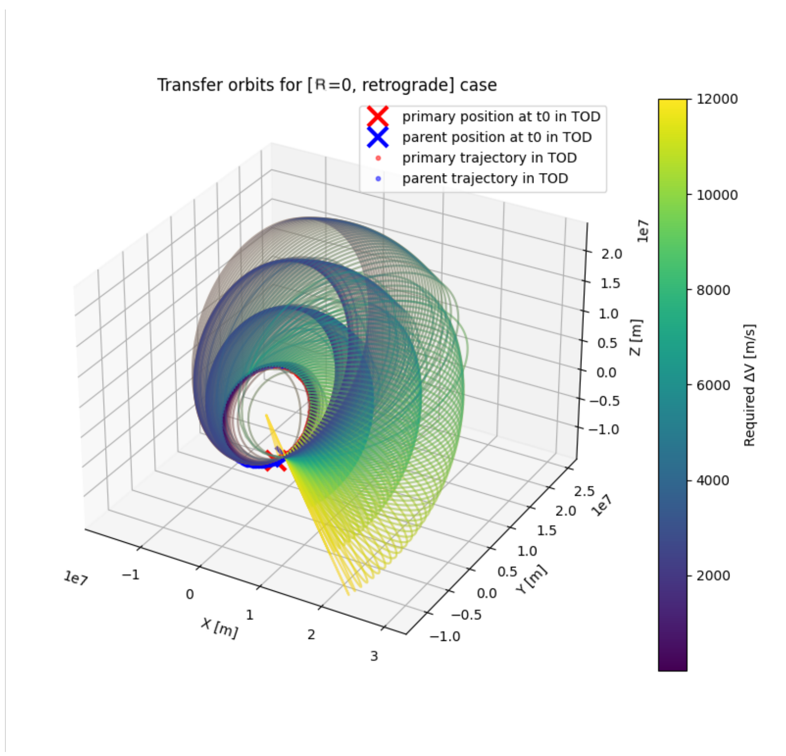

Figure 5.4: Lambert's solutions for $[R = 0, prograde = False]$ and dt=10s

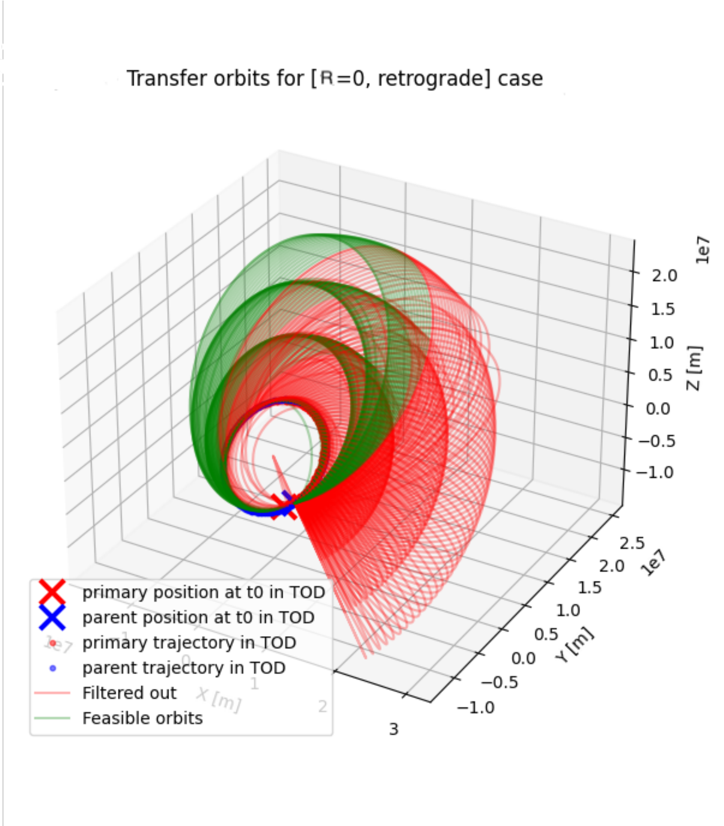

Figure 5.5: Lambert's solutions for $[R = 0, prograde = False]$ after filtering

It is interesting to observe the behaviour of required additional velocity over time, shown in Figure 5.6. It can be noticed that a few moments after the break-up, the ΔV norms required are huge, because the TOF is very short. After a while, they reduce and the behaviour seems to repeat with a period of about 5000 seconds. This value corresponds more or less to the orbit period of the primary and the parent, since their orbits are very similar. The relative geometry repeats periodically, causing this periodic behaviour.

At this point, the analysis can proceed in the spread velocity space. As a proof that there is not only one continuous trajectory of the primary in this space, Figure 5.7 represents the primary image for case $[R = 0, prograde = False]$ only, after filtering. It can be clearly observed the presence of different trajectories. After a while, their shape almost repeats for the same reason of the ΔV behaviour over time presented in Figure 5.6. An even more important feature is the fact that the trajectory of each case is not continuous, but has some discontinuities. These interruptions occur when there is a transition of solutions from one transfer orbit family to another. The closer these trajectory are to the mean of the ejection velocity PDF, the higher the overall collision probability will be. Obviously, while the primary has a unique trajectory in the position space, it will trace different paths in the spread velocity space according to the settings of the Lambert's problem.

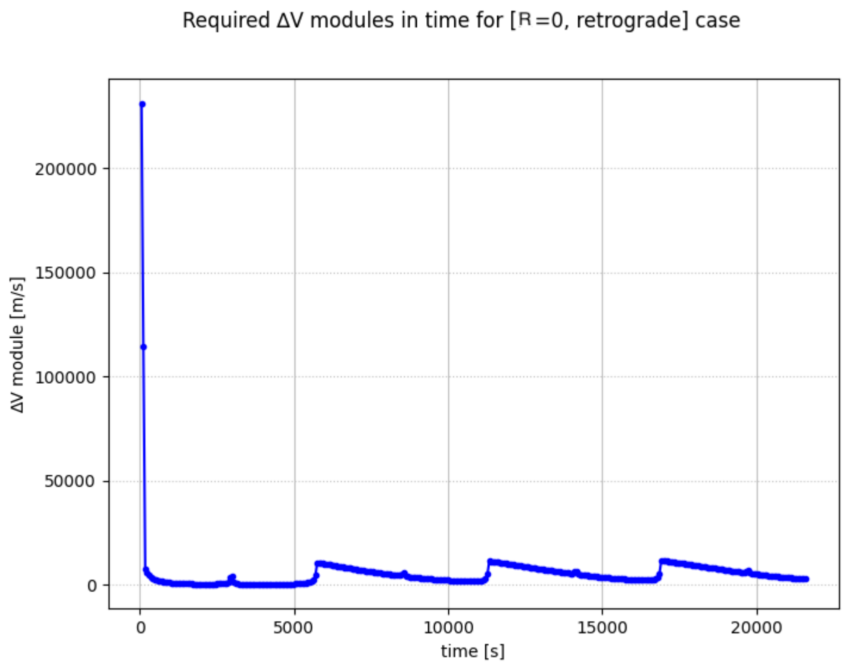

Figure 5.6: Required additional velocity over time for [R = 0, $prograde$ = $False$]

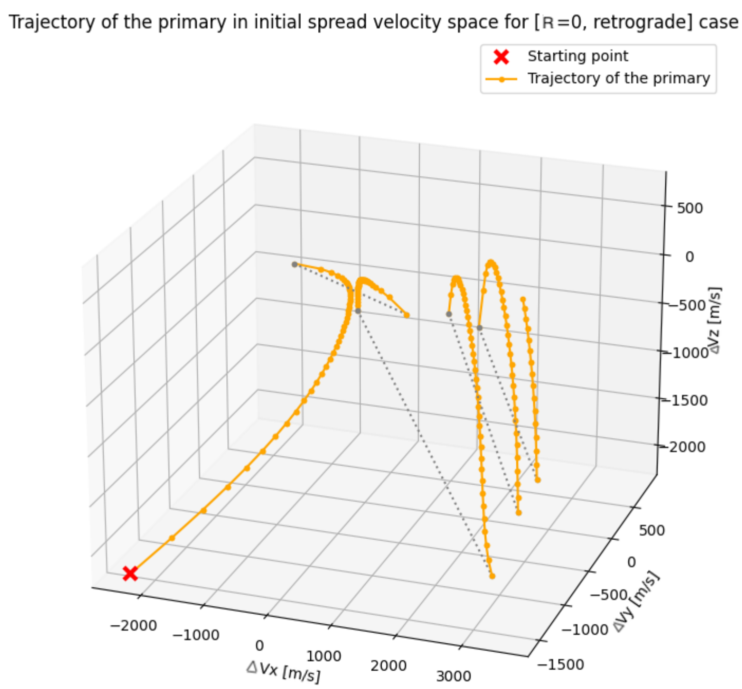

Figure 5.7: Trajectory of the primary mapped into spread velocity space for [R = 0, $prograde$ = $False$]

To conclude the analysis in the spread velocity space, Figure 5.8 shows the transformed ellipsoids for case [$R = 0$, $prograde = False$]. The directions of ejection velocity vectors time derivatives are also represented as blue arrows, which are locally tangent to the trajectory. As anticipated in Section 4.4.4, ellipsoids tend to reduce their size over time, leading to the primary cross section area in the spread velocity space reduction. This causes the integration volume to become thinner and it is due to the fact that, as the debris cloud evolves, its density decreases, reducing the probability of collision.

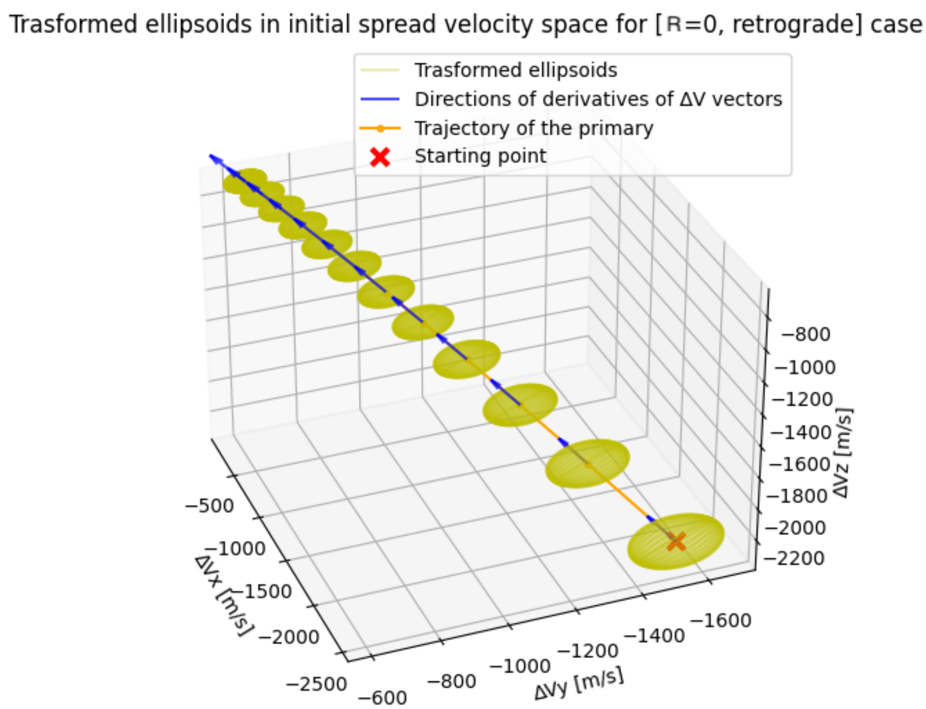

Figure 5.8: Portion of the trajectory of the primary mapped into spread velocity space with ellipsoids for [$R = 0$, $prograde = False$]

5.2 Final result

Finally, in this section the final output of the tool is presented. It is the cumulative short-term collision probability of the entire debris cloud and its time evolution is shown in Figure 5.9. The P_C reaches the maximum value of almost 10^{-2} after 6 hours from the break-up, starting from an initial value of about 10^{-6}. Actually, the latter serves only as an indication, because it is influenced by the time step of the simulation. The smaller the time step, the closer the first final position in the Lambert problem is to the position of the primary at the time of break-up. This reduces the time of flight, consequently increasing the ΔV required for the transfer orbit, and the associated PDF value becomes very small. This causes the probability curve to decrease with a steep slope as it approaches 0 seconds. Indeed, for $t = 0$, a clear vertical asymptote is visible. To have a more useful result from an operational point of view, the probability of collision is compared to the maneuvering threshold, set to 10^{-4}. It can be observed that just after 20 minutes, this threshold is overcome. Even though this is a test case specifically designed to ensure a certain level of probability and the primary is an object of considerable size, this result shows that this kind of event may pose an actual threat.

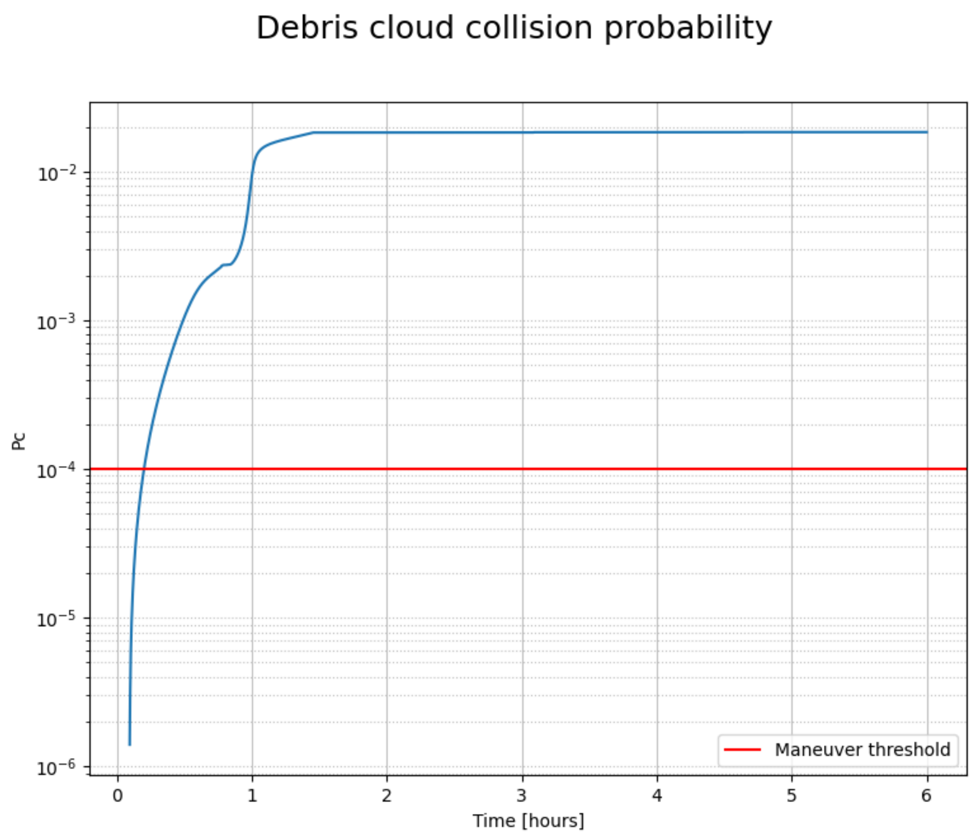

Figure 5.9: Cumulative collision probability of the debris cloud in the short-term of the test case

The cumulative collision probability provided by the tool is compared to the results proposed by [32], [34] and [40]. In particular, the output of the tool developed matches the P_C presented in [34], which has been validated through a Monte Carlo simulation. A keen eye might notice that the initial P_C value of the reference is lower than the one registered in Figure 5.9. This is due to the previously mentioned reason, since a much lower time step equal to $10\mu s$ is involved by the reference. Therefore, the initial P_C value is modified, while the overall P_C behaviour and its final value are not affected.

As a conclusion, the Python tool for short-term collision risk assessment between a debris cloud and an operational satellite successfully manages the analysis of this kind of scenario.

5.3 Break-up time uncertainties

The determination of the break-up epoch, i.e., the moment in which a fragmentation event occurs, is a complex process. It is usually determined through backward propagation of detected fragments. The time of break-up will be the time at which fragments reach the minimum distance. However, this approach is affected by different sources of uncertainties. First of all, to propagate a fragment, its state vector must be known. It can be only estimated through observations, thus, it may be strongly uncertain. Another challenge is linked to the lack of a precise ballistic coefficient of the fragment, since it is very hard to estimate the cross-section and the mass of an unknown object in space. An erroneous evaluation of the latter may lead to incorrect predictions of the effect of atmospheric drag on the fragment orbit, resulting in a miscalculation of the break-up epoch. As a result, predicting the exact time of an in-orbit break-up is characterised by uncertainty, making impossible its precise determination and only a time window can be provided. Break-up epoch uncertainties can be described involving statistical distributions.

As presented in Section 4.3, the developed tool works neglecting position uncertainty on the parent position at break-up time, assuming that the latter and, thus, the break-up epoch are precisely known. To make the tool more consistent from an operational point of view, a procedure to account for break-up epoch uncertainty is carried out and shown in this section.

The break-up time window can be described through statistical distributions, such as a Gaussian distribution characterised by a mean μ and a standard deviation σ. The approach consists in repeating the analysis of the problem, whose initial conditions are shifted in time of $\pm 3\sigma$, and observing how P_C curves change and shift with respect to each other. Therefore, the break-up time is changed and so the parent and primary positions at t_0 do. To update their position at the new initial time, it is sufficient to update the mean anomaly M, since the problem is in the assumptions of Kepler's dynamics. This can be done through Equation 5.1.

$$M_{new} = M + n\Delta t \tag{5.1}$$

In this expression, n is the mean motion computed as $2\pi/T$, where T is the orbital period of the parent or the primary.

For the specific test, no value of the standard deviation is available. However, for demonstration purposes, an arbitrary value is considered. The analysis of Cosmos-1408 break-up in 2021, which had a LEO orbit, provided two values of the standard deviation of break-up time for two different intersection thresholds: 1546 seconds for 50 km, and 944 seconds for 10 km [41]. The two values correspond to about 25 and 15 minutes. For the purpose of demonstrating the procedure, the analysis was extended to $\pm\sigma$, since considering $\pm 3\sigma$ would correspond to uncertainties of 75 and 45 minutes, which were deemed too large. The original P_C curve of Figure 5.9 is assumed to be referred to as the mean of the break-up time.

Figure 5.10 shows P_C curves for $\pm 1546s$ (in orange) and $\pm 944s$ (in green) related to the original one (in blue). Dashed curves refer to negative values of σ, while positive values are represented as solid lines.

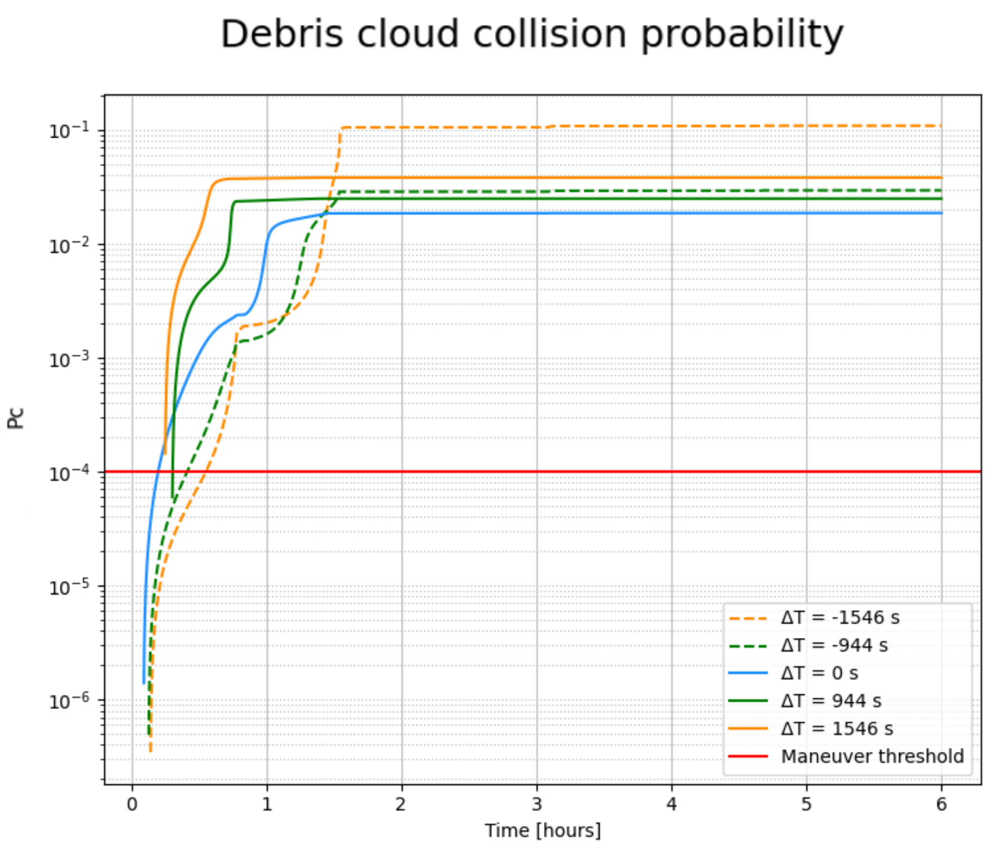

Figure 5.10: Cumulative collision probability of the debris cloud in the short-term for different break-up epochs

As it was expected, curves are different. The reason for this effect lies in the fact that changing the break-up time has altered the initial relative geometry. This leads to a variation in the solution of the Lambert's problem, meaning that the ΔV norms required to reach the primary at a given position within a certain time of flight have changed.

Consequently, the PDF assumes different values, which in turn modifies the overall probability.

At this point, it may be interesting to understand what are the causes that lead one curve to overtake or undershoot the others. Figure 5.11 is referred to [$R = 0$, prograde=True] case and is very helpful in this optic. This plots shows the required ejection velocity norms trajectory for the simulation time for different break-up times, coded in different colours and markers. The mint green dashed line and box in the background represent, respectively, the mean and standard deviation of the ejection velocity norms PDF employed by the tool. The plot is in logarithmic scale, since the variable of ejection velocity distribution is $log_{10}\Delta V$. The closer the required ΔV trajectory is to the mean of the ΔV distribution, the higher the PDF value, and the higher the overall probability of collision.

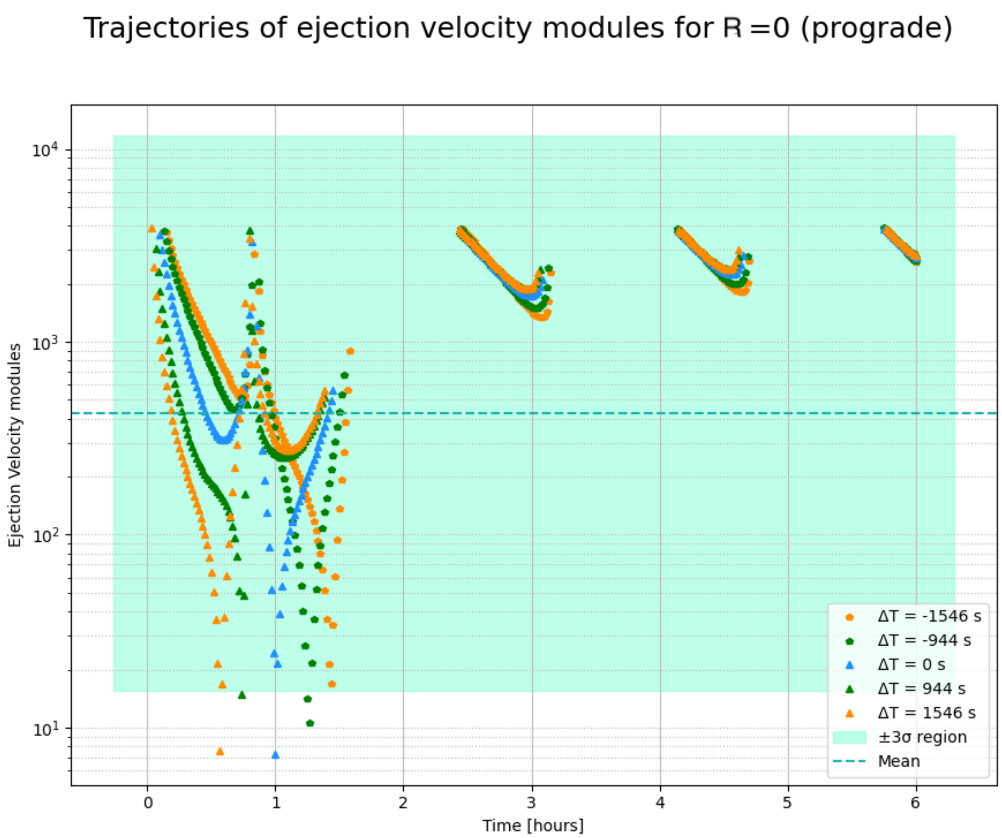

Figure 5.11: Trajectories of ejection velocity norms for different break-up epoch

This specific plot represents the situation for a single case of the Lambert's problem, but strictly speaking, these considerations should be applied to all possible cases of the Lambert problem. Therefore, the probability of collision for a specific break-up time will be highest if, on average, the required ΔV trajectories for all cases of the Lambert problem are the closest to the mean of the distribution. It is worth noting that these are trajectories of norms and not ΔV vectors, because their directions do not affect the PDF value, as an isotropic ejection model is involved.

However, the PDF value is not the only piece of the integral of Equation 4.6. The effect of the change of break-up location on the area of the collision cross-section should also be considered.

All these considerations translate into a useful operational result, which consists of considering the worst-case scenario of exceeding the maneuver threshold. The first probability curve that exceeds this threshold over time represents the earliest moment when a potential collision avoidance maneuver might be necessary. In this specific case, the maneuver threshold is still exceeded by the original curve after 20 minutes.

5.4 Future work

As a final note, this section is dedicated to outlining potential avenues for future work that could further refine and improve the tool that has been developed.

First of all, as specified in 4.4.6, the tool is currently only suitable to manage debris clouds generated by in-orbit explosions, hence break-ups of a single parent. However, debris clouds can be generated by in-orbit collisions and they may still pose a threat for active satellites. If an in-orbit collision occurs, fragments belong to two distinct parents, with two different orbital velocities. Since the Lambert's problem provides the orbital velocity of transfer orbits but the methodology for collision risk assessment needs the required additional velocity, it must be computed. Knowing from which parent a fragment is ejected means knowing which of the two orbital velocities must be subtracted to Lambert's solutions in order to get the $\vec{\Delta V}$. Fragments can be associated with a given parent in different ways, either using a statistical approach or a more physically consistent method that ensures the conservation of physical laws, such as momentum conservation. After this process, the short-term probability of collision can be computed following the same procedure provided by the current tool.

Secondly, the tool involves a simplified ejection velocity probability density function, which is not dependent on the A/M ratio of the fragment. To achieve more consistency with NASA's SBM, its original distributions can be considered. Hence, for each L_c, an A/M ratio is extracted and there is a corresponding ΔV PDF value. This feature has already been proposed by [32], which divides A/M values in bin. This corresponds to consider the same ejection velocity distribution for fragments with similar area-to-mass ratio, allowing to save computational time.

–6– Conclusions

This thesis work is set in the context of short-term collision risk assessment following in-orbit break-up events. The main motivation behind this research stems from the need to develop effective tools for quickly evaluating the collision risks posed by debris clouds to active satellites immediately after fragmentation events.

The thesis begins by providing an overview of the space debris environment, highlighting its overcrowded nature. Break-ups have been rigorously defined, with a focus on their causes and different types of events. Challenges associated with assessing the probability of collisions involving debris clouds immediately after the fragmentation have been explored. These challenges include the lack of immediate fragment data following a break-up and limitations in tracking small fragments. These limitations prevent the direct application of classical collision probability methods, necessitating the development of new approaches for debris cloud risk assessment.

A review of existing break-up model categories is conducted, highlighting advantages and disadvantages. A key element in the analysis of NASA's Standard Break-up Model, the most used empirical model that has been refined over decades based on in-orbit break-ups and ground experiments. The SBM describes the outcome of a collision or explosion, providing statistical distributions of fragment size, area-to-mass ratio, and imparted velocity. However, one limitation is that it only provides the magnitude of the ΔV distribution and does not account for the directions of the imparted velocities. The latter is crucial in applications of collision risk assessments and debris environment analysis, as it directly influences the trajectory of the debris fragments and their potential to collide with operational spacecraft. To address this gap, the isotropic ejection model is commonly used. This model assumes that fragments are ejected uniformly in all directions and is considered a conservative approach. It is widely used because of its simplicity, but it may not always reflect the real behaviour of debris clouds. In practice, ejection directions are often influenced by specific dynamics during the break-up event, making it difficult to accurately estimate preferential ejection patterns.

The thesis also delves into the evolution of the debris cloud over time, which is characterised by three distinct phases governed by different forces. Initially, the debris movement is dominated by the imparted velocities from the break-up event. In the second phase, the Earth's oblateness perturbation becomes more significant, while in the long-term, atmospheric drag and other perturbations play a key role in shaping the cloud's behavior. Throughout these phases, distributions of mean anomaly, argument of perigee and right ascension of the ascending node reflect the cloud dynamics. Furthermore, the propagation of a test case demonstrated that in the short-term, the only orbital parameter that truly experiences variations and moves towards randomization is the mean anomaly. This observation supports the validity of applying Kepler's motion assumptions in the short-term evolution of debris clouds. These assumptions can be reflected in the development of the tool, allowing for more efficient simulations while maintaining accuracy. Additionally, the duration of the short-term phase is estimated through two different approaches.

The core of the thesis presents a detailed analysis of the methods used to compute the collision probability in the aftermath of a break-up. By exploring both theoretical aspects and practical implementation, a prototype tool was developed to assess the short-term collision risk for a debris cloud scenario. Simplifying assumptions, in line with the state of the art of the problem, have been made and clarified. The only uncertainty considered is related to the initial velocity of the parent through the SBM. All other uncertainties regarding the primary and the parent can be neglected, as the SBM is a statistical model and therefore inherently very uncertain. The key element of the developed methodology involves mapping the primary trajectory in the time window of interest from the position space at a certain time to the spread velocity space at time of break-up. This process leverages the multi-revolution Lambert problem to estimate what is the ΔV that a fragment should have to collide with the primary in the future. This approach allows to perform the integral to compute the probability of collision in the spread velocity space, integrating the probability density function of ejection velocity along the path swept by the satellite image in spread velocity space. The final chapter presents the testing and validation of the developed tool through a common test case that has already been employed in literature to validate other methodologies and whose ground truth is provided by Monte Carlo simulations. The results match the reference and demonstrate the tool's effectiveness in assessing collision risk between a debris cloud generated by an in-orbit explosion and an active satellite in the short-term. To account for the uncertainty of the break-up, an alternative approach is proposed t position the tool within a more operational perspective.

In conclusion, this thesis contributes to the advancement of short-term collision risk assessment methods, offering a prototype tool that can be further developed and refined for more complex scenarios. Although this test case is designed to produce a specific probability trend, such break-up events can pose a real threat to operational spacecraft. Therefore, analyses of this type are recommended and necessary to mitigate the risks posed by space debris in increasingly congested orbital environments.

Bibliography

[1] ESA's Space Debris Office. *Space Environment Statistics*. visited on 12/04/2024. 2023. URL: `https://sdup.esoc.esa.int/discosweb/statistics/`.

[2] NASA Orbital Debris Program Office. *Orbital Debris Quarterly News, Volume 15, Issue 4*. 2011.

[3] Jacob Daniel Griesbach, David A Vallado, and Jacob D Griesbach. *"Simulating Space Surveillance Networks"*. 2011.

[4] H. Klinkrad. *Space Debris: Models and Risk Analysis*. Jan. 2006.

[5] Mark Matney et al. *"An Overview of NASA's Newest Engineering Model, ORDEM 4.0"*. 2003.

[6] Andrew Vavrin et al. "NASA Orbital Debris Engineering Model ORDEM 3.1-Software User Guide Orbital Debris Program Office". In: (2019).

[7] A. Tan, T. X. Zhang, and M. Dokhanian. "Analysis of the Iridium 33 and Cosmos 2251 Collision using Velocity Perturbations of the Fragments". In: *Advances in Aerospace Science and Applications* 3 (1 2013), pp. 13–25.

[8] NASA Orbital Debris Program Office. *Orbital Debris Quarterly News, Volume 13, Issue 2*. 2009.

[9] Nicola Cimmino et al. "Tuning of NASA standard breakup model for fragmentation events modelling". In: *Aerospace* 8 (7 July 2021).

[10] Felix Roach Hoots and Marlon E. Sorge. "Satellite Breakup Parameter Determination". In: *The Journal of the Astronautical Sciences* 59 (2012), pp. 120–140.

[11] Simon Barrows. "Evolution of artificial space debris clouds". PhD thesis. University of Southampton, Mar. 1996.

[12] J. Geul, E. Mooij, and R. Noomen. "Modelling and assessment of the current and future space surveillance network". In: (2017).

[13] D. Mehrholz et al. "Detecting, tracking and imaging space debris". In: *Fraunhofer FHR* 109 (Feb. 2002).

[14] William J. Tedeschi et al. "Determining the effects of space debris impacts on spacecraft structures". In: *Acta Astronautica* 26 (7 1992), pp. 501–512.

[15] N.L. Johnson et al. "NASA's new breakup model of evolve 4.0". In: *Advances in Space Research* 28 (Dec. 2001), pp. 1377–1384.

[16] Akhil Rao et al. "An Integrated Assessment Model for Satellites and Orbital Debris". In: (2023).

[17] A. Bade et al. "Breakup model update at NASA/JSC". In: (Jan. 2000), pp. 125–138.

[18] Jonas Schuhmacher. *"Efficient Implementation and Evaluation of the NASA Breakup Model in modern C++"*. Master's Thesis, Technical University of Munich. 2021.

[19] Deanna L. Mains and Marlon E. Sorge. "The IMPACT satellite fragmentation model". In: *Acta Astronautica* 195 (June 2022), pp. 547–555.

[20] P. H. Krisko, M. Horstman, and M. L. Fudge. "SOCIT4 collisional-breakup test data analysis: With shape and materials characterization". In: *Advances in Space Research* 41 (7 2008), pp. 1138–1146.

[21] Heather Mae Cowardin et al. "Characterization of Orbital Debris via Hyper-Velocity Laboratory-Based Tests". In: (2017).

[22] James Murray et al. "Analysis of the DebriSat Fragments and Comparison to the NASA Standard Satellite Breakup Model". In: (2019).

[23] Martin Schimmerohn et al. "Numerical investigation on the standard catastrophic breakup criteria". In: *Acta Astronautica* 178 (Jan. 2021), pp. 265–271.

[24] C. A. Smith and A. R. Motevalli. "Inertial and aerodynamic coupling effects on aircraft". In: *Journal of Aircraft* 16.9 (1979), pp. 594–600.

[25] Francesca Letizia. "Space debris cloud evolution in Low Earth Orbit". PhD thesis. Feb. 2016.

[26] Rüdiger Jehn. "Dispersion of Debris Cloud from In-Orbit Fragmentation Events". In: (Sept. 1990).

[27] A. Chobotov et al. "Dynamics of Debris Motion and the Collision Hazard to Spacecraft Resulting From an Orbital Breakup". In: (1988).

[28] N.L. Johnson and D.S. McKnight. *Artificial Space Debris.* 1987.

[29] J. F. Spann, C. E. Randall, and G. J. Romick. "Effect of auroral structure on satellite ultraviolet remote sensing of auroral electron energy parameters". In: *Advances in Space Research* 10.6 (1990), pp. 61–64.

[30] Jia-Sheng Li, Zhen Yang, and Ya-Zhong Luo. "A review of space-object collision probability computation methods". In: *Astrodynamics* (Apr. 2022).

[31] Francesca Letizia, Camilla Colombo, and Hugh G. Lewis. "Collision probability due to space debris clouds through a continuum approach". In: *Journal of Guidance, Control, and Dynamics* 39 (10 2016), pp. 2240–2249.

[32] Cristina Parigini, Reem Algethamie, and Roberto Armellin. "Short-Term Collision Probability Caused by Debris Cloud". In: *Journal of Guidance, Control, and Dynamics* (Jan. 2024), pp. 1–13.

[33] Alan B. Jenkin. "Probability of collision during the early evolution of debris clouds". In: *Acta Astronautica* 38 (4-8 1996), pp. 525–538.

[34] Peng Shu, Zhen Yang, and Ya Zhong Luo. "Impact Risk of a Debris Cloud to Spacecraft". In: *Journal of Guidance, Control, and Dynamics* 46 (5 May 2023), pp. 989–997.

[35] Ryan P. Russell. "On the solution to every Lambert problem". In: *Celestial Mechanics and Dynamical Astronomy* 131 (11 Nov. 2019).

[36] Juan Luis Cano Rodríguez and the poliastro development team. *Revisiting Lambert's Problem in Python*. Accessed: 2024-09-06. 2024. URL: `https://docs.poliastro.space/en/stable/examples/Revisiting%20Lamberts%20problem%20in%20Python.html`.

[37] Wilfred Kaplan. *Advanced Calculus*. 1973.

[38] Stefan Frey and Camilla Colombo. "Transformation of satellite breakup distribution for probabilistic orbital collision hazard analysis". In: *Journal of Guidance, Control, and Dynamics* 44 (1 2021), pp. 88–105.

[39] Dario Izzo. "Revisiting Lambert's problem". In: *Celestial Mechanics and Dynamical Astronomy* 121 (1 Jan. 2015), pp. 1–15.

[40] Peng Shu et al. "Collision Probability of Debris Clouds Based on Higher-Order Boundary Value Problems". In: *Journal of Guidance, Control, and Dynamics* 45 (8 2022), pp. 1512–1522.

[41] Ronglan Wang et al. "Breakup analysis of Cosmos 1408 Satellite". In: *Journal of Space Safety Engineering* 11 (2 June 2024), pp. 335–341.